INFORMATION TO USERS

This manuscript has been reproduced from the microfilm master. UMI films the text directly from the original or copy submitted. Thus, some thesis and dissertation copies are in typewriter face, while others may be from any type of computer printer.

The quality of this reproduction is dependent upon the quality of the copy submitted. Broken or indistinct print, colored or poor quality illustrations and photographs, print bleedthrough, substandard margins, and improper alignment can adversely affect reproduction.

In the unlikely event that the author did not send UMI a complete manuscript and there are missing pages, these will be noted. Also, if unauthorized copyright material had to be removed, a note will indicate the deletion.

Oversize materials (e.g., maps, drawings, charts) are reproduced by sectioning the original, beginning at the upper left-hand corner and continuing from left to right in equal sections with small overlaps.

Photographs included in the original manuscript have been reproduced xerographically in this copy. Higher quality 6" x 9" black and white photographic prints are available for any photographs or illustrations appearing in this copy for an additional charge. Contact UMI directly to order.

ProQuest Information and Learning
300 North Zeeb Road, Ann Arbor, MI 48106-1346 USA
800-521-0600

VIBRATION CONTROL OF FLEXIBLE STRUCTURES USING SMART MATERIALS

By

Rafael Bravo, Mech. Eng., M. Eng.

A Thesis
Submitted to the School of Graduate Studies
In Partial Fulfillment of the Requirements
for the Degree of
Doctor of Philosophy
McMaster University

Doctor of Philosophy (2000)
(Mechanical Engineering)

MCMASTER UNIVERSITY
Hamilton, Ontario

TITLE: Vibration Control of Flexible Structures Using Smart Materials

AUTHOR: Rafael Bravo
Mechanical Engineer
Universidad del Zulia
Maracaibo, Venezuela

Master of Engineering
McMaster University
Hamilton, Ontario

SUPERVISORS: Dr. Mohamed Dokanish
Dr. Anthony Vaz

NUMBER OF PAGES: xix, 173

Abstract

This work presents the analytic and experimental development of active vibration control of large flexible space structures (LFSS) using smart materials. Two basic configurations were studied: flexible manipulators, and truss structures, which encompass most of the flexible structures in space applications. The dynamics of LFSS are characterized by their high order and the significant presence of lightly damped, closely spaced low frequency modes. . In space applications, space structures are required to perform precision trajectory tracking and attitude regulation, tasks that introduce disturbance torques and forces that may excite vibrational modes in the flexible parts of the structures, degrading their performance. To solve this problem, the use of piezoelectric materials coupled to structural members, to form smart structural members, is proposed for the implementation of active control techniques.

For the flexible manipulator, the use of shaped piezoelectric sensors is presented. Piezoelectric sensors can be shaped to provide state feedback, which can be used as part of a control law to compensate vibrations induced by flexible degrees of freedom. A robust H_∞ state feedback control law is obtained. The control law is implemented using the shaped sensor to stabilize the flexible manipulator. Simulation and experimental results in a single link flexible manipulator confirm the effectiveness of the proposed approach.

The design of a truss structure and the control for active damping of vibration is presented, taking advantage of the use of piezoelectric actuators and sensors. Three control techniques are tested: negative velocity feedback, LQG and H_∞ control. Simulations and experiments are performed on the closed loop to assess the relative merits of each control technique. Results show that the controllers increase the damping of the structure noticeably. The robust H_∞ controller provides the better performance of the control techniques presented, even in the presence of higher order modes and parametric uncertainties not accounted for in the control design process.

Dedication

To Maigua and Leda, the two most wonderful and giving persons in the world.

Acknowlegments

I would like to thank my supervisors, Dr. Mohamed Dokainish and Dr. Anthony Vaz, for their invaluable contribution in all aspects of making this research a success. I would also like to thank the members of my Ph.D. supervisory committee, Dr. Mohamed Elbestawi and Dr. Gary Bone for their valuable suggestions and insight.

My co-workers at the Mechanical and Electrical Engineering departments deserve my gratitude for their timely and disinterested help in technical aspects of the research, particularly Steve Leatherland, and Marwan Hassan. Without their contribution, mine would have been a much harder task.

I would like to thank the staff at the department of Mechanical Engineering: Rebecca Clifford, Allison Wenzowski, Jane Mah and Betty Ann Bedell-Ryc for their prompt, friendly and efficient help in administrative matters, and Dave Schick, Ron Lodewyks, Jim McLaren and Joe Verhaeghe for their competent advice in technical issues.

I wish to express my gratitude to my dear wife Maigua, that provided me with encouragement, patience, love and company during all the years of education that culminated with this thesis. Without the help and support of my mother Leda it would have been impossible to complete this work.

Finally, I gratefully acknowledge the financial support of Universidad del Zulia, Maracaibo, Venezuela, the Ministry of Education and Training of Ontario, and the Canadian Space Agency.

Contents

List of Tables

List of Figures

List of Acronyms

ADC	Analog to Digital Conversion
AFL	Articulated Flexible Link
CAD	Computer-Assisted Design
DAC	Digital Analog to Conversion
DC	Direct Current (Zero frequency level)
LFSS	Large Flexible Space Structure
LFT	Linear Fractional Transformation
LMI	Linear Matrix Inequality
LQG	Linear Quadratic Gaussian
LQR	Linear Quadratic Regulator
MIMO	Multi-Input, Multi-Output
NACT	Number of Active truss members
NDOF	Number of Degrees of Freedom
NNOD	Number of Nodes
NSENS	Number of Sensed truss members
PVDF	PoliVinyldene Di-Fluoride
PZT	Lead Zirconate Titanate Piezoceramic

List of Symbols

Flexible Manipulator Modelling and Control

θ	Joint angle
ϕ_i	Mode shape of mode i
ω_i	Mode frequency of mode i
ζ_i	Modal damping coefficient for mode i
$\Xi(x)$	Shape function of piezoelectric sensor
ε	Strain
$\in_c$	Permittivity of the piezoelectric film
I_{cs}	Moment of inertia of cross-section
A_{cs}	Area of cross-section
E	Young's Modulus
J_h	Moment of inertia of hub
V_{oc}	Open circuit voltage
I_{sc}	Short circuit current
W, L, t	Width, length and thickness
M, H, K	Mass, damping and stiffness matrices
A, B, C, D	State space matrices

$e_{31}(x)$	Charge to strain ratio at location x

Piezoelectric Variables

d_{31}	Transverse piezoelectric charge to stress ratio
g_{31}	Voltage to strain coefficient
c_f^S	Film capacitance at constant strain
c_f^T,	Film capacitance at constant stress
s_f^E	Film compliance at constant electric field intensity
e_f	Film charge to displacement ratio
d_f	Film charge to force ratio
C_c	Piezoelectric film capacitance

Truss Structure Modelling and Control

η	Modal coordinate vector
Φ	Modal Matrix
ε	Strain
ψ^k	Truss member k to piezoelectric stiffness ratio
H, Λ	Modal damping, squared modal frequencies matrices
q	Physical coordinate vector

x, y, u	State space, output space, control vector
M, K	Mass and Stiffness matrices from Finite Element Analysis
A, B, C, D	State space matrices
A_k, B_k, C_k, D_k	Dynamic controller state space matrices
$V_{oc}^{k}(t)$	Open circuit voltage at truss member k
$I_{sc}^{k}(t)$	Short circuit current at truss member k
$M_{V_{oc}}$	nodal displacement to open voltage gain matrix
$M_{I_{sc}}$	nodal rate vectors to short circuit current gain matrix
K_v	Negative velocity feedback gain matrix
s, a	Subscripts denoting sensor and actuator

1. Introduction

Large Flexible Space Structures (LFSS) are being used in orbit in applications such as space stations, large communication satellites, manipulator arms and others, which carry sensitive payloads, such as scientific instruments, antennas, solar panels, or manned research laboratories. Due to the particular requirements of this applications, the structures have large dimensions, are assembled in orbit, and due to the high cost of sending large masses and volumes into space, they are made of lightweight, slender elements. One side effect of these requirements is the large flexibility of these LFSS, which typically results in low frequency, lightly damped, clustered vibrational modes. Examples of LFSS are the Canadian Canadarm shuttle manipulator system, and the new International Space Stations currently being built by the United States and Russia in partnership with Canada, Europe and Japan.

The dynamics of LFSS are characterized by their high order and the significant presence of closely spaced, lightly damped low frequency modes. This fact presents a challenging problem to the designer of the structure, who requires a level of performance in order to carry out the mission assigned to the system. In space applications, space structures are required to perform precision trajectory tracking and attitude regulation,

tasks that introduce disturbance torques and forces that may excite vibrational modes in the flexible parts of the structures.

There are two possible ways of dealing with the flexibility problem: design it out of the system by using more robust, stiffer structural members, or include in the design means of counteracting the resulting oscillations. The first way is not feasible due to the reasons mentioned previously, while the second option involves artificially increasing the damping of the system, by either passive or active means. Passive damping techniques are commonly used in civil engineering structures and involve the use of elastomeric materials that have high rate of energy dissipation, or viscous damping systems. Unfortunately, those techniques have a limited use in space applications due to the additional weight and volume that they involve, and in some cases are only effective for relatively large frequencies.

Active damping techniques make use of sensors and actuators to measure some key variables of the flexible structure and perform corrective action, to attempt to minimize the maximum amplitude and the settling time of the undesired oscillations. These techniques require certain level of knowledge about the dynamic behaviour of the structure, which is achieved using mathematical modelling, with tools such as the finite element method, or using experimental model identification techniques, such as modal testing.

One issue that arises when modelling dynamic system for control purposes is the accuracy of the model behaviour as compared to the actual structure. For example, LFSS are infinite order systems, while their mathematical models are usually finite-dimensional approximations that neglect higher order dynamics. Even modeled modes of vibration

tend to have a degree of inaccuracy, due to uncertainty in the knowledge of mechanical parameters, and simplifications and assumptions taken during the modelling process. Moreover, these models do not provide damping ratios, hence they are originally undamped. Model identification of LFSS is often impractical because such structures are assembled in space and are difficult to test on earth because of the presence of the gravity field and the atmosphere. Thus it is desirable to have a control design procedure that can use the uncertain mathematical model and some knowledge of the uncertainty bounds and provide a controller that is guaranteed to be stable when implemented on the actual LFSS.

The next subsections present a review of the relevant literature published on the subject of modelling and control of LFSS. Two main applications were considered in this research: flexible manipulators and truss structures, which represent most of the typical configurations encountered in space applications. Each one presents its own challenges and solutions in terms of modelling, sensor and actuator choice, design, and location, and control design for robust stability. The results of the survey are divided into the following subjects: modelling and control of flexible manipulators, active vibration control on LFSS and modelling of piezoelectric materials in smart structures applications

1.1. Flexible Manipulators: Modelling and Control

Several researchers have addressed the problem of control of manipulators with flexible links in the last 20 years. One of the first works is by Book, Maizza-Neto *et al.* [7], which presents a time domain and a frequency domain modelling approach. They use the assumed modes method and linearization to obtain a model, which is employed for the design of a feedback controller using pole-placement to meet reasonable performance

specifications. Cannon and Schmidtz [14] presented theoretical and experimental results for the case of a flexible one-link arm. They modelled the arm as a flexible pinned-free beam, neglecting velocity coupling between the flexible and rotary degrees of freedom. Their controller was obtained using a Linear Quadratic Gaussian (LQG) technique to minimize a performance index that penalizes the deformation states and the control torque. The sensors were a tip-position sensor and a hub-rate sensor, while the remaining elements of the state were estimated. The experiments showed that the controller was capable of providing satisfactory tip control response. Biswas and Klafter [6] also presented simulation results for a flexible one-link manipulator. The model of the manipulator was obtained assuming that the link oscillates around its rigid body position as a clamped-free beam, and the complete dynamic model was obtained using Hamilton's principle. The optimal controller considered a performance index that included weights on joint angle and tip position at the end of the motion, as well as the deflection, deflection rate and the control input during the motion period. The numerical results of the manipulator using a nominal control (not considering flexibility) were compared to the optimally controlled system, showing that the latter provided a marked improvement on the performance.

Sunada and Dubowsky [35] presented a method for analyzing manipulators with complex-shape flexible links, using Finite Element Analysis tools and homogeneous transformation matrices. Comparison between experiments and simulations showed good correlation, and link flexibility was demonstrated to have a significant impact on system performance and stability. Wang [41] presented an experimental comparison of several optimal and non-optimal control strategies, such as LQR, H_∞, PD, etc. The experimental

setup consisted of a DC servomotor directly attached to the link without gearing. The sensed variables were the motor angle, using an optical encoder, and the tip deflection, using a CCD array camera that observes the displacement of an LED that was installed at the end of the flexible link. The results showed that the optimal controllers required higher initial torques, which produced higher initial tip deflection, which can lead to mechanical fatigue problems. The optimal controllers were able to damp the induced oscillations out quickly, and provide better robustness than the non-optimal techniques tested. This results seemed to indicate that depending on performance and practical requirements, non-optimal control strategies may be better suited for the task.

1.2. Active Vibration Control of Large Flexible Space Structures

Active vibration control of LFSS has been the subject of increased attention, due to the appearance of large, lightweight structures, mainly for aerospace applications (Balas [5]). In this type of structures, a consequence of the large size and light weight of the system is the presence of low frequency, lightly damped, clustered vibrational modes, which can interfere with the performance of the structure.

The Linear-Quadratic-Gaussian control method, or LQG control, was developed in the 1960s and is capable of obtaining controllers for multiple input-multiple output systems such as the ones in consideration in this research. LQG controllers give good response when model dynamics are known exactly. However, LQG controllers do not necessarily cope well with model uncertainty (Doyle [16]). Furthermore, the infinite bandwidth of LQG controllers can also excite unmodelled higher order dynamics. This effect is termed the "spillover problem" (Balas [5]). Allen *et al.* [1] applied the LQG method directly to the problem of vibration suppression in a truss structure. Their results

showed a limit on the performance specifications and gain values after which stabilizing controllers were not possible. Allen *et al.* [2] employed a frequency weighted LQG method, in which the system dynamics are augmented with bandpass filters for the input and output signals. This accounted for the infinite controller bandwidth and sensitivity to modelling uncertainty that standard LQG controllers showed. They applied this method successfully to an experimental structure, obtaining a controller design with specified bandwidth and robustness.

The H_∞ control design method (Doyle *et al.*[17], Zhou *et al.*[44]) has recently been applied to the problem of control of large flexible space structures. This is because of its capability in obtaining a controller that robustly stabilizes the system in the presence of bounded structured and unstructured uncertainties, while at the same time allowing the designer to specify performance requirements. A general solution of the general multiple-input-multiple-output (MIMO) H_∞ optimal control problem was presented by Francis [19]; the solution relied on state-space methods but suffered from problems with the high order of the resulting controller. Doyle *et al.*[17] obtained a simpler state-space formula that provided a lower order controller, showing that the controller need not be of an order higher than that of the plant.

Boulet [9] showed an H_∞ controller design using a left co-prime factorization model of the plant and perturbations applied to a flower-shaped experimental structure with 20 flexible modes between 0.05 and 0.12 Hz. The structure had pulse-width modulation (PWM) controlled air jet thrusters at each flexible rib for actuation; at the tip of each rib there were accelerometers and a light-emitting diode (LED). At the hub there were CCD cameras to measure the position of these diodes. He obtained a good

performance without the need of additional tuning of the controller, which meant that the controller coped well with the perturbations and uncertainties. Buddie *et al.*[12] used a "weighted gap optimization" approach for the synthesis of the H_∞ controller, employing input and output weighting functions to "shape" the open loop response of the system. Experiments were performed in both a flower shaped structure and in a truss structure, and in both cases success was achieved in increasing the damping for particular modes while obtaining a specified level of robustness. They used momentum exchange actuators, operated by linear DC motors. The accelerometer sensors were collocated at the actuator locations, and their signals are integrated to provide velocity. Morris [28] analyzed the problem of noise reduction in ducts, analog to active vibration control, and showed that the optimal H_∞ controller made the closed loop system unstable. She obtained a stabilizing suboptimal controller, and showed that there existed a "spatial waterbed" effect (i.e. noise levels are increased for points outside the region for which the design is done) for some cases. A good survey on the subject of control laws for flexible spacecraft was provided by van Woerkom [37]. He showed several examples of spacecraft that presented challenging problems due to their flexibility; among others the OGO series of satellites and the Hubble space telescope. Various control techniques were discussed and examples of its applications are presented.

1.3. Piezoelectric Materials in Smart Structures

The use of piezoelectric materials as sensors and actuators in flexible systems has been a topic of research since the mid 1980s. Hubbard and his collaborators [3,13,31] proposed the application of piezoelectric polymer (PVDF) as actuator for the active damping of beams with different boundary conditions. The sensors employed were tip

mounted linear and angular accelerometers for the case of cantilever beams and a base-mounted angular accelerometer for the case of the simply supported beam. They used several linear and non-linear velocity-feedback control techniques to artificially increase the modal damping ratios of the flexible beam, and these control laws were applied to rectangular and spatially varying distributed PVDF films, with voltage levels of up to ±250 V. A significant level of damping increase was attained, particularly when using non-linear on-off velocity feedback control.

Crawley and de Luis [15] developed an analytic framework for the static and dynamic modelling of the interaction between piezoelectric materials and the structure they are attached to, when used as actuators. They obtained equations that predict the combined piezoelectric-structure response to applying a voltage across the piezoelectric actuator, for the cases of surface-bonded and embedded actuators, in bending or extension, and considering perfect or imperfect bond between the piezoelectric material and the structure. Their predictions were compared to experiments performed on cantilevered beams of various materials and actuator placement. Vaz [38,39,40,41] extended their work to comprise the behaviour of shaped piezoelectric sensors and actuators. The effect of shaping the electrode on the response of the structure-piezoelectric film pair was analyzed, showing that by etching an adequate shape to the piezoelectric sensor, it is possible to make the sensor work as a modal filter. This feature can be used to produce "intelligent" sensors, that are designed to provide state feedback according to any control law, thus simplifying the hardware required for control. Farr [18] presented experimental results to validate for the structure-piezoelectric interaction equations presented by Vaz. He developed and tested several techniques for bonding and

shaping of sensors and actuators, and developed circuits for the conditioning of the sensor signals. He introduced a bonding factor to account for differences between experiments and simulations due to factors like bonding shear. Experimental results are obtained for shaped piezoelectric acting as modal filters in a cantilever beam configuration.

Miller and van Schoor [27] discussed the estimation of exact displacement and displacement feedback kernels in flexible structures for finite dimensional control based on finite element structural models. They proposed the use of curvature and curvature rate area-averaging sensors, such as shaped piezoelectric films, to extend the discrete, finite dimensional feedback gains into infinite order full state feedback. Ryou et al. [34] presented the design of a distributed piezoelectric film sensor and actuator for the vibration control of a plate. The distribution of the piezoelectric film over the surface of the plate was optimized using genetic algorithms to minimize the system energy in the control modes. A discrete LQG control law was applied for vibration control.

1.4. Objectives of the Research

The objectives to be reached in this research can be summarized as follows:

a) Development, numerical simulation and experimental validation of control techniques for LFSS. This is to be achieved taking advantage of smart structures technology, with emphasis on the use of piezoelectric sensors and/or actuators.

b) Modelling and characterization of the piezoelectric-structure pair, for sensing and actuation applications. The interaction equations are to be expressed in a way that is compatible with the finite element and modal models of the structures to be analyzed.

c) Comparison of the different control techniques applicable to the problem of control of LFSS, and assess their theoretical and practical advantages and disadvantages, in terms of performance, robustness, flexibility and complexity.

1.5. Thesis Organization

The thesis is divided in two parts. Chapters 2 and 3 deal with the one-link flexible manipulator problem. Chapter 2 presents the theoretical development of mathematical models to characterize the dynamic behaviour of the manipulator, as well as the relations that model the operation of a shaped piezoelectric film when used as a sensor. The interaction equations between the piezoelectric sensor and the flexible link are shown in terms of its state space observation matrix representation. In chapter 3, the robust control technique used for control of the flexible manipulator is presented. The feedback controller is implemented using shaped piezoelectric films. Simulation and experimental results are presented.

The truss structure active vibration control problem is studied in chapters 4, 5 and 6. In chapter 4 the design and modelling process on the truss structure is shown. A complete dynamic model is obtained using the finite element method and modal analysis. The influence of the piezoelectric sensors and actuators on the dynamic model is found, and the state space model of the system, including sensors and actuators is obtained. The control design process is presented in chapter 5 together with numerical simulations of the closed loop system (dynamic model plus controller) for the cases of negative velocity feedback, LQG, and H_∞ control. Experimental verification of the simulation results obtained in chapter 5 is shown in chapter 6. Details of the experimental testbed used for

the verifications are given, including instrumentation and electronics used. Experiments are performed for impact tests on the nominal and perturbed structure, as well as continuous disturbance tests.

The conclusions of the research and suggestions for future work are presented in chapter 7.

2. Modelling of the Flexible One-Link Manipulator

2.1. Introduction

This chapter deals with the problem of dynamic modelling of a flexible one-link manipulator. The configuration that is analyzed corresponds to that of an experimental setup built specifically for this research. In Section 2.2, Hamilton's principle is used to obtain an integrated model of the system, including actuator dynamics, and rigid and flexible modes. Section 2.3 presents an analysis of the beam-shaped piezoelectric interaction from the finite element method point of view. The formulation of the state space observation matrix for the flexible manipulator, assuming that encoder feedback and shaped piezoelectric films are used as sensors is presented on section 2.4. The models obtained in this chapter are used in chapter 3 for control design and numerical simulation.

2.2. Lagrangian Dynamics of a Flexible One-Link Manipulator

In this section, the procedure to obtain the dynamic model of a flexible manipulator is shown. A model is developed for the case of a manipulator with one flexible link constrained to acting on a horizontal plane, and which is rigidly attached at one end to the shaft of an electric servomotor. The horizontal motion of the link precludes any contribution of the gravity in the dynamic model. Hamilton's principle, developed

into Lagrange's equation, is used to obtain the dynamic equations from the kinetic and potential energy expressions of the arm. Figure 2.1 shows the coordinate systems employed in the subsequent development:

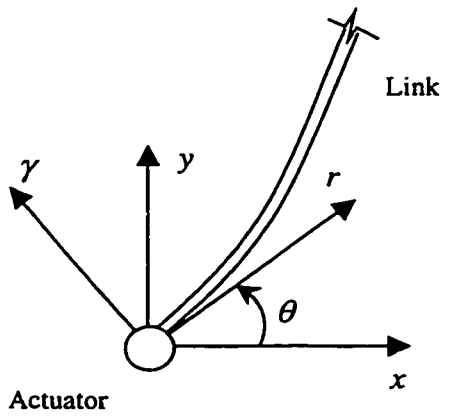

Figure 2.1: Coordinate Systems

Two reference systems are defined:

1. $x-y-z$ system: An inertial system with its origin at the centre of the shaft of the actuator, its z-axis aligned with the shaft, and the x-axis aligned with the home position of the manipulator.
2. $r-\gamma-z$ system: A rotating system, attached to the actuator's shaft, with its z-axis coincident with the inertial system's z-axis and its r-axis tangent to the link at the shaft.

The behaviour of the link relative to the $r-\gamma-z$ system can be analyzed using beam theory. Assuming that the link is a homogeneous slender beam of constant cross-

section, the equations of motion can be found using the Bernoulli-Euler theory. The Bernoulli-Euler beam equation for free vibration can be written as:

$$\rho A_{cs} \frac{\partial^2 \gamma(r,t)}{\partial t^2} + EI_{cs} \frac{\partial^4 \gamma(r,t)}{\partial r^4} = 0$$

where ρ is the density of the beam's material, A_{cs} is the cross-sectional area of the beam, E is the Young's modulus, and I_{cs} is the cross-sectional moment of inertia. The solution of the previous differential equation can be obtained by separation of variables. The relative displacement $\gamma(r,t)$ can be written as:

$$\gamma(r,t) = \sum_{i=1}^{\infty} a_i(t)\, \phi_i(r)$$

where $a_i(t)$ are the *modal coordinates* and $\phi_i(r)$ are the *modes of vibration*. The modes of vibration $\phi_i(r)$ are found as the solutions to the following differential equation, which results from substituting the separated variables form of the solution into the Bernoulli-Euler equation:

$$\frac{d^4 \phi_i}{dr^4} - \frac{\lambda_i^2}{h^2} \phi_i = 0 \quad h = \frac{EI_{cs}}{\rho A_{cs}}$$

where λ_i is the circular frequency of vibration of mode i. The boundary conditions for this problem correspond to those of a clamped-free beam:

$$\text{Clamped end: } \phi_i(0) = 0 \quad \frac{d\phi_i}{dr}(0) = 0$$

$$\text{Free end: } \frac{d^2 \phi_i}{dr^2}(L) = 0 \quad \frac{d^3 \phi_i}{dr^3}(L) = 0$$

For more complex link geometries, the mode shapes and frequencies of vibration have to be found using numerical techniques, such as the finite element method. There

are infinite solutions for the stated problem; the common approach is to truncate the solution to a finite number N of modes that have the most significant contribution to the global behaviour of the system. Using the parameters shown in Table 2.1, which correspond to those of the experimental setup described in section 3.4.1, the mode frequencies and shapes can be obtained. The first four mode shapes and their associated curvatures are shown in Figure 2.2, Figure 2.3 and Figure 2.4 respectively.

Table 2.1: Link Properties

Material	Density ρ (Kg/m^3)	Young's Modulus E (Pa)	Section Shape	Length L (m)	Width W (m)	Thickness t_b (m)
Aluminum	2700	6.9×10^{10}	Rectangular	1.1	0.0514	0.0016

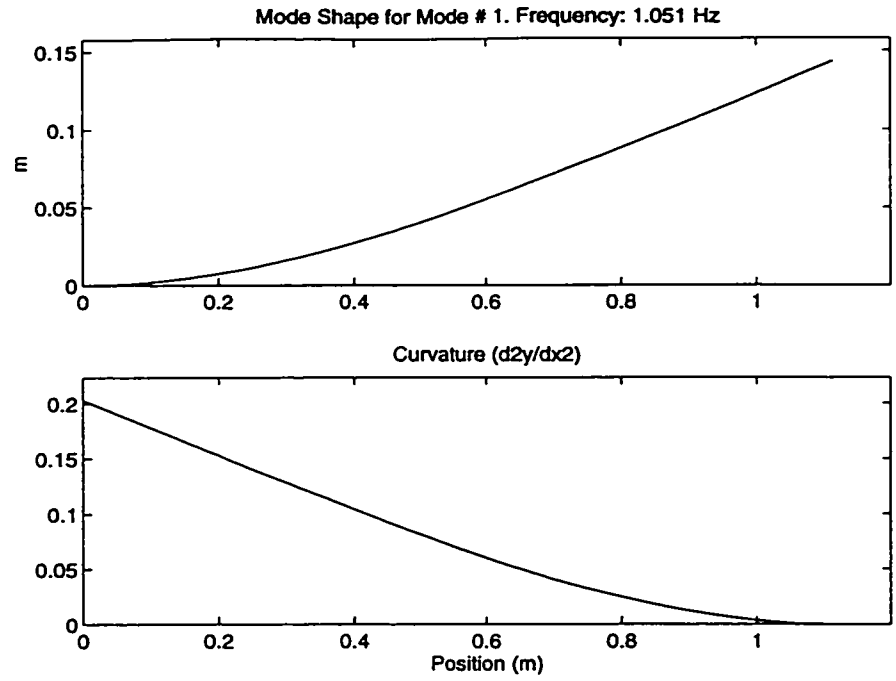

Figure 2.2: 1st Mode Shape and Curvature for Cantilever Beam

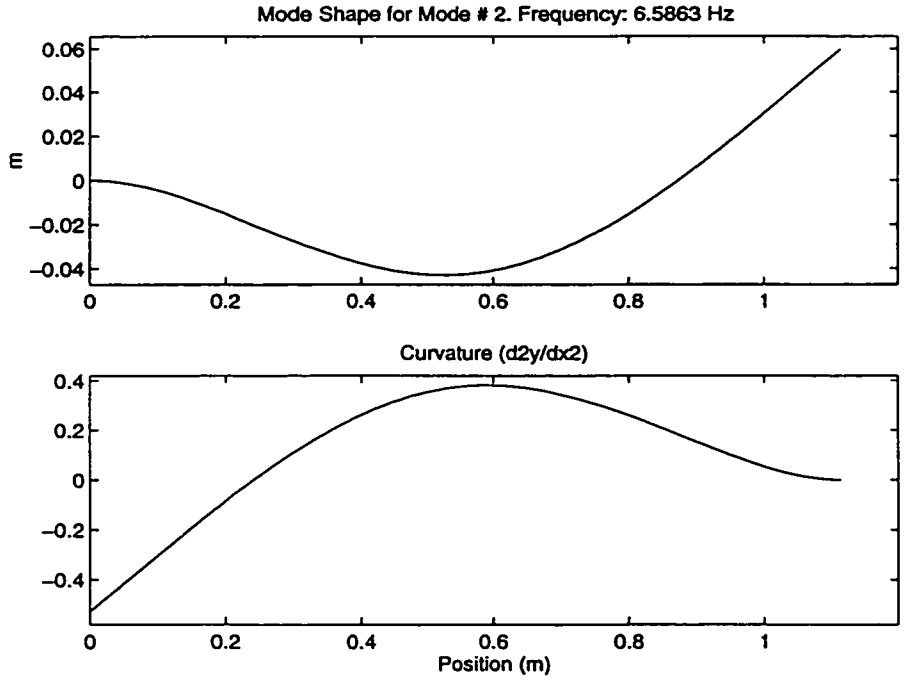

Figure 2.3: 2nd Mode Shape and Curvature for Cantilever Beam

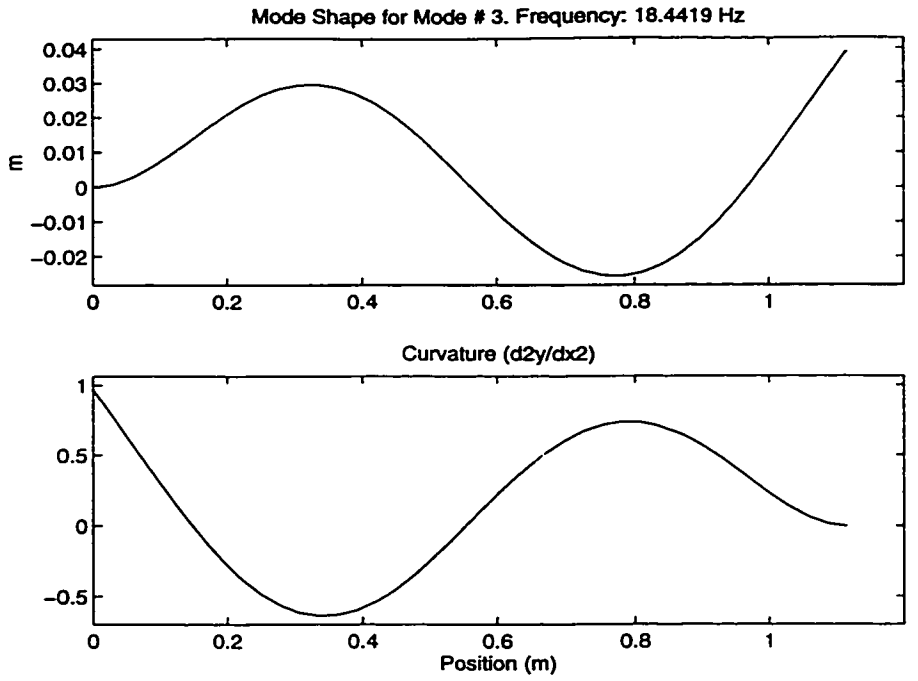

Figure 2.4: 3rd Mode Shape and Curvature for Cantilever Beam

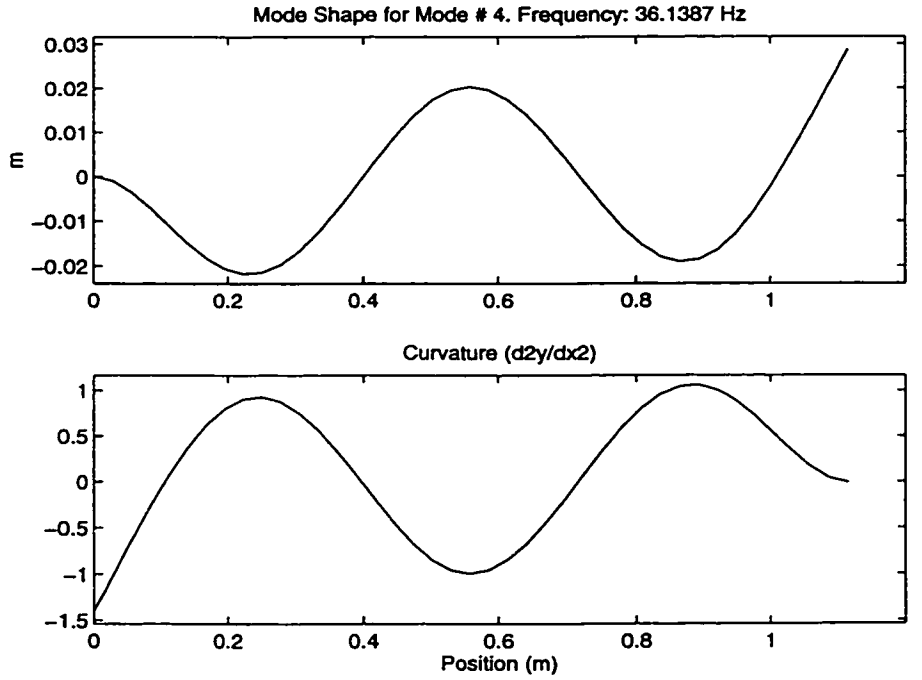

Figure 2.5: 4th Mode Shape and Curvature for Cantilever Beam

Once the relative motion of the link with respect to the rotating reference system has been written in terms of the modal coordinates and mode shapes, the magnitude of the velocity of any point of the link can be obtained as the superposition of the rigid body rotation of the beam plus the flexible motion, as follows:

$$\dot{y}(r,t) = \dot{\theta}(t)\, r + \dot{\gamma}(r,t) = \dot{\theta}(t)\, r + \sum_{i=1}^{N} \dot{a}_i(t)\, \phi_i(r)$$

where $\cdot$ denotes differentiation with respect to t. The kinetic energy of the arm can be written as the sum of rotational and translational components as:

$$T = \frac{J_h \dot{\theta}(t)^2}{2} + \frac{1}{2}\int_0^L \dot{y}(r,t)^2 dm = \frac{J_h \dot{\theta}^2}{2} + \frac{1}{2}\int_0^L \left(\dot{\theta}(t)\, r + \sum_{i=1}^{N} \dot{a}_i(t)\, \phi_i(r) \right)^2 \rho A_{cs} dr$$

The potential energy is stored in the arm as strain energy in the flexible link, and it can be expressed in terms of the mode shapes and modal coordinates as follows:

$$V = \frac{1}{2} EI_{cs} \int_0^L (\gamma''(r,t))^2 dr = \frac{1}{2} EI \int_0^L \left(\sum_{i=1}^{N} a_i(t)\, \phi_i''(r) \right)^2 dr$$

where $'$ denotes differentiation with respect to r. The dynamic model of the system can be found by using Hamilton's Principle:

$$\int_{t_1}^{t_2} \delta(T - V) dt + \int_{t_1}^{t_2} \delta W_{nc} dt = 0$$

where W_{nc} is the work done by non-conservative external forces. The joint angle and the modal coordinates can be grouped to form a vector of generalized coordinates, defined as:

$$q_{N+1\times 1} = \{\theta \quad a_1 \quad a_2 \quad \cdots \quad a_N\}^T$$

Similarly, the torque applied at the joint and the modal forces can be grouped to form a vector of generalized forces. Since there are no modal forces being applied to the system, the vector of generalized forces can be written as:

$$\{Q\}_{N+1\times 1} = \{T \quad 0 \quad 0 \quad \cdots \quad 0\}^T$$

The work done by non-conservative external forces can then be written in terms of the generalized coordinates and forces as:

$$W_{nc} = Q^T q = T \times \theta$$

Since the kinetic and potential energy are already expressed in terms of the vector of generalized coordinates, as follows:

$$T = T(q_i, \dot{q}_i) \quad V = V(q_i)$$

then Hamilton's Principle can be simplified into Lagrange's Equation:

$$\frac{d}{dt}\frac{\partial L}{\partial \dot{q}_i} - \frac{\partial L}{\partial q_i} = Q_i \ , \quad i = 1..N+1$$

where $L = T - V$ is the Lagrangian function of the system, Q_i is the i^{th} element of the vector of generalized forces, and q_i is the i^{th} element of the vector of generalized coordinates. All the elements of the vector of generalized forces are zero, except for the first element, which is equal to the torque, $T = K_u u$, applied by the servomotor. Substituting the expressions for kinetic and potential energy and performing the required operations, one obtains the following matrix equation, which is a set of $N + 1$ ordinary differential equations that model the dynamic behaviour of the system:

$$M\ddot{q} + Kq = fu$$

where u is the control voltage sent to the servomotor amplifier. The system matrices are given by:

$$M = \begin{bmatrix} J_h + \frac{\rho A_{cs} L^3}{3} & \rho A_{cs}\int_0^L \phi_1(r)rdr & \rho A_{cs}\int_0^L \phi_2(r)rdr & \cdots & \rho A_{cs}\int_0^L \phi_N(r)rdr \\ \rho A_{cs}\int_0^L \phi_1(r)rdr & \rho A_{cs}\int_0^L \phi_1^2(r)dr & 0 & \cdots & 0 \\ \rho A_{cs}\int_0^L \phi_2(r)rdr & 0 & \rho A_{cs}\int_0^L \phi_2^2(r)dr & \cdots & \vdots \\ \vdots & \vdots & \vdots & \ddots & \vdots \\ \rho A_{cs}\int_0^L \phi_N(r)rdr & 0 & \cdots & \cdots & \rho A_{cs}\int_0^L \phi_N^2(r)dr \end{bmatrix}$$

$$K = \begin{bmatrix} 0 & 0 & 0 & \cdots & 0 \\ 0 & EI_{cs}\int_0^L (\phi_1''(r))^2 dr & 0 & \cdots & 0 \\ 0 & 0 & EI_{cs}\int_0^L (\phi_2''(r))^2 dr & \cdots & 0 \\ \vdots & \vdots & \vdots & \ddots & \vdots \\ 0 & 0 & 0 & \cdots & EI_{cs}\int_0^L (\phi_N''(r))^2 dr \end{bmatrix}$$

$$f = \{K_u \quad 0 \quad 0 \quad \cdots \quad 0\}^T$$

The motor and hub parameters needed for the numeric calculation of the mass and stiffness matrices are shown in Table 2.2. The link parameters are listed in Table 2.1.

Table 2.2: Motor-Hub Properties

Motor-Fixture Inertia J_h **(Kg-m^2)**	**Friction Coeff.** B_m **(Nm/rad)**	**Motor-Amp. Torque Constant** K_u **(Nm/V)**	**Voltage at Saturation Torque (V)**	**Encoder Gain** K_θ **(V/rad)**
4.11×10^{-3}	6.79×10^{-2}	0.256	1.4	3.18

The effects of actuator friction and the link structural damping can be included in the model via a viscous damping matrix $[H]$, given by:

$$H = \begin{bmatrix} B_m & 0 & 0 & \cdots & 0 \\ 0 & 2\zeta_1 m_{22}\omega_1 & 0 & \cdots & 0 \\ 0 & 0 & 2\zeta_2 m_{33}\omega_2 & \cdots & 0 \\ \vdots & \vdots & \vdots & \ddots & \vdots \\ 0 & 0 & 0 & \cdots & 2\zeta_N m_{N+1,N+1}\omega_N \end{bmatrix}$$

where ω_i, $i = 1..N$ are the clamped-free frequencies of the link, m_{ii} are the corresponding elements of the mass matrix, and ζ_i are the modal damping coefficients. This yields the following modified dynamic model:

$$M\ddot{q} + H\dot{q} + Kq = fu$$

For modelling and control purposes it is convenient to write the model of the system in state-space form, as follows:

$$\dot{x} = Ax + Bu$$

$$y = Cx$$

where the matrices A and B are defined in terms of the stiffness, mass and damping matrices K, M and H, respectively, and the force vector f:

$$A = \begin{bmatrix} 0_{N+1\times N+1} & I_{N+1\times N+1} \\ -[M^{-1}K]_{N+1\times N+1} & -[M^{-1}H]_{N+1\times N+1} \end{bmatrix}_{2(N+1)\times 2(N+1)}$$

$$B = \begin{Bmatrix} 0_{N\times 1} \\ \{M^{-1} f\}_{N\times 1} \end{Bmatrix}_{2N\times 1}$$

The inertia matrix M is positive definite, guaranteeing the existence of M^{-1}. The state space is defined as:

$$x = \begin{Bmatrix} q \\ \dot{q} \end{Bmatrix}$$

The observation matrix C, which relates the state space to the output space, has to be obtained based on the available sensors. In the next sections the C matrix will be found for the cases of a strain gauge sensor and for a shaped piezoelectric film acting as a sensor.

2.3. Finite Element Analysis of Beam-Piezoelectric Interaction

2.3.1 Finite Element Analysis of the Beam

The dynamic behaviour of the beam is simulated numerically using the finite element method [43]. The beam is discretized into a finite number of elements, in which an assumed profile is used to interpolate the value of the degrees of freedom between nodes. A two-node planar beam element is employed, where the degrees of freedom are the traverse displacement and slope at each node, as illustrated in Figure 2.6.

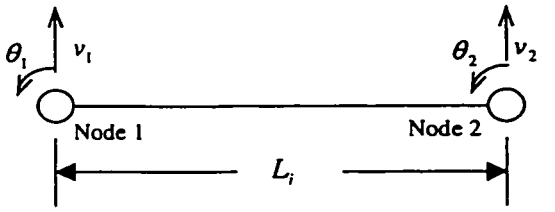

Figure 2.6: Two-Node Planar Beam Element

In this section, subscripts represent element numbers, as opposed to mode numbers for the remaining sections. The displacement is approximated between nodes using the nodal values of the degrees of freedom and the interpolation functions, as follows:

$$v(x,t) = N(x)_i \{q(t)\}_i$$

where

$$N(x)_i = \left[\frac{2x^3 - 3x^2 L_i + L_i^3}{L_i^3} \quad \frac{x^3 L_i - 2x^2 L_i^2 + x L_i^3}{L_i^3} \quad \frac{-2x^3 + 3x^2 L_i}{L_i^3} \quad \frac{x^3 L_i - x^2 L_i^2}{L_i^3} \right]$$

$$q(t)_i = \{q\}_i = [v_1 \ \theta_1 \ v_2 \ \theta_2]_i^T$$

The strain at any point in the cross-section of the beam can be expressed in terms of the vertical displacement as:

$$\varepsilon = -y \frac{d^2 v}{dx^2}$$

where y is the distance between the point and the neutral axis of the cross-section. The strain-displacement matrix can then be found to be

$$B_i = -y\frac{d^2 N_i}{dx^2}$$

The element stiffness and mass matrices may be obtained from the following expressions:

$$\overline{K}_{el\,i} = E_i \int_{V_i} B_i^T \, B_i \, dV$$

$$\overline{M}_{el\,i} = \int_{V_i} \rho_i N_i^T \, N_i \, dV$$

where E_i and ρ_i are the Young's modulus and the density of the material, respectively. Substituting the expression for N_i and performing the required derivations and integrations, the elementary stiffness and mass matrices are defined in terms of the material properties and geometric parameters as:

$$\overline{K}_{el\,i} = \frac{2\,E_i\,I_i}{L_i^3}\begin{bmatrix} 6 & 3L_i & -6 & 3L_i \\ 3L_i & 2L_i^2 & -3L_i & L_i^2 \\ -6 & -3L_i & 6 & -3L_i \\ 3L & L_i^{\,2} & -3L_i & 2L^2 \end{bmatrix}$$

$$\overline{M}_{el\,i} = \frac{\rho_i\,A_i\,L_i}{420}\begin{bmatrix} 156 & 22L_i & 54 & -13L_i \\ 22L_i & 4L_i^{\,2} & 13L_i & -3L_i^{\,2} \\ 54 & 13L_i & 156 & -22L_i \\ -13L_i & -3L_i^{\,2} & -22L_i & 4L_i^2 \end{bmatrix}$$

The load vector for a beam element is composed of the superposition of the effects of concentrated moments and concentrated and distributed forces normal to the length of the beam. The consistent load vector for element i has the form:

$$\overline{f}_{el\,i} = [\, f_1 \;\; m_1 \;\; f_2 \;\; m_2 \,]_i^T$$

If the local axes for an element are not parallel to the global axes, the local matrices and coordinates have to be transformed into the global reference system using rotation matrices. The elementary matrices in the global reference system are found to be:

$$K_{el\,i} = R_i^T \, \overline{K}_{el\,i} \, R_i$$

$$M_{el\,i} = R_i^T \, \overline{M}_{el\,i} \, R_i$$

$$f_{el\,i} = R_i^T \, \overline{f}_{el\,i}$$

where the rotation matrices are

$$R = \begin{bmatrix} \hat{R}_i & 0_{2x2} \\ 0_{2x2} & \hat{R}_i \end{bmatrix} \qquad \hat{R}_i = \begin{bmatrix} \cos\theta_i & \sin\theta_i \\ -\sin\theta_i & \cos\theta_i \end{bmatrix}$$

The global stiffness and mass matrices and the load vector are assembled from the superposition of the effects of the local matrices, taking into account the global numbering of the local nodes in each element. If $k^p_{m,n}$ is the m,n component of the local stiffness matrix of element p, and it contributes to the i,j component $k_{i,j}$ of the global stiffness matrix, the mapping that inserts the components of the local matrices global matrices can be written as:

$$I_{map}(p,m,n) = (i,j)$$

The pre-image of I_{map} is written as

$$I_{map}^{-1}(i,j) = \{(p,m,n) \mid I_{map}(p,m,n) = (i,j)\}$$

It denotes all the element components that contribute to (i,j) in global coordinates. The components of the global stiffness matrix can be found using the inverse insertion map, as follows:

$$k_{i,j} = \sum k^{p}_{m,n}, \quad (p,m,n) \in I_{map}^{-1}(i,j)$$

Assembly of the mass matrix and load vector follows exactly the same approach, using the same inverse mapping for the insertion of local contributions into the global matrices. The dynamic model of the beam is now given by a set of second order differential equations, each one corresponding to a different degree of freedom, and it can be written as follows:

$$M\ddot{q} + Kq = f$$

The effect of concentrated masses and inertias at the nodes is easily accounted for by adding the extra mass and inertia to the diagonal elements of the mass matrix, at the location that corresponds to the translational or rotational degree of freedom where the additional mass and inertia are located.

Before attempting to find a solution for the system, it is necessary to eliminate the rows and columns that correspond to prescribed degrees of freedom. At this point, a direct numerical solution of the system shown before can be obtained, or a modal analysis may be performed to reduce the size of the numerical problem to be solved.

2.3.2 Effect of the Piezoelectric Film on the Beam

The addition of a layer of piezoelectric film bonded to the beam in an open circuit has two distinct effects: It adds additional passive compliance that increases the stiffness of the system, and it creates a stiffness induced by the voltage feedback on the piezoelectric film. The first effect may be modelled using conventional approaches, such as the equivalent cross-sectional area method (Popov [32]), or by adding a stiffness matrix that accounts for the increased rigidity. The second effect is negligible for most usual structure-film pairs.

The analysis that follows is performed to predict the open circuit voltage and short circuit current induced in the piezoelectric when the beam to which it is attached is subject to vibrations. The charge induced in the piezoelectric film by its strain can be determined as the sum of the charge of each element:

$$P = \sum_{i=1}^{\#\ of\ elements} P_i$$

where the charge contributed by each element is obtained from the following expression:

$$P_i = \int_0^L e_{31_i}(x)\varepsilon_{c_i}(x,t)dx$$

$e_{31_i}(x)$ represents the charge to strain ratio of a cross section of element i with a fixed x coordinate, and it can be written as:

$$e_{31_i}(x) = d_{31} E_c W_c \Xi_i(x)$$

The shape function $\Xi_i(x)$ of the film at element i can be written in terms of the same interpolation functions used for the displacement:

$$\Xi_i(x) = N_i\{\phi\}_i = \{\phi\}_i^T N_i^T$$
$$e_{31_i}(x) = d_{31} E_c W_c \{\phi\}_i^T N_i^T \quad ,$$

where $\{\phi\}_i$ is a vector that contains the nodal values of width and slope of the shape function $\Xi_i(x)$:

$$\{\phi\}_i = \left[\phi_{1_i} \quad \frac{d\phi_{1_i}}{dx} \quad \phi_{2_i} \quad \frac{d\phi_{2_i}}{dx} \right]^T$$

The strain distribution of the film can be written using the interpolation functions and the nodal displacements:

$$\varepsilon_{c_i}(x,t) = -y \left. \frac{d^2 v}{dx^2} \right|_{y=\frac{t_b}{2}} = -\frac{t_b}{2} \frac{d^2 N_i}{dx^2} \{q\}_i$$

Substituting the equations of the strain distribution and the strain to charge ratio in the equation for the electric charge, one obtains the following expression for the charge in element i:

$$P_i = -\frac{d_{31} E_c W_c t_b}{2} \int_0^{L_i} \{\phi\}_i^T N_i^T \frac{d^2 N_i}{dx^2} \{q\}_i \, dx = -\frac{e_f t_b}{2} \{\phi\}_i^T \left[\int_0^{L_i} N_i^T \frac{d^2 N_i}{dx^2} dx \right] \{q\}_i$$

where e_f is the film charge to displacement ratio, defined as

$$e_f = d_{31} E_c W_c$$

The integral between the large brackets can be calculated using the given interpolation functions. The result is:

$$\int_0^{L_i} N_i^T \frac{d^2 N_i}{dx^2} dx = \begin{bmatrix} -\frac{6}{5L_i} & -\frac{11}{10} & \frac{6}{5L_i} & -\frac{1}{10} \\ -\frac{1}{10} & -\frac{2}{15L_i} & \frac{1}{10} & \frac{L_i}{30} \\ \frac{6}{5L_i} & \frac{1}{10} & -\frac{6}{5L_i} & \frac{11}{10} \\ -\frac{1}{10} & \frac{L_i}{30} & \frac{1}{10} & -\frac{2}{15L_i} \end{bmatrix}$$

If the piezoelectric film is in open circuit, the voltage at the electrodes is obtained from the total charge and the capacitance of the film, as follows:

$$V = \frac{P}{C_c} \quad , \quad C_c = \frac{\epsilon_c \sum_{i=1}^{NEL} A_{ci}}{t_c}$$

where C_c is the film capacitance and ϵ_c is the permittivity of the film material, and NEL is the number of elements.

2.4. Observation Matrix for the Shaped Piezoelectric Sensor

Consider the cross-section of a rectangular piezoelectric film, as illustrated in Figure 2.7 (Vaz [38]). The 1-axis and 2-axis define a plane which is parallel to the film's surface. The 3-axis is perpendicular to the film's surface. The 3-axis points in the opposite direction to the electric field used to pole the piezoelectric film during its manufacture. Some piezoelectric films, such as polyvinylidene di-flouride (PVDF), are

uniaxially stretched during the poling process. In such a case the 1-axis is oriented in the direction of the uniaxial stretching. Piezoelectric films which are uniaxially stretched exhibit properties which differ in the directions of the 1 and 2 axes (e.g., $d_{31} \neq d_{32}$).

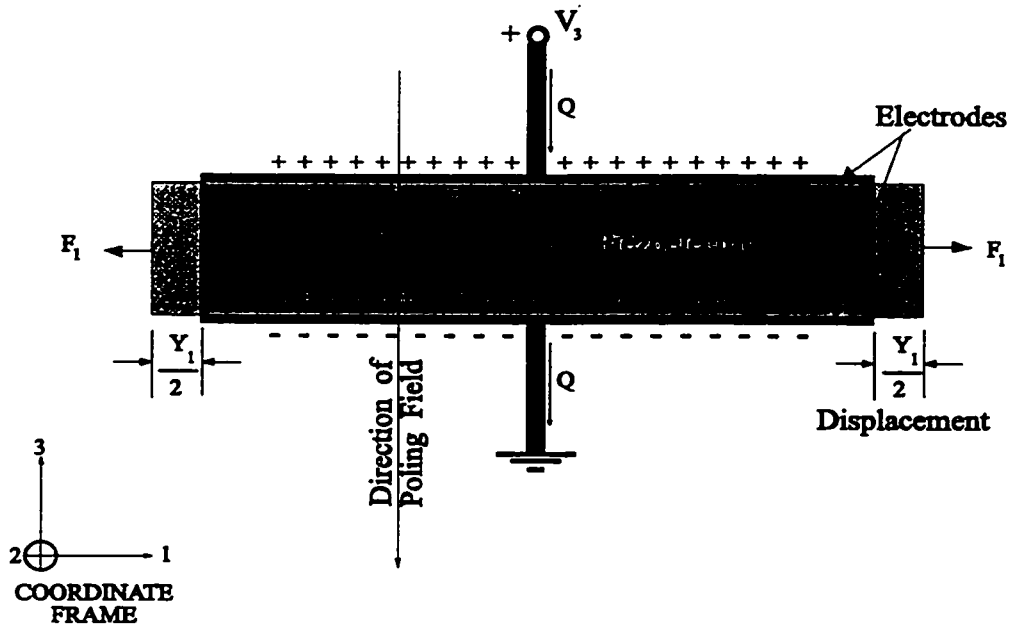

Figure 2.7: Cross Section of a Piezoelectric Film

Films which are not uniaxially stretched, such as piezoceramics, do not exhibit these differences. The transverse effects in piezoelectric films are illustrated in Figure 2.7. The film is assumed to have a length L_c along the 1 axis, a width W_c along the 2 axis, and a thickness t_c along the 3 axis. A voltage V_3 is measured across the upper and lower electrodes. The upper and lower electrodes are assumed to have free charges of $+Q$ and $-Q$ respectively. A tensile force F_1 and an elongation displacement Y_1 are measured along the 1 axis. If the film acts as an actuator, a voltage V_3 is applied across the film; the induced polarization in the piezoelectric generates a tensile force F_1 and an

elongation Y_1. If the film is used as a sensor, a tensile force F_1 is applied which stretches the film by Y_1; the induced polarization in the piezoelectric causes an increase of free charges on the contacts which generates a voltage V_3 through a capacitive effect.

In (Vaz [41]), it is shown that a piezoelectric film's behaviour can be modelled by

$$\begin{aligned} Y_1 &= s_f^E F_1 + d_f V_3 \\ Q &= d_f F_1 + c_f^T V_3 \end{aligned} \tag{2.1}$$

where s_f^E is interpreted as the film compliance at constant electric field intensity; d_f, the film charge to force ratio; and c_f^T, the film capacitance at constant stress. The above film parameters are defined as follows:

$$s_f^E := \frac{L_c}{E_c W_c t_c} \qquad d_f := \frac{d_{31} L_c}{t_c} \qquad c_f^T := \frac{\in_c L_c W_c}{t_c}$$

where E_c is the Young's modulus of the piezoelectric, $\in_c$ is the permittivity of the piezoelectric at a constant stress, and d_{31} is the transverse piezoelectric charge to stress ratio.

Equation (2.1) can be represented in terms of the electromechanical models based on force and voltage. The charge generated by applying a tensile force to a piezoelectric film is modelled by the circuit in Figure 2.8a. The circuit in Figure 2.8b is obtained by applying Thévenin's theorem to the circuit in Figure 2.8a. In Figure 2.8c, the mechanical tensile force F_1 is balanced by the mechanical reaction force of an elongated spring of stiffness $1/s_f^E$. The net elongation of the spring is given by subtracting the piezoelectric

displacement $d_f \cdot V_3$ from the mechanical displacement Y_1. It is clear from the inverted voltage source in the circuit of Figure 2.8b that the charge generated by the piezoelectric effect causes a negative piezoelectric displacement in the mechanical model in Figure 2.8c. Thus the piezoelectric effect augments the mechanical stiffness of the film.

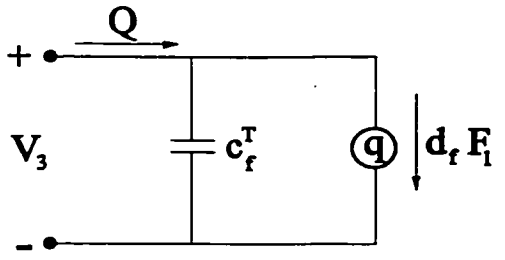

(a) Charge Model

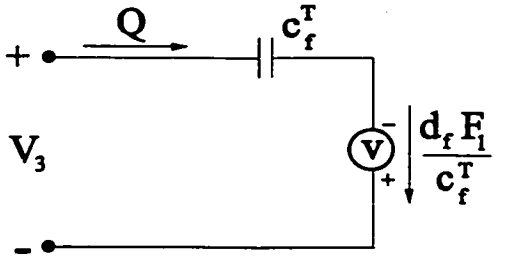

(b) Voltage Model

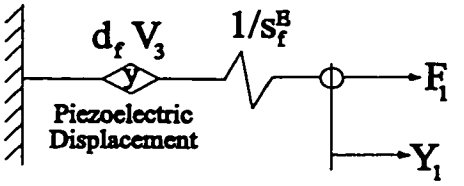

(c) Mechanical Model

Figure 2.8: Electromechanical Models Based on Force F_1 and Voltage V_3

In (Vaz [41]), it is shown that piezoelectric films can also be modelled in terms of voltage and displacement:

$$\begin{aligned} F_1 &= \left(\frac{1}{s_f^E}\right) Y_1 - e_f V_3 \\ Q &= e_f Y_1 + c_f^S V_3 \end{aligned} \tag{2.2}$$

where c_f^S is interpreted as the film capacitance at constant strain; and e_f, the film charge to displacement ratio. The above parameters are defined as follows:

$$c_f^S := c_f^T - \frac{d_f^2}{s_f^E} = \left(\varepsilon_c - d_{31}^2 E_c\right)\left(\frac{L_c W_c}{t_c}\right) \qquad e_f := \frac{d_f}{s_f^E} = d_{31} E_c W_c$$

Equation (2.2) can be represented in terms of the electromechanical models based on displacements and voltages. The charge generated by stretching a piezoelectric film is modelled by the circuit in Figure 2.9a. The circuit in Figure 2.9b is obtained by applying Thévenin's theorem to the circuit in Figure 2.9a. In Figure 2.9c, the relation between mechanical reaction force and mechanical displacement Y_1 is modelled by a spring of $1/s_f^E$. The net force exerted on the spring is the sum of the mechanical tensile force F_1 and the piezoelectric force $e_f V_3$.

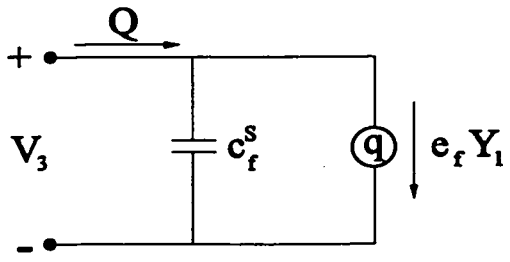

(a) Charge Model

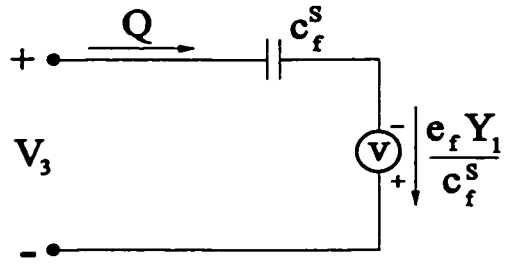

(b) Voltage Model

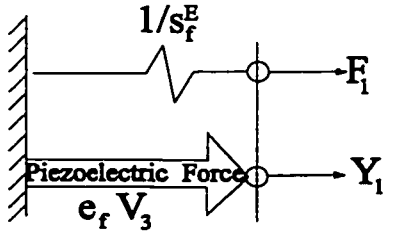

(c) Mechanical Model

Figure 2.9: Electromechanical Models Based on Displacement Y_1 and Voltage V_3

Vaz [38],[41] shows that a shaped film can be idealized as a rectangular piezoelectric film which has a poling direction that varies throughout the film, and electrodes that are etched into geometrical shapes. At any point in a shaped film, the poling direction may either point up or down. The electrode shapes are such that a point in the piezoelectric film may or may not be covered by both electrodes. The properties of a shaped film are determined by the pattern of the poling direction variation and the electrode geometry.

A shaped film can be constructed from several electrically connected contiguous sections of piezoelectric films. The orientation of the polling direction varies between sections. The piezoelectric sections are bonded to an electrical insulator which is bonded to the beam. The inner electrodes are inaccessible. Copper tape leads with adhesive epoxy are used to make electrical contact with the inner electrodes. The outer electrodes can be etched into geometrical patterns.

Shaped films are analyzed in terms of variations of the poling direction and domain of the outer electrodes. The functions used to represent these quantities are expressed in terms of the coordinate system of the beam to which they are attached. The coordinate system of the beam is shown in Figure 2.10. The x, y, z coordinate frame has its origin on the neutral surface of the beam. The beam has a length L along the x axis, a width W along the y axis, and a thickness t_b along the z axis. The upper and lower surfaces of the beam have z coordinates of $t_b/2$ and $-t_b/2$, respectively.

The shaped film is bonded to the beam as shown in Figure 2.10. The film is situated between $x = a - m$ and $x = a + m$ in the x axis and $y = 0$ and $y = W_c$. The z

coordinate of the beam surface, to which the film is bonded, is denoted by z_c. If the beam is bonded to the top surface, $z_c = t_b/2$; otherwise, $z_c = -t_b/2$ for the lower surface.

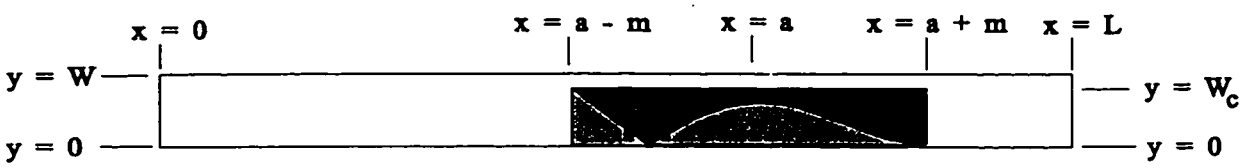

Figure 2.10: Top View of Piezoelectric Film Bonded to a Flat Beam

The bending strain of the flat beam shown in Figure 2.10 varies only in the x and z directions. Hence beam strain ε_b can be represented as a function $\varepsilon_b(x,z,t)$. Note the strains have the following antisymmetric property:

$$\varepsilon_b(x,-z,t) = -\varepsilon_b(x,z,t)$$

Accordingly, the strain in a cross section of the piezoelectric film can be represented by a function $\varepsilon_c(x,z_c,t)$. The strain variations of ε_c in the z direction are negligible due to the thinness of the piezoelectric film. The piezoelectric film is assumed to be perfectly bonded to the beam; hence:

$$\varepsilon_c(x,z_c,t) = \varepsilon_b(x,z_c,t)$$

In practice, the errors incurred by this simplifying assumption are typically negligible (Vaz [41]).

The properties of a shaped film are characterized in terms of a domain function $F(x,y)$ and poling function $P(x,y)$.The domain function $F(x,y)$ defines the region of a shaped film's etched electrode:

$$F(x,y) := \begin{cases} 1, & \text{point } (x,y) \text{ is covered by both} \\ & \text{electrodes of the film;} \\ 0, & \text{otherwise.} \end{cases}$$

The poling direction is specified with respect to the electric field intensity associated with a particular electrode polarity. The electric field intensity points from the positive electrode to the negative electrode. The poling direction is aligned with the electric field if it points towards the negative electrode. The poling function $P(x,y)$ specifies the variations of the poling direction throughout the shaped film:

$$P(x,y) := \begin{cases} +1 & \text{poling direction at } (x,y) \\ & \text{points towards - electrode;} \\ 0, & \text{the film does not cover } (x,y); \\ -1 & \text{poling direction at } (x,y) \\ & \text{points towards + electrode.} \end{cases}$$

The function $F(x,y)$ basically defines which areas of the film are active while the poling function, $P(x,y)$, indicates the output polarity of that region. The shape function $\Xi(x)$) of a shaped film is the average of the poling function $P(x,y)$ over a cross section of a particular x coordinate. It is defined by

$$\Xi_c(x) := \frac{1}{W_c} \int_0^{W_f} P(x,y)dy$$

The area covered by the film's electrodes is given by

$$A_c = \int_{a-m}^{a+m} \int_{0}^{W_c} F(x,y)dy.$$

The capacitance of the film is given by

$$C_c = \frac{\in_c A_c}{t_c},$$

where $\in_c$ is the permittivity of the piezoelectric, and t_c is the film thickness.

When the shaped film is strained, an electric flux density is created due to the polarization in the piezoelectric. The electric flux varies in the x direction but not the y direction. Integrating electric flux gives charge $Q_c(t)$, given by

$$Q_c(t) = -d_{31}E_c W_c \int_{a-m}^{a+m} \Xi_c(x)\varepsilon_c(x,z_c,t)dx$$

The above equation is derived by applying equation (2.2) and the circuit in Figure 2.9a to an infinitesimal element.

For a given strain profile, $\varepsilon_c(x,z_c,t)$, the corresponding open circuit voltage $V_{oc}(t)$ and the short circuit current $I_{sc}(t)$ are respectively given by

$$V_{oc}(t) = -\frac{d_{31}E_c W_c}{C_c} \int_{a-m}^{a+m} \Xi_c(x)\varepsilon_c(x,z_c,t)dx$$

and

$$I_{sc}(t) = -d_{31}E_c W_c \int_{a-m}^{a+m} \Xi_c(x)\frac{\partial \varepsilon_c(x,z_c,t)}{\partial t}dx$$

The strain profile can be expressed in modal terms as:

$$\varepsilon_c(x,z_c,t) = -\text{sgn}(z_c)\times\frac{t_b}{2}\left(\sum_{i=1}^{n}\frac{d^2\phi_i(x)}{dx^2}q_i(t)\right)$$

where z_c is the coordinate from the neutral axis of the beam to the piezoelectric film and $\Phi_i(x)$ and $q_i(t)$ are the i^{th} mode shape and modal amplitude respectively. The strain rate is given by:

$$\frac{\partial\varepsilon_c(x,z_c,t)}{\partial t} = -\text{sgn}(z_c)\times\frac{t_b}{2}\left(\sum_{i=1}^{n}\frac{d^2\phi_i(x)}{dx^2}\frac{dq_i(t)}{dt}\right)$$

Substituting the modal expressions for strain and strain rate into the open circuit voltage and short circuit current expression yield:

$$V_{oc}(t) = \sum_{i=1}^{n} Q_i^{V_{oc}}\, q_i(t) \tag{2.3}$$

$$I_{sc}(t) = \sum_{i=1}^{n} Q_i^{I_{sc}}\, \dot{q}_i(t) \tag{2.4}$$

where

$$Q_i^{V_{oc}} := \text{sgn}(z_c)\times\frac{d_{31}E_cW_ct_b}{2C_c}\times\int_{a-m}^{a+m}\Xi_c(x)\frac{d^2\phi_i(x)}{dx^2}dx$$

$$Q_i^{I_{sc}} := \text{sgn}(z_c)\times\frac{d_{31}E_cW_ct_b}{2}\times\int_{a-m}^{a+m}\Xi_c(x)\frac{d^2\phi_i(x)}{dx^2}dx$$

The operation of a modal sensor can be understood from equations (2.3) and (2.4). Suppose the sensor film is shaped such that

$$\Xi(x) = \mu\hat{\Xi}(x)$$

where

$$\hat{\Xi}(x) = \frac{\dfrac{d^2\Phi_i(x)}{dx^2}}{\displaystyle\int_0^{L_b}\left(\frac{d^2\Phi_i(x)}{dx^2}\right)^2 dx}$$

and

$$\mu^{-1} = \max_{0\le x\le L_b}\left|\hat{\Xi}(x)\right|$$

The film is assumed to have a length equal to that of the beam; that is, $a = L_b/2$ and $m = L_b/2$. From the orthogonality property of the mode shapes, and from equations (2.3) and (2.4), it follows that

$$V_{oc}(t) = \mu\left(\frac{d_{31}E_cW_c}{2C_c}\right)q_i(t)$$

and

$$I_{sc}(t) = \mu\left(\frac{d_{31}E_cW_c}{2}\right)\dot{q}_i(t)$$

Hence, such a sensor film can be used either to produce a voltage, that is proportional to the amplitude of mode i, or a current, that is proportional to the amplitude rate of mode i (Lee *et al.* [24]).

The ability to observe particular modes in a beam can be used to implement a modal feedback control law in terms of a film's shape. Suppose a film is shaped so that

$$\Xi(x) = \mu\hat{\Xi}(x)$$

where

$$\hat{\Xi}(x) = \sum_{i=1}^{n} K_i \left(\frac{\dfrac{d^2\Phi_i(x)}{dx^2}}{\displaystyle\int_0^{L_b} \left(\frac{d^2\Phi_i(x)}{dx^2} \right)^2 dx} \right) \tag{2.5}$$

and

$$\mu^{-1} = \max_{0 \le x \le L_b} \left| \hat{\Xi}(x) \right|$$

The open circuit voltage is given by

$$V_{oc}(t) = \mu \left(\frac{d_{31} E_c W_c}{2C_c} \right) \sum_{i=1}^{n} K_i q_i(t) \tag{2.6}$$

which is proportional to the feedback

$$u_q = \sum_{i=1}^{n} K_i q_i(t)$$

The short circuit current is given by

$$I_{sc}(t) = \mu \left(\frac{d_{31} E_c W_c}{2} \right) \sum_{i=1}^{n} K_i \dot{q}_i(t) \tag{2.7}$$

which is proportional to the feedback

$$u_{\dot{q}} = \sum_{i=1}^{n} K_i \dot{q}_i(t)$$

Assuming that there are an angular encoder and two films attached to the flexible link, one measuring open circuit voltage and another measuring short circuit current, the sensors output vector

$$\{y\} = \begin{Bmatrix} V_\theta \\ V_q \\ V_{\dot{q}} \end{Bmatrix}$$

where V_q and $V_{\dot{q}}$ are voltage signals proportional to the open circuit voltage and short circuit current measured in the piezoelectric films, with proportionality constants of β and γ, respectively. The observation matrix $[C]$ for the state-space model of the manipulator is given by

$$[C] = \begin{bmatrix} K_\theta & [0]_{1\times n} & 0 & [0]_{1\times n} \\ 0 & \beta[Q^{V_\alpha}] & 0 & [0]_{1\times n} \\ 0 & [0]_{1\times n} & 0 & \gamma[Q^{I_\alpha}] \end{bmatrix}$$

where

$$[Q^{V_\alpha}] = [Q_1^{V_\alpha} \quad Q_2^{V_\alpha} \quad \cdots \quad Q_n^{V_\alpha}]$$

$$[Q^{I_\alpha}] = [Q_1^{I_\alpha} \quad Q_2^{I_\alpha} \quad \cdots \quad Q_n^{I_\alpha}]$$

2.5. Summary

In this chapter, the dynamic model of a flexible one link manipulator was obtained. Lagrange's formula and the assumed modes method was used to obtain the model using generalized variables obtained from a modal analysis of a cantilever beam.

A finite element analysis of the piezoelectric-beam interaction in the sensor application was performed, including the effect of shaping the sensor. A relation was found that allows for the design of sensors that provide a specific linear combination of modal amplitudes and the gains, thus giving a feedback signal that can be used for control purposes. The state space observation matrix of the shaped piezoelectric sensor was deducted in terms of the state space variables. This will allow for the development in chapter 3 of a controller using the ability to shape the sensors and obtain modal sensors to produce state feedback controllers that are able of stabilizing the manipulator in presence of link flexibility.

3. Control of the Flexible One-Link Manipulator

3.1. Introduction

In this chapter, the synthesis and design of a robust control system for a flexible one link manipulator are presented, taking advantage of the use of shaped piezoelectric sensors. In section 3.2 the theoretical development of an optimal H_∞ static state feedback controller using linear matrix inequality (LMI) techniques is shown. In section 3.3, numerical simulation results of the dynamic model of the manipulator obtained in chapter 2 are presented, using the controller design obtained in this chapter. The results obtained in the simulations are validated by the experimental results presented in section 3.4; details of design and construction of the experimental setup used for this purpose are shown and discussed.

3.2. H_∞ Feedback Controller Synthesis

A robust H_∞ feedback controller was designed for the flexible link manipulator based on linear matrix inequality (LMI) design techniques obtained by Gahinet [20]. The design objective of the H_∞ control technique is to minimize the H_∞ norm of the closed loop from w to z. This is desired because the H_∞ norm is idempotent with the induced L_2-L_2 norm, which represents the maximum energy gain from the input space to the

output space. The H_∞ norm of a stable transfer function is defined by its largest gain across the frequency range:

$$\|G(s)\|_\infty := \sup_\omega \sigma_{\max}(G(j\omega))$$

To obtain the controller using this technique, the dynamic model of the system is to be written in lower Linear Fractional Transformation (LFT) form. This formulation framework is convenient because it allows for the inclusion of the effects of sensor and control disturbances, as well as loop-shaping weights on the inputs and outputs in a very compact and straightforward way. Figure 3.1 shows the block representation of the lower LFT form of the control problem

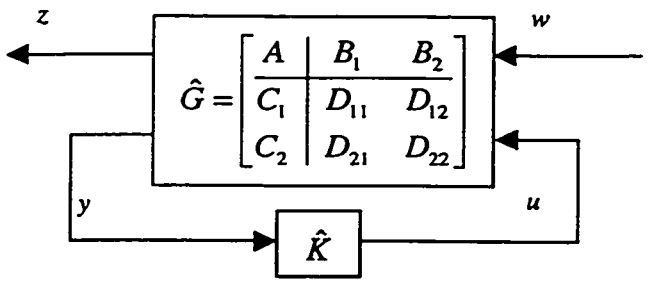

Figure 3.1: Lower LFT Representation of Control Problem

From this figure, it is possible to obtain the relation between the exogenous and controlled outputs z and y, the exogenous and control inputs w and u, and the system matrices:

$$\dot{x} = Ax + B_1 w + B_2 u$$
$$z = C_1 x + D_{11} w + D_{12} u$$
$$y = C_2 x + D_{21} w + D_{22} u$$

It can be shown that, assuming the complete state-space is available for measurement, the state feedback controller that minimizes the H_∞ norm of the closed loop is given by:

$$\hat{K} = D_K, \; D_K = YX^{-1}$$

where $X>0$ and Y are solutions to the following Linear Matrix Inequality (LMI):

$$\begin{bmatrix} B_1 \\ D_{11} \end{bmatrix} \begin{bmatrix} B_1^* & D_{11}^* \end{bmatrix} + \begin{bmatrix} \begin{bmatrix} A & B_2 \end{bmatrix} \begin{bmatrix} X \\ Y \end{bmatrix} + \begin{bmatrix} X & Y^* \end{bmatrix} \begin{bmatrix} A^* \\ B_2^* \end{bmatrix} & \begin{bmatrix} X & Y^* \end{bmatrix} \begin{bmatrix} C_1^* \\ D_{12}^* \end{bmatrix} \\ \begin{bmatrix} C_1 & D_{12} \end{bmatrix} \begin{bmatrix} X \\ Y \end{bmatrix} & -I \end{bmatrix} < 0$$

The LMI problem as stated above is convex and can be solved numerically. The LMILab toolbox of Matlab contains functions to solve this type of problem. The next step in the control design process is to write the dynamic model of the manipulator in lower LFT form. Figure 3.2 shows the conventional block diagram of the closed loop flexible manipulator system, including the sensor noise and disturbances to the control:

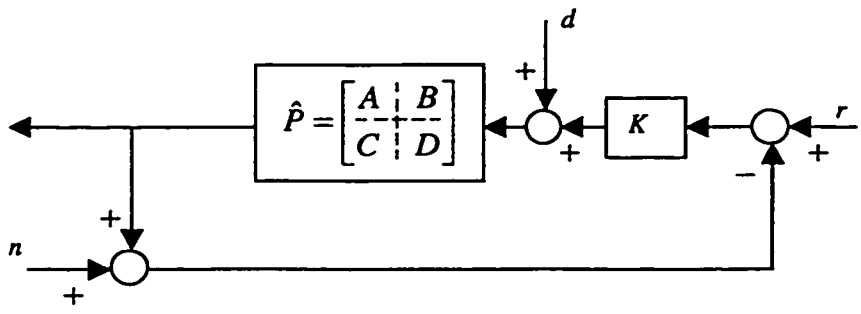

Figure 3.2: Block Diagram of the Closed Loop System

From this figure, it can be seen that the exogenous input vector is comprised of the reference signal r, the control disturbance d and the sensor noise n. Choosing the output vectors to contain the full state x and the control signal u allows shaping the open loop to improve the performance of a particular part of the state and the control. The resulting external input and output vectors are:

$$w = \begin{Bmatrix} r \\ d \\ n \end{Bmatrix} \quad z = \begin{Bmatrix} x \\ u \end{Bmatrix}$$

Based on Figure 3.2, the lower LFT system matrices are given by

$$B_1 = [B \quad 0_{N\times N}] \qquad B_2 = B$$

$$C_1 = \begin{bmatrix} I_{N\times N} \\ 0 \end{bmatrix} \qquad D_{11} = 0_{N+1\times N+1} \qquad D_{12} = \begin{bmatrix} 0_{N\times 1} \\ 1 \end{bmatrix}$$

$$C_2 = I_{N\times N} \qquad D_{21} = [0_{N\times 1} \quad I_{N\times N}] \; D_{22} = D$$

3.3. Numerical Simulations

3.3.1 Controller Design

For the numerical simulations of this controller, the dynamic model developed in chapter 2 is employed, together with the parameters shown in Table 2.1 and Table 2.2. For simulation purposes, the first ten flexible modes of the beam were included in addition to the rigid (rotary) modes. For control design purposes only the first two modes were taken into account. In this way, the effects of observation and control spillover on the higher modes can be observed. The numerical simulations were performed using Matlab and Simulink using the techniques shown in section 3.2. The open loop transfer function can be shaped using weights on the inputs and outputs to improve the response of the controller for certain conditions, as shown in:

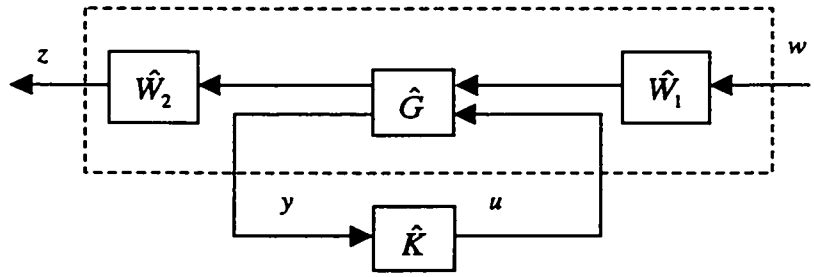

Figure 3.3: Shaping of the Open Loop

No weights were applied to the inputs of the system. Thus, the input weight matrix W_1 is the identity matrix. The output weight matrix is a constant penalty on the state and control effort, with the purpose of improving the performance on certain elements of the state, while maintaining a reasonable bound on the control signal. The matrix employed in this case for the output weights is then:

$$\hat{W}_2 = \begin{bmatrix} 1 & 0 & 0 & 0 & 0 & 0 & 0 \\ 0 & 1 & 0 & 0 & 0 & 0 & 0 \\ 0 & 0 & 1 & 0 & 0 & 0 & 0 \\ 0 & 0 & 0 & 0.5 & 0 & 0 & 0 \\ 0 & 0 & 0 & 0 & 0 & 0 & 0 \\ 0 & 0 & 0 & 0 & 0 & 0 & 0 \\ 0 & 0 & 0 & 0 & 0 & 0 & 0.05 \end{bmatrix}$$

Performing the control design procedure as explained earlier results in the following controller:

$$u = u_M + u_q + u_{\dot{q}}$$

where

$$u_M = 4.2613(\theta^{ref} - \theta) - 3.1103\dot{\theta}$$
$$u_q = -0.0321q_1 + 21.2564q_2$$
$$u_{\dot{q}} = -0.6238\dot{q}_1 + 2.2264\dot{q}_2$$

The term u_M provides feedback of the rigid body states, while the terms u_q and $u_{\dot{q}}$ provide the feedback of the flexible states: modal amplitudes and modal rates, respectively.

The shaped piezoelectric sensors that provide the desired ratio of gains for open circuit voltage and short circuit current is obtained using equation (2.5). The resulting shapes are shown in Figure 3.4:

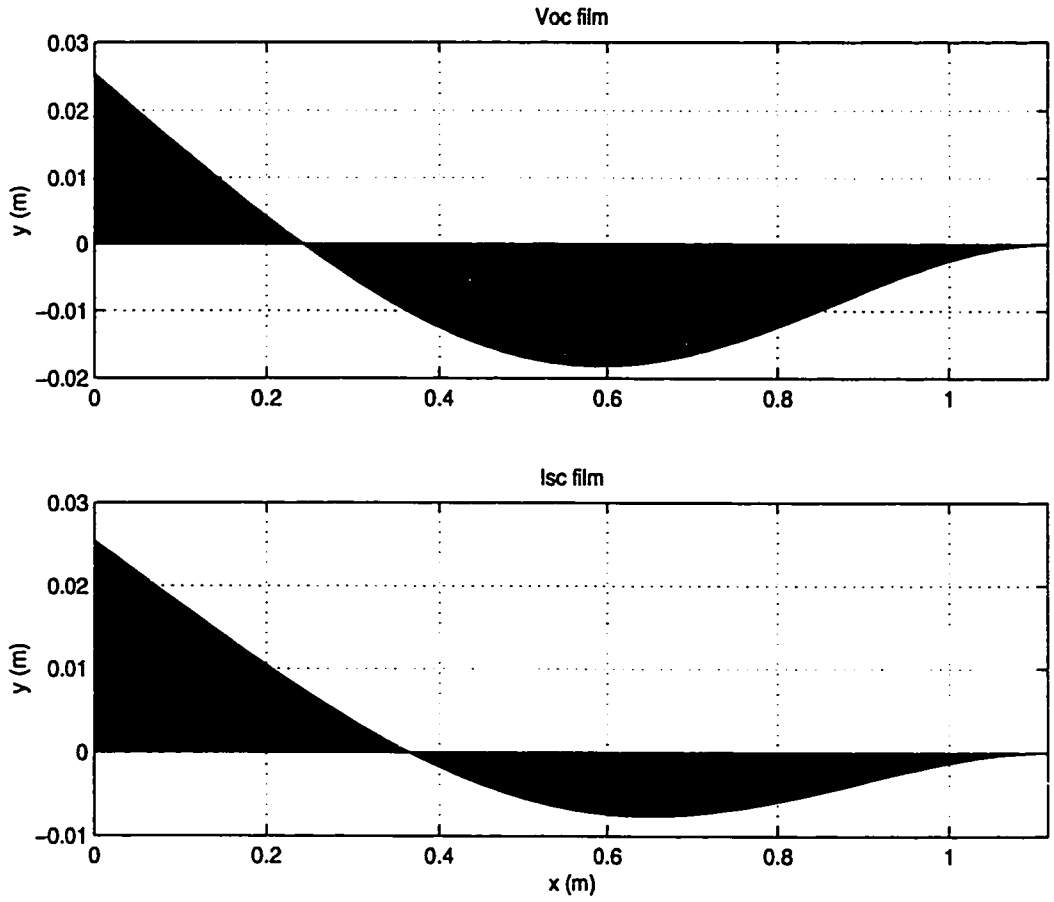

Figure 3.4: Shape of PE Films for H_∞ Control Design

It is important to notice that the width of the sensors along the length of the beam is arbitrarily scaled. Ideally, the film should be as wide as possible, to obtain the best signal to noise ratio. The desired value of the gain has to be recovered via amplification (or attenuation) of the signal. In this case, the maximum width for both films was set to

2.54 cm, half the width of the beam. The case of change of sign in the shape of the piezoelectric was implemented by splicing the film at the sign change point and reversing the polarity of the electrode.

3.3.2 Simulation Results

Two sets of results are shown in this section. The first corresponds to the controller as obtained in the previous section, including the feedback of the flexible states as sensed by the shaped piezoelectric sensors. The response of the system to a step reference input in the angle is shown in Figure 3.5, Figure 3.6 and Figure 3.7 for the joint angle, piezoelectric sensors, and control signal respectively. The joint angle is commanded to move from –57.3 degrees to 57.3 degrees at t=3 s. The model includes the effect of actuator saturation, but the simulations show that the controller is still capable of stabilizing the system with a minimal amount of deflection to the beam. Due to the saturation of the actuator, the beam initially has a large deflection, but as soon as the control signal goes within the unsaturated range, the controller picks up the oscillations and damps them quickly.

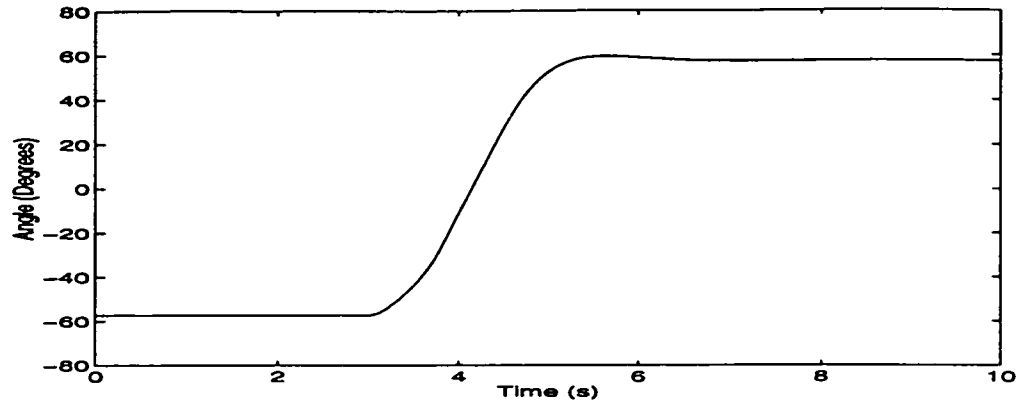

Figure 3.5: Step Response: Joint Angle (Simulation)

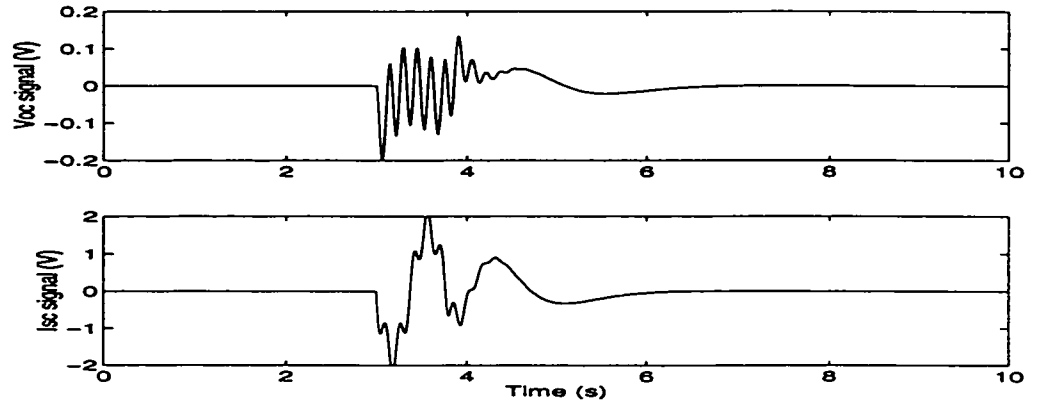

Figure 3.6: Step Response: PE Sensor Signals (Simulation)

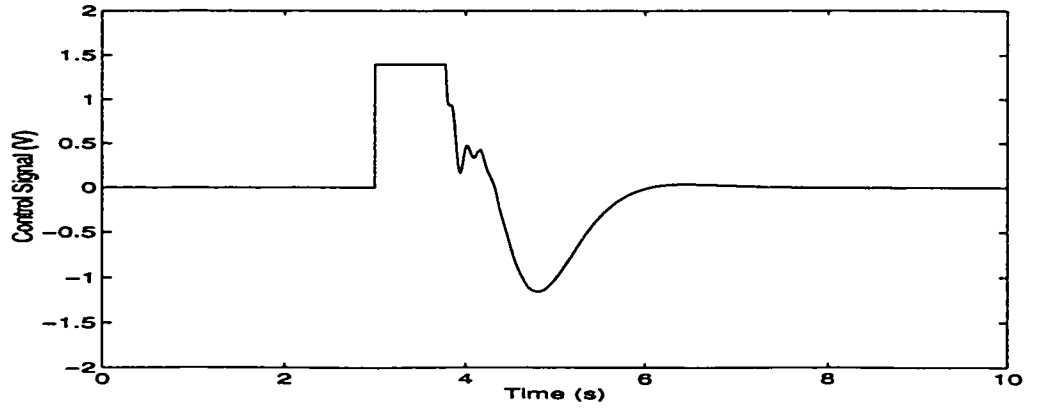

Figure 3.7: Step Response: Control Signal (Simulation)

The second set of results corresponds to the case of no feedback of flexible states. This is done to visualize the amount of performance improvement attained when using the feedback of the shaped piezoelectric sensors. The controller used for this simulation is the same used in the previous simulation, but without the terms u_q and $u_{\dot{q}}$ Figure 3.8, Figure 3.9 and Figure 3.10 show the response of the system to a step reference angle identical to the previous case. The controller is still stable, but the oscillations induced on the link due to the initial impulse are damped out much more slowly, only due to the structural damping and to a lesser extent, due to the cross coupling between the rigid body and flexible states.

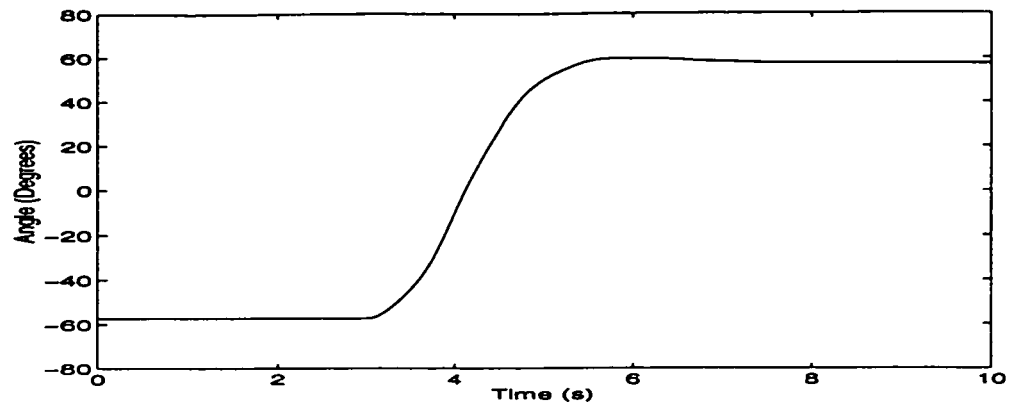

Figure 3.8: Step Response: Joint Angle (Simulation). No PE Feedback

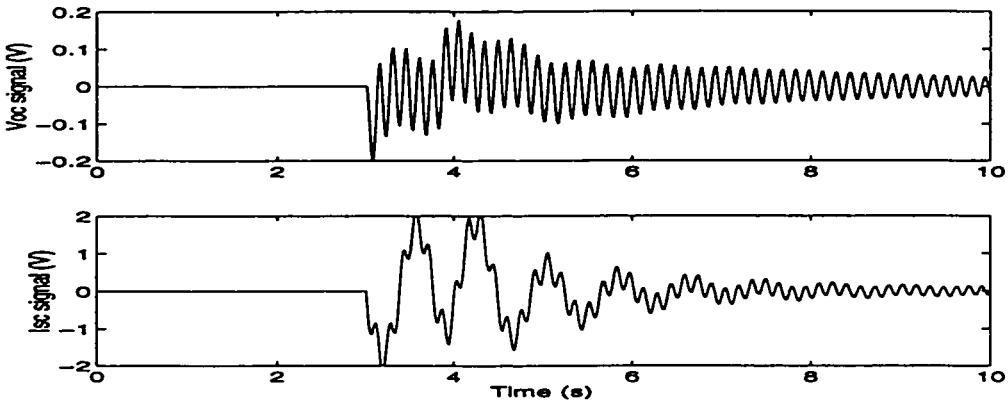

Figure 3.9: Step Response: PE Sensor Signals (Simulation). No PE Feedback

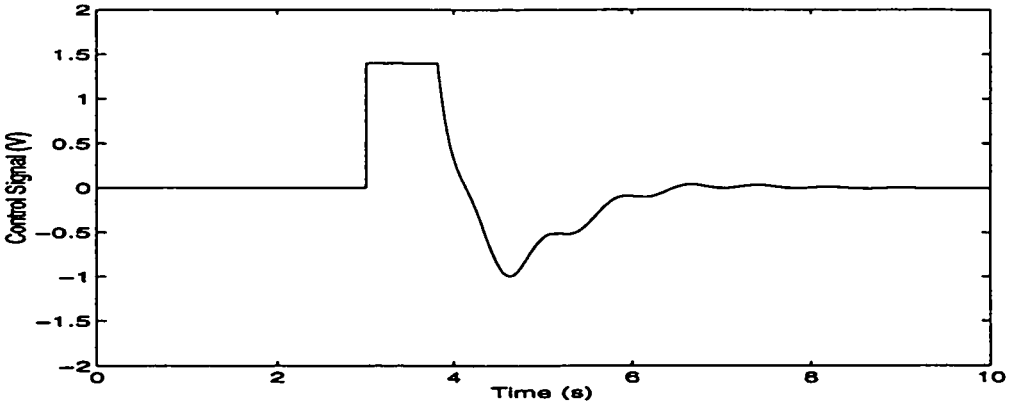

Figure 3.10: Step Response: Control Signal (Simulation) No PE Feedback

3.4. Experimental Verification

3.4.1 Experimental Setup Configuration

A one-link flexible manipulator setup was built to compare the simulations with experimental results. A picture of the system is shown in Figure 3.11:

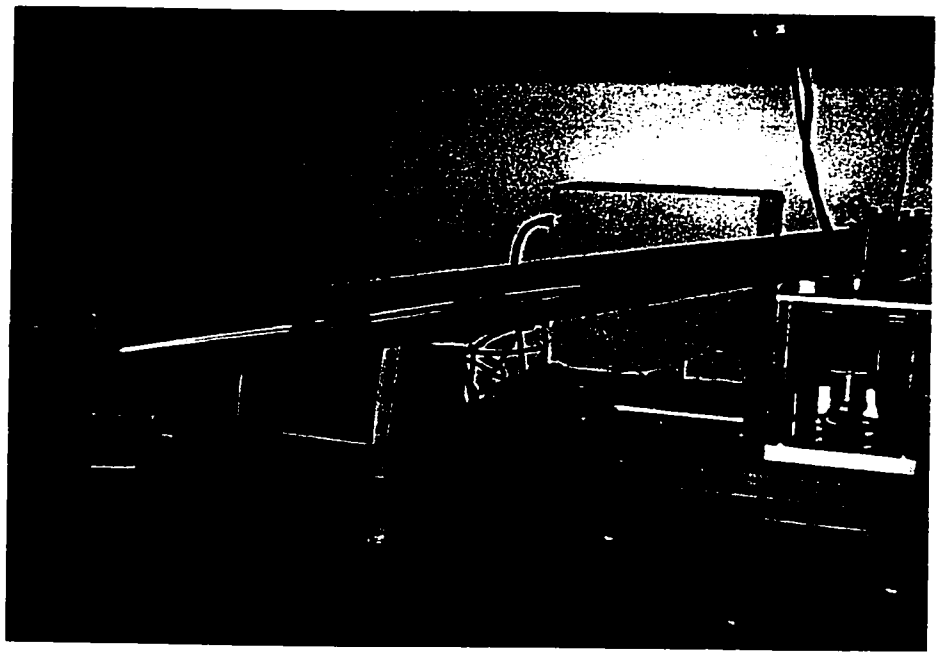

Figure 3.11: Experimental Setup

The one-link flexible manipulator setup was fitted with shaped piezoelectric films, with the shape of the films as given in Figure 3.4, to compare the simulations with experimental results. The specifications of the actuator and link correspond to those given in Table 2.1 and Table 2.2. There are several issues that need to be examined: the effect of imprecision in the shape of the film on the performance; robustness of the controller to

parametric uncertainty, namely unknown payload and effect of control spillover on the unmodelled high frequency modes. Figure 3.12 shows a schematic of the signal flow for this experiment.

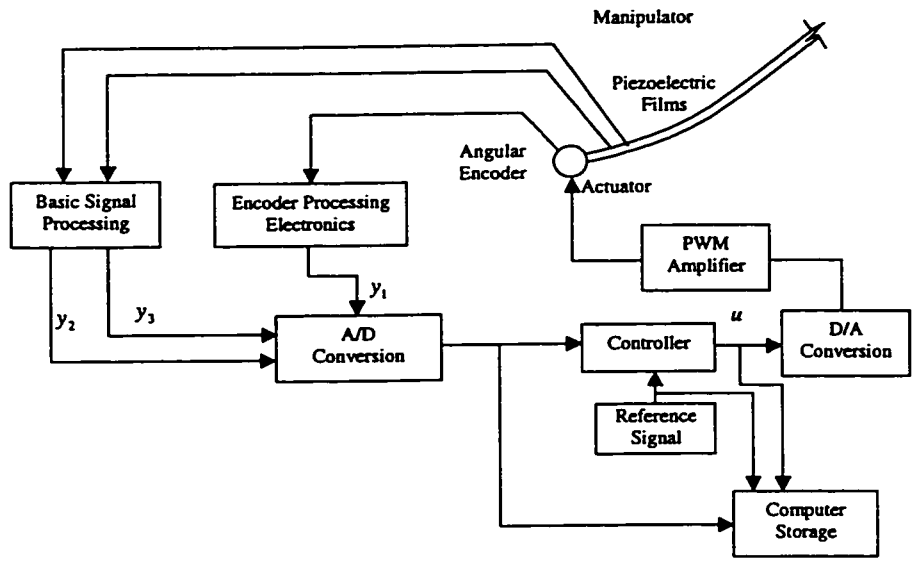

Figure 3.12: Signal Flow Diagram for H_∞ Control Experiment

The controller is implemented on a Pentium based system, using Quanser Consulting Wincon software to interface the A/D-D/A card to Matlab/Simulink. The A/D-D/A card is a Quanser MultiQ, capable of sampling frequencies of 2 kHz, although for this experiment, it was set at 1 kHz.

The link is driven directly by a permanent magnet DC servomotor. A rotary shaft encoder with a resolution of 2400 lines per revolution is used for angle measurement. The angular velocity, not available for measurement, is obtained by differentiation followed by low-pass filtering of the angle measurement.

The piezoelectric films are interfaced to the AD-D/A card using the circuits illustrated in Figure 3.13 and Figure 3.14. The circuits are constructed using a LF351 operational amplifier, which has high impedance FET input nodes. In order to function properly each input must have a DC current path. The circuit in Figure 3.13 is used to buffer the open circuit voltage V_{oc} of the piezoelectric film. The non-inverting terminal has a resistor R_{in} = 33 MΩ to provide a DC current path. The circuit outputs a voltage V_{ma} that is equal to the voltage V_{oc}.

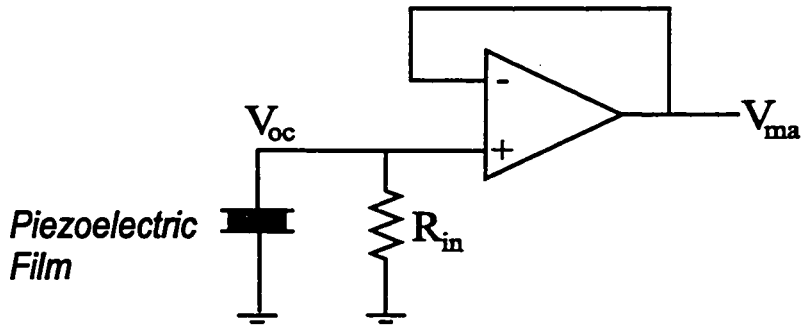

Figure 3.13: Electronic Circuit for Measuring Open Circuit Voltage V_{oc}

The circuit in Figure 3.14 is used to amplify the short circuit current of the piezoelectric film I_{sc}. The circuit outputs a voltage V_{mr} that is proportional to I_{sc}. In particular,

$$V_{mr} = -R_f I_{sc}$$

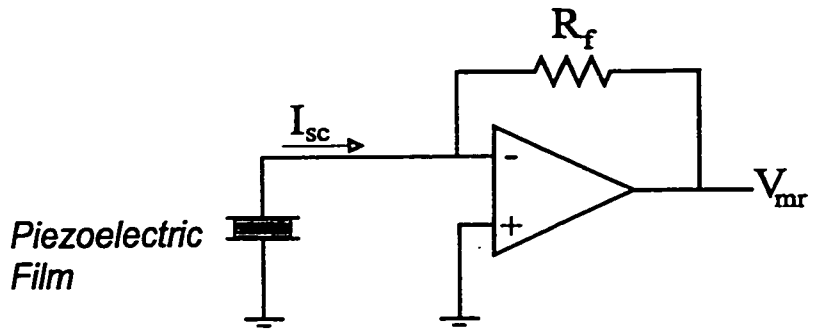

Figure 3.14: Electronic Circuit for Measuring Short Circuit Current I_{sc}

3.4.2 Shaping and Bonding Techniques for the Piezoelectric Sensor

The piezoelectric material used for sensing purposes is Polyvinylidene Di-Fluoride (PVDF) film, with silver ink metallization. Some relevant properties of the PVDF film employed are shown in Table 3.1:

Table 3.1: Mechanical and Electrical Properties of PVDF film

Thickness t_c (μm)	Strain Constant d_{31} (m/m)/(V/m)	Young's Modulus E_c (N/m^2)	Capacitance C_c (F/cm^2)
28	23×10^{-12}	2×10^{9}	379×10^{-12}

To obtain a precise shape, as needed for the implementation of the control law shown in Figure 3.4, development of a good shaping technique is needed. After testing different approaches, the following method, which is a modification of the technique presented in Farr [18], was employed:

1) The desired shaped is printed into paper, using the shape data obtained from the control design process described in section 3.2. Adobe Postscript coding is employed to insure dimensional consistency. Since the shapes are to cover a complete beam, this means that the complete shape requires 6 segments printed on individual sheets of 8.5x11" paper.

2) 3M brand Kapton tape was applied to a non-stick backing. Since the available Kapton tape is 1 inch wide, the maximum width of the shaped film was limited to this dimension.

3) The silhouette of the shape printed in paper is lightly attached to the Kapton tape using transparent tape applied to the edges of the actual shape.

4) The shape is then cut accurately into the Kapton tape by cutting though the paper, tape and backing at the same time to obtain the shaped Kapton tape mask.

5) The Kapton tape mask is attached to the PVDF film using its own adhesive. Care has to be taken on the side of the PVDF film to which the Kapton template is to be attached, to assure that the right polarity is used.

6) The electrode material that is not covered by the Kapton tape mask is removed using a solvent such as acetone and a cotton swab.

7) The Kapton tape template remains in place to protect the top electrode from contamination or damage. Holes can be cut through the Kapton tape to provide for connections and leads at the adequate locations.

The fabrication sequence is shown in Figure 3.15. This technique proved to be optimal because it avoids the problem of electrode shorting that occurs when the PVDF is cut to the exact shape directly. It is also more precise, because it is easier to cut intricate shapes in Kapton tape than in PVDF film.

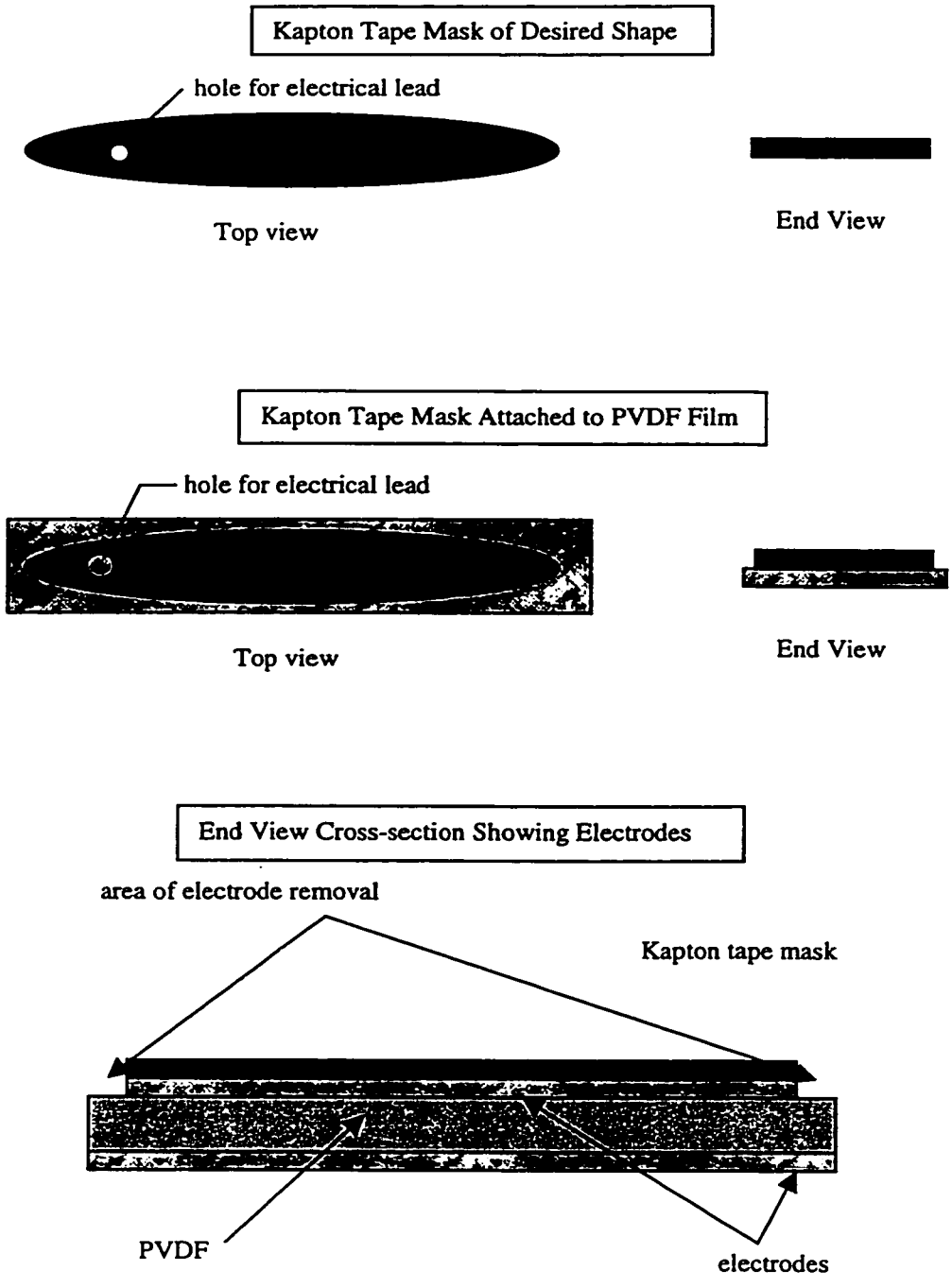

Figure 3.15: Fabrication sequence for Shaped Film

As mentioned before, the complete sensor consists of multiple segments that are individually made following the procedure just described. This is done for two reasons: the sensor is too long to be cut from one PVDF sheet, since the supplier only provides PVDF sheets of up to 8.5x11" size. Also, there are polarity inversions that correspond to sign changes in the shape, which require interruptions in the continuity of the shaped film to produce poling field direction changes. A two-segment shaped film is shown in Figure 3.16. Note that the PVDF film itself is of arbitrary shape; the active portion of the film is given by the portion of it that is located between the shaped electrodes.

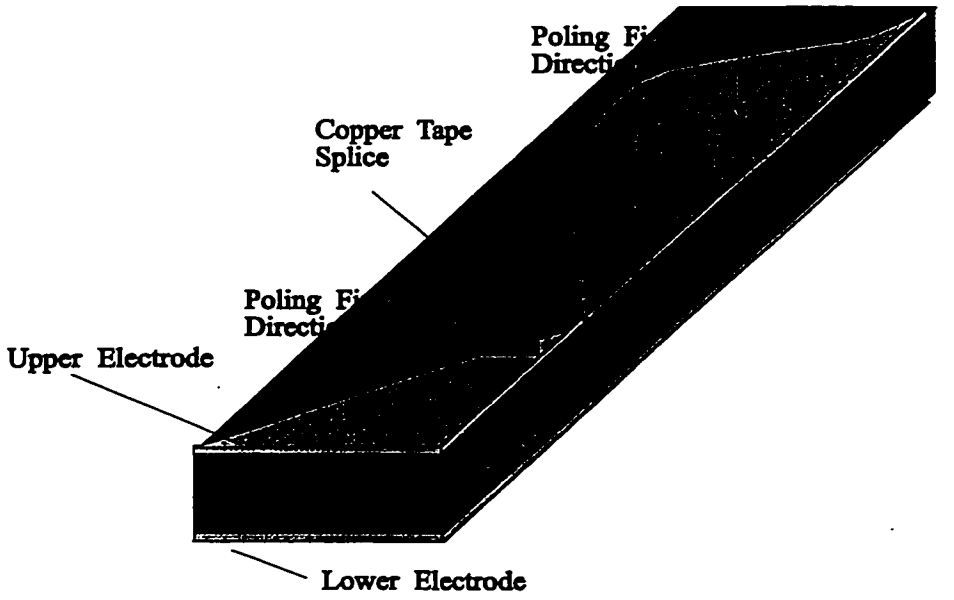

Figure 3.16: Multi-segment Shaped PVDF Film

In order to bond the shaped PVDF film to the beam, a layer of Kapton tape is applied to the beam to provide electrical insulation between the beam and the bottom electrode of the film. Since the bottom part of the film is going to be permanently attached to the beam, the electrical leads have to be installed before the bonding. For this purpose, copper tape with conductive adhesive is employed. The segments of the shaped

film are then individually bonded to the beam using cyanoacrylate glue, taking care to avoid the entrapment of air bubbles between the film and the beam, that can distort the performance of the sensors. Figure 3.17 shows a cross-section of the beam and the sensor, showing the layers of Kapton tape, glue and PVDF film.

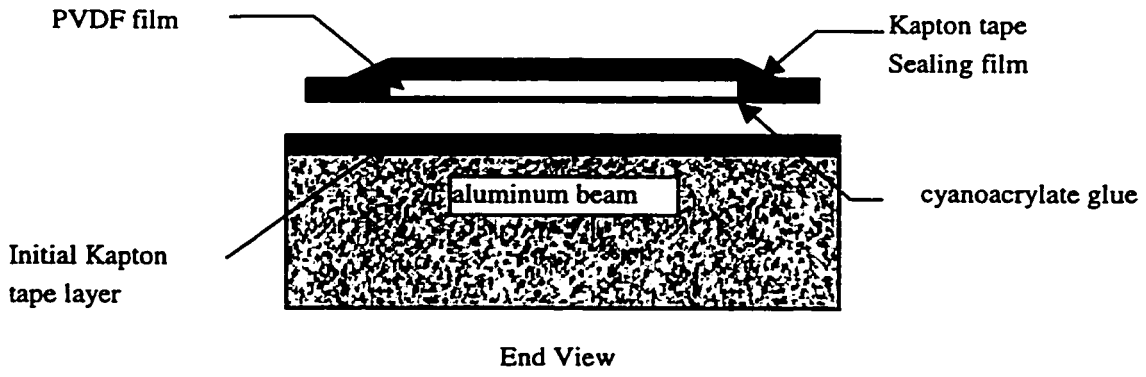

Figure 3.17: Bonding of PVDF Film to Beam

3.4.3 Experimental Results

Figure 3.18, Figure 3.19 and Figure 3.20 show the joint angle, piezoelectric sensor, and control signal response, respectively, to a step input. The step input is identical to the one applied in the simulations presented in section 3.3.2. The response of the system matches well with the simulations, showing that the controller is capable of driving the link while at the same time stabilizing the oscillations with small deflections. As discussed in the simulation results sections, due to the low saturation torque of the actuator employed, the oscillations of the link are not suppressed until the gross angular error is overcome and the control signal returns to the non-saturated range. At this point, the controller immediately contains the oscillations, as shown in the plot of the piezoelectric sensor signals.

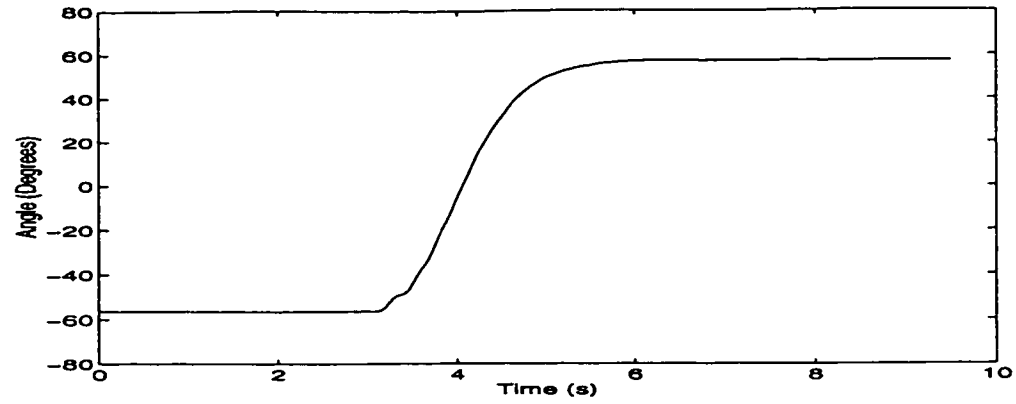

Figure 3.18: Step Response: Joint Angle (Experimental)

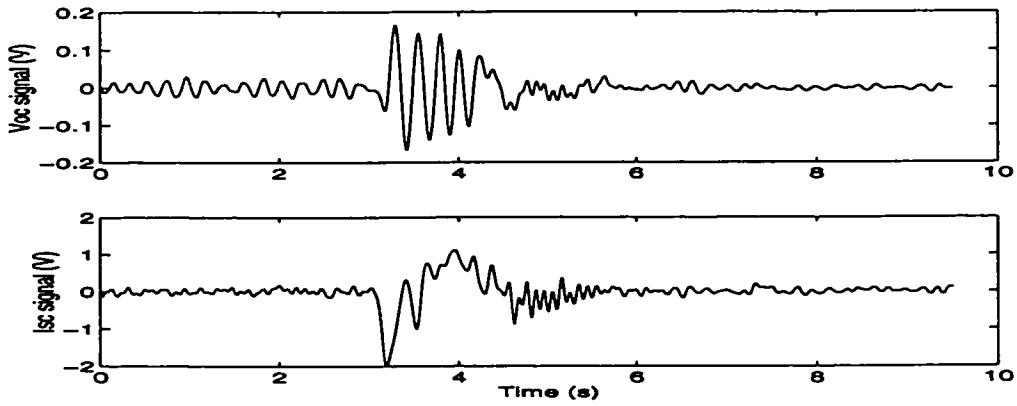

Figure 3.19: Step Response: PE Sensor Signals (Experimental)

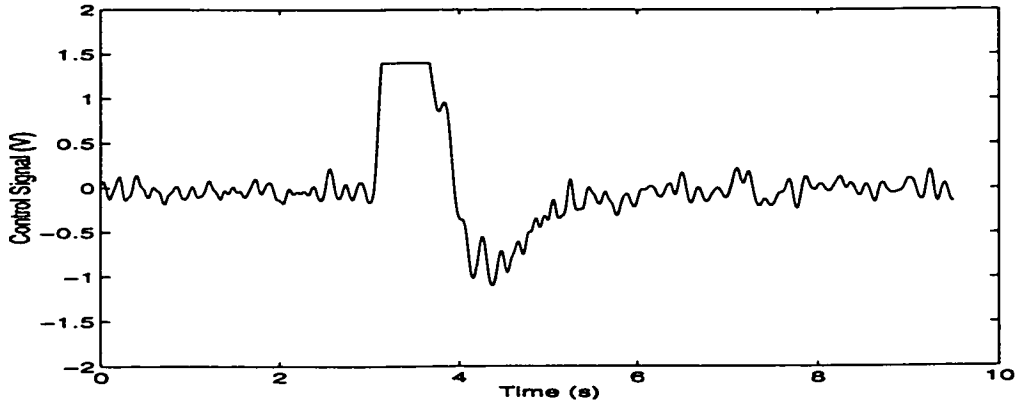

Figure 3.20: Step Response: Control Signal (Experimental)

3.5. Summary

In this chapter, the development of a control strategy for the flexible link manipulator was presented. A robust H_∞ state feedback controller was designed using LMI techniques, and was implemented using shaped PVDF films for modal strain and modal strain rate feedback. Numerical simulations of the closed loop system were performed, which showed that the controller was capable of improving the performance of the manipulator when compared to the case of no flexible states feedback. The settling time of the oscillations of the tip of the manipulator is decreased from $t_s > 7$ s to $t_s < 2$ s.

An experimental setup for the validation of the simulation results was designed and built, together with the development of techniques for the shaping and bonding of the PVDF piezoelectric sensors. The experimental results obtained confirm the findings of the previous sections, matching well with simulations and showing the feasibility of the proposed approach.

4. Design and Modelling of a Truss Structure

4.1. Introduction

In this chapter, the design and mathematical modelling of a truss structure is presented and explained. The truss structure is designed to have a configuration and behaviour that resembles that of a Large Flexible Space Structure (LFSS), that are known to suffer from poorly damped, low frequency, clustered modes of vibration.

The design and mathematical model obtained in this chapter are used in later chapters for control design, numerical simulations and as a basis for the experimental testbed used for validation of the results. Also developed in this chapter are the relations that describe the behaviour of piezoelectric sensors and actuators in terms of finite element and modal models of the system. In section 4.2, a description of the design of the structure, including design requirements to be met, is shown. A detailed finite element-modal analysis of the truss structure is presented in section 4.3, including a rod element model for numerical simulation and control design and a beam element model for validation of the design. Section 4.4 presents the formulation of the state space dynamic model, based on the rod element model obtained in section 4.3, and including the observation and control matrices based on the interaction equations between the piezoelectric actuators and sensors and the structure.

4.2. Configuration Geometry

A truss structure was designed to be a testbed for evaluating potential control techniques for LFSS using piezoelectric actuators and sensors. The design criteria for the selection of the final configuration were the following:

a) similarity to structures used in flexible structure literature;

b) at least 10 modes under 100 Hz.;

c) the first 5 modes of vibration should not include local bending of truss members; and

d) cost, weight, actuation power requirements.

The structure is constructed from polycarbonate tubing of 12.7 mm outer diameter, connected at the nodes to joining blocks. The polycarbonate material was selected because of its advantages over metals such as aluminum and steel in this application, in particular: cost, machinability, light weight, strength, electrical properties, ease of bonding using solvents such as methylene chloride. Table 4.1 shows the mechanical properties and the dimensions of the polycarbonate tubes to be used in the structure, including the parameters that are needed for the finite element simulation. The configuration of the structure is shown in Figure 4.1 (dimensions are shown in m).

Table 4.1: Dimensions and Mechanical Properties of Polycarbonate Tubing

Material	Outside Diameter (mm)	Thickness (mm)	Young's Modulus (N/m^2)	Density (kg/m^3)
Polycarbonate	12.7	1.5875	2.35×10^9	1.2×10^3

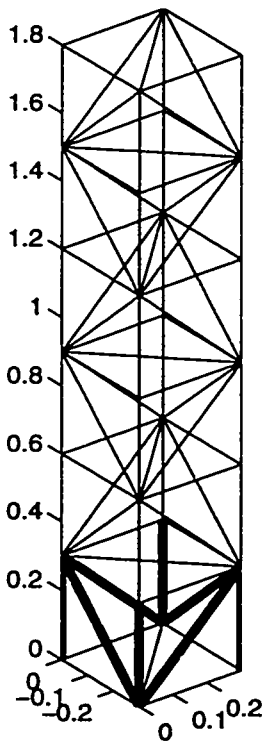

Figure 4.1: Configuration of the Truss Structure

The truss structure is vertically cantilevered at the bottom, and it is composed of six vertical bays, each a 300-mm cube. The thick lines represent the active truss members, i.e.. those that are fitted with sensors and actuators. Not all the active truss members are to be used in the control design simultaneously. The design was iterated until the desired design criteria were met. The structure is approximately 1800 mm high. Figure 4.2 shows a detailed view of two bays of the structure, showing more clearly the topology of the truss. At each junction there is a joining block, also made of polycarbonate material. A detailed view of the design of the joining blocks is shown in

Figure 4.3, while Figure 4.4 shows how the tubular elements are joined together at the junctions.

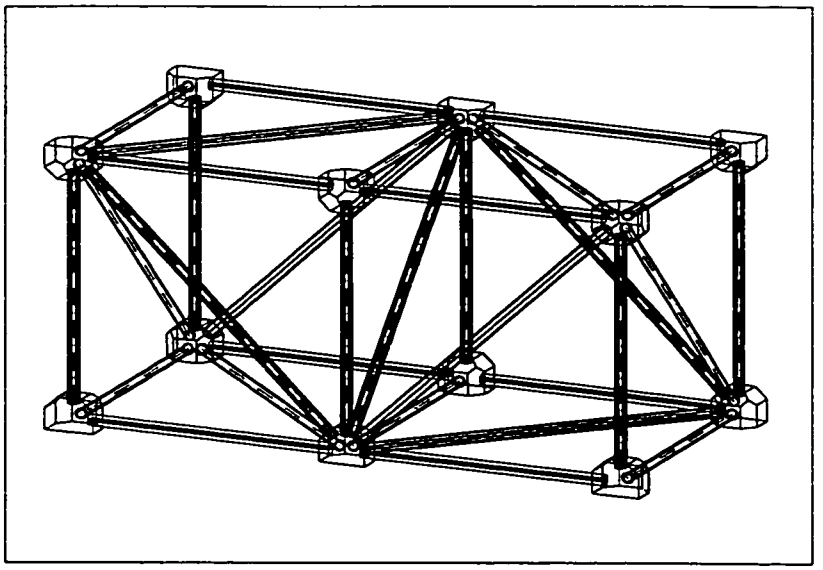

Figure 4.2: Detail of Two Bays

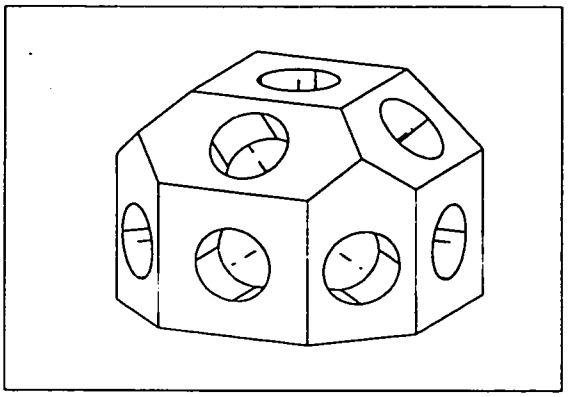

Figure 4.3: Joining Block

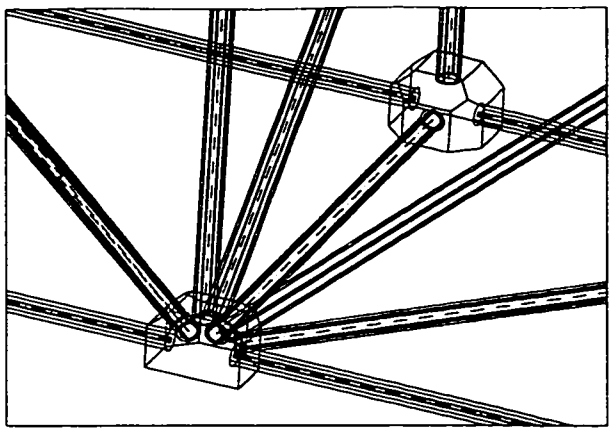

Figure 4.4: Detail of Joints

4.3. Finite Element and Modal Analysis of the Truss Structure

In the finite element method, a continuous structure is discretized into a finite number of elements (Weaver [43]). This converts the dynamics of the continuous structure with infinite number of degrees of freedom to a finite dimensional representation. The discretized structure has dynamics that are characterized by a system of ordinary differential equations, whereas the continuous structure dynamics are characterized by a system of partial differential equations.

The result of a finite element discretization of a structure is a system of ordinary differential equations, which are called the system model:

$$M\ddot{q} + Kq = F$$

where q is the physical coordinate vector; M is a constant, positive definite mass matrix; K is a constant, positive semi-definite stiffness matrix; and F is a vector of actuation forces and torques applied to the structure. It is always possible to find a matrix Φ, called

the modal matrix, whose columns are the normalized eigenvectors of the matrix $M^{-1}K$, such that

$$\Phi^T M \Phi = I$$

$$\Phi^T K \Phi = \Lambda$$

where Λ is a diagonal matrix of squared modal frequencies. The modal matrix Φ defines a coordinate transformation from the modal coordinate vector η to the physical coordinate vector q, that is,

$$q = \Phi \eta$$

Substituting this in the system model and pre-multiplying by Φ^T, the system model yields the modal model of the system:

$$\Phi^T M \Phi \ddot{\eta} + \Phi^T K \Phi \eta = \Phi^T F$$

which is equivalent to

$$\ddot{\eta} + \Lambda \eta = \Phi^T F$$

To account for structural damping, a diagonal modal damping matrix H can be added. The resulting augmented system is:

$$\ddot{\eta} + H\dot{q} + \Lambda \eta = \Phi^T F$$

This form of the model has the advantage that it is uncoupled due to the diagonality of the matrices Λ and H. The damping matrix H can be determined from either material properties or experimentation.

The modal dynamic model can be converted into state space form, which is the canonical form used for control design purposes and simulation. The state space model is given by:

$$\dot{x} = Ax + Bu$$
$$y = Cx$$

with

$$x = \begin{Bmatrix} \eta \\ \dot{\eta} \end{Bmatrix} \quad A = \begin{bmatrix} 0 & I \\ -\Lambda & -H \end{bmatrix}$$

Matrices B and C depend on the sensors and actuators to be used. Their structure is explained in section 4.4.

Modal analysis of a structure involves determining the mode shape and frequencies. Finite element modelling with the CAD-CAE program I-DEAS® [35] was used to perform modal analysis. The identified mode shapes and frequencies were then imported to Matlab® [25] to create the state space models used for open and closed loop simulation as well as control design. Two dynamic models were created: a simpler model using rod elements, that only allows for longitudinal deformation of the truss components, and a more complex model using beam elements, which allows for longitudinal deformation as well as bending of the truss components. The rod element model is subsequently used for closed loop simulation and control design purposes, while the beam element model is employed to check the impact of the simplifying assumptions in the modal frequencies and mode shapes for the rod element model, and to verify that at least the first five modes of the structure do not involve local bending of the truss members. To simulate the effect of the mass of the junction blocks, concentrated mass elements where added at the nodes.

4.3.1 Rod Element Model

A rod element has two nodes with one degree of freedom per node that corresponds to the displacement in the axial direction. Figure 4.5 shows a diagram of the rod element. The displacement is varies linearly along the rod element as a function of the distance from node 1, u.

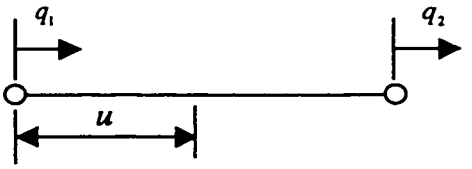

Figure 4.5: Rod Element

The mesh used for the finite element model with rod elements is shown in Figure 4.6. The nodes were placed at the junctions, and are denoted in the figure by star symbols. The cross section of the rod elements is indicated by the ovals at mid-span. Using rod elements is equivalent to assuming that the structure is pin-jointed, and thus the strain profile along each element is constant. For this reason, increasing mesh density, by partitioning the truss members with additional rod elements, will not alter the strain profile. Concentrated mass elements are added at each junction to simulate the effect of the extra weight of the junction blocks, and are denoted in Figure 4.6 by small squares coincident with the nodes. The finite element model has 83 rod elements and 28 nodes. Each node has 3 degrees of freedom; hence the structure has a total of 84 degrees of freedom. The structure is fixed at the base; this restricts 3 degrees of freedom at each of the four base nodes, for a total of 12 constrained degrees of freedom.

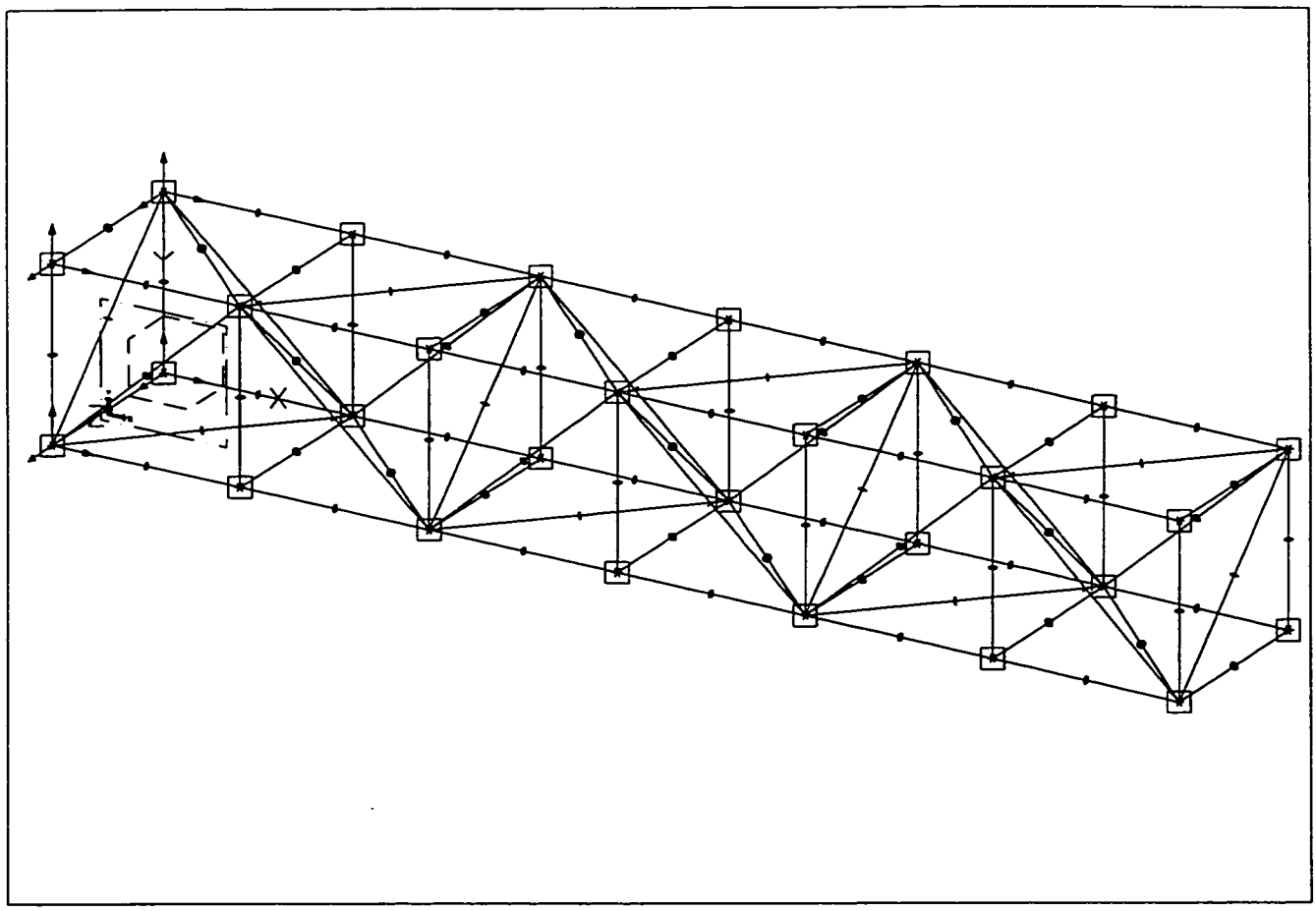

Figure 4.6: Finite Element Mesh for the Rod Element Model

A modal analysis was performed to obtain the frequencies and mode shapes of the system. The results are shown in Figure 4.7 to Figure 4.10 for the first eight modes of the structure.

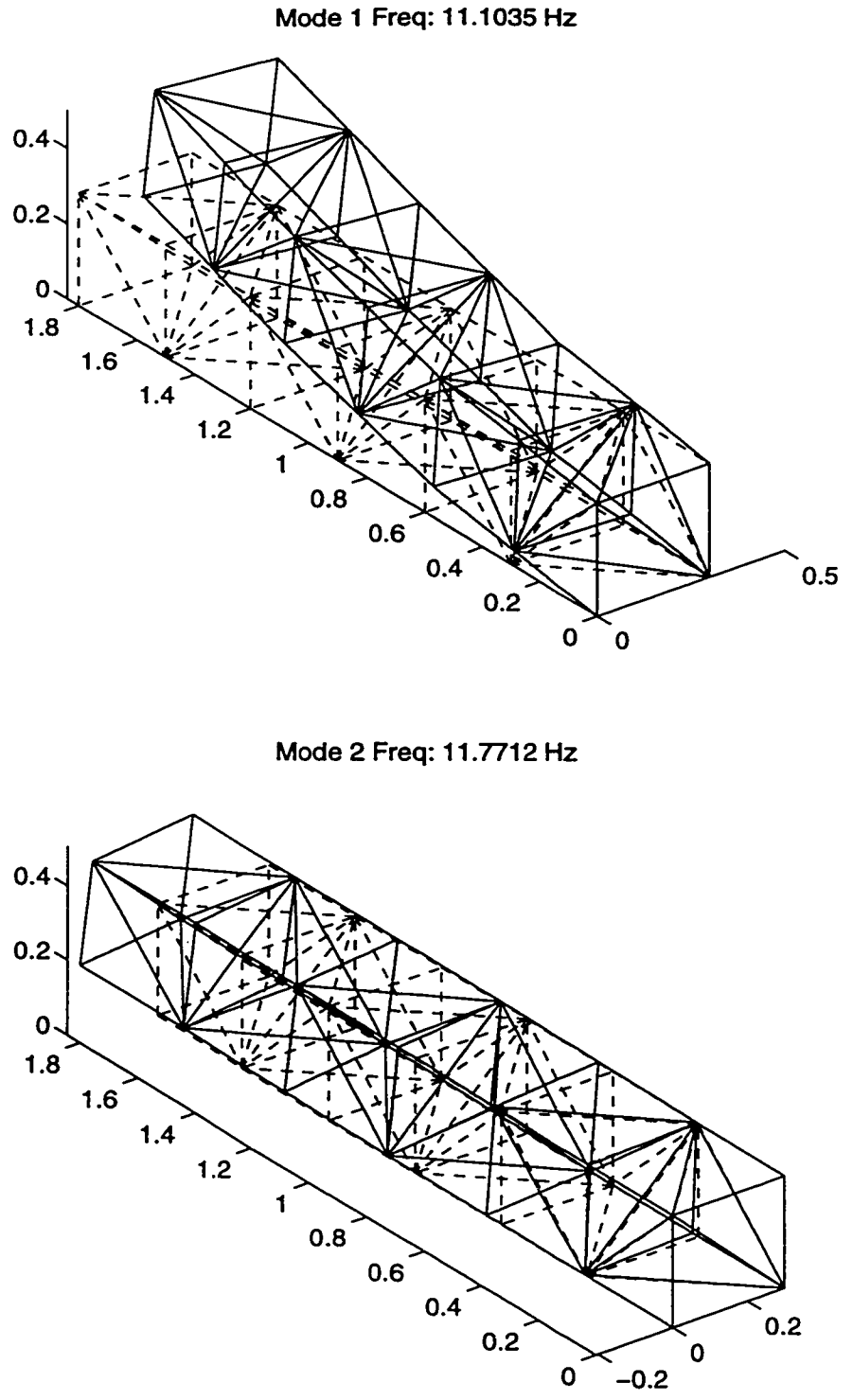

Figure 4.7: Modes 1 and 2. Rod Element Model

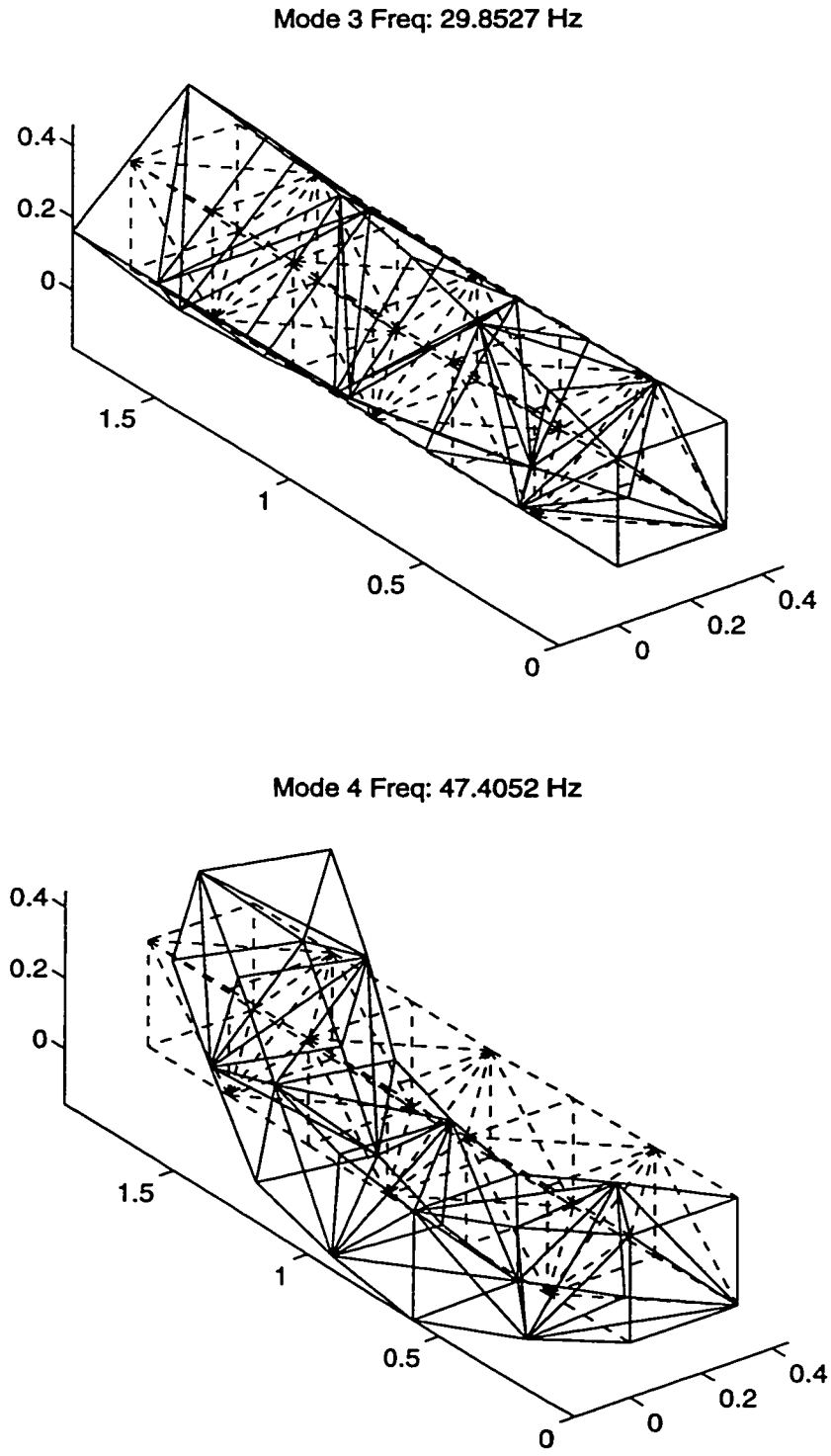

Figure 4.8: Modes 3 and 4. Rod Element Model

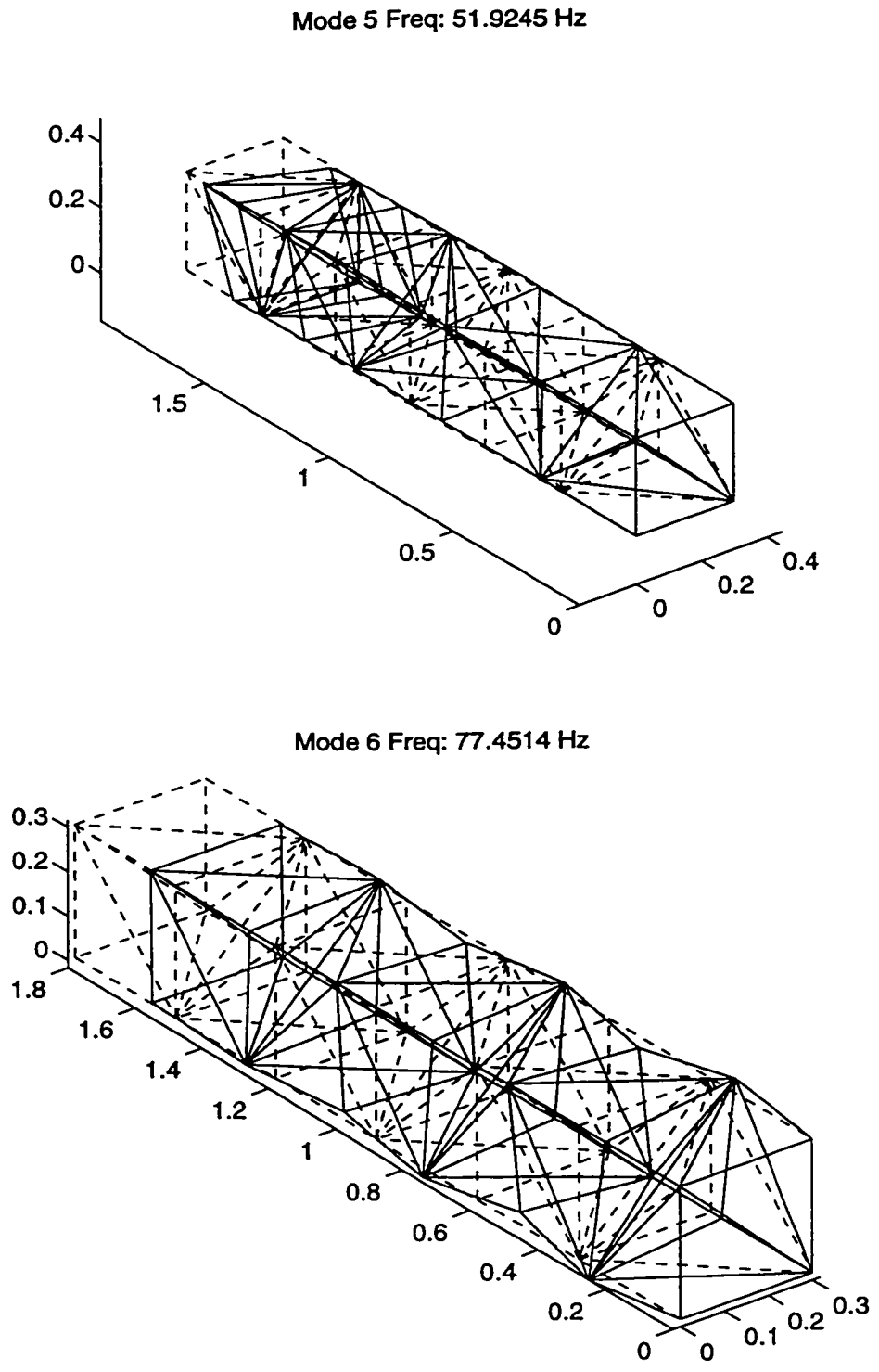

Figure 4.9: Modes 5 and 6. Rod Element Model

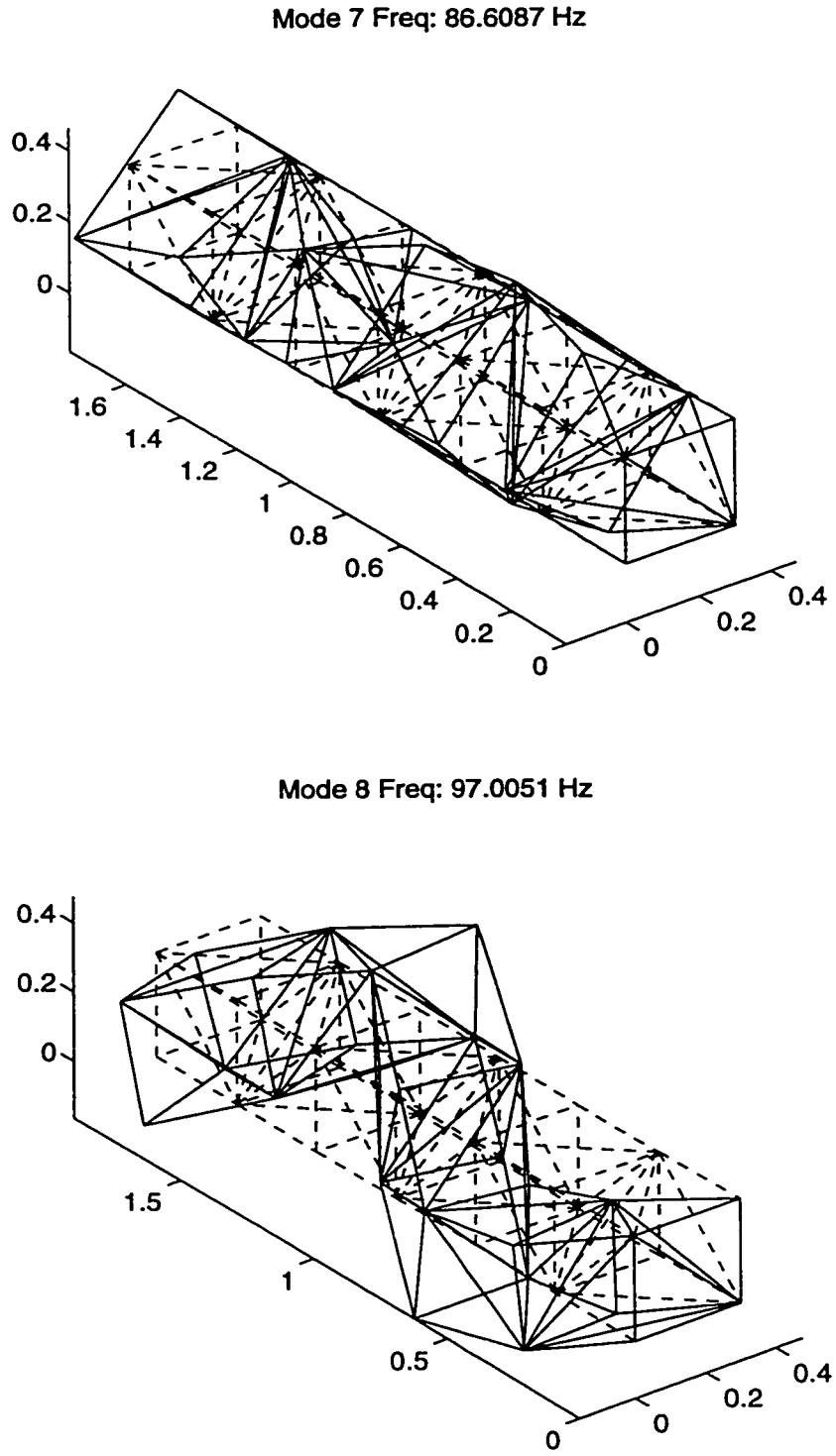

Figure 4.10: Modes 7 and 8. Rod Element Model

4.3.2 Beam Element Model

The objective of the beam element model is to verify that the simplifying assumptions made in the rod element model are valid, and that for the first number of modes of the structure, local bending of the truss member is not present. By performing this analysis, it is possible to size the truss members so that the structure behaves as a truss structure, i.e., the truss members are mostly subject to axial strain and not bending.

The beam element has two nodes per element, with six degrees of freedom per node. Three degrees of freedom ($\theta_u, \theta_v, \theta_w$) account for nodal rotations (bending about u and v-axes and torsion about w-axis) and three degrees of freedom (q_u, q_v, q_w) account for nodal displacements. In this case, the displacement profile along the element is assumed to be cubic polynomial of distance from node 1, u. Figure 4.11 shows the schematic of a beam element, including the degrees of freedom allowed at each node.

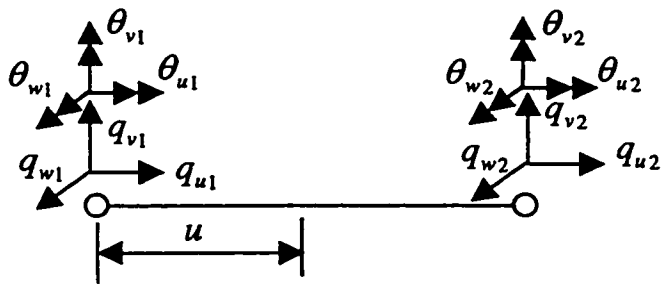

Figure 4.11: Beam Element

The finite element mesh for the beam element model is shown in Figure 4.12. Each truss member is modeled by two rigid elements and two beam elements, as shown in Figure 4.13. The length of the rigid elements is determined by the size of the corresponding connecting blocks, shown in Figure 4.3. It was decided to use two beam

elements to model the flexible portion of each truss member, after testing different mesh densities and finding that convergence was attained with this choice. A beam element has six degrees of freedom at each node. The structure has 166 beam elements, 166 rigid elements, and 277 nodes. Each node has 6 degrees of freedom; hence the structure has a total of 1662 degrees of freedom. The structure is fixed at the base; this restricts 6 degrees of freedom at each of the four base nodes, for a total of 24 constrained degrees of freedom.

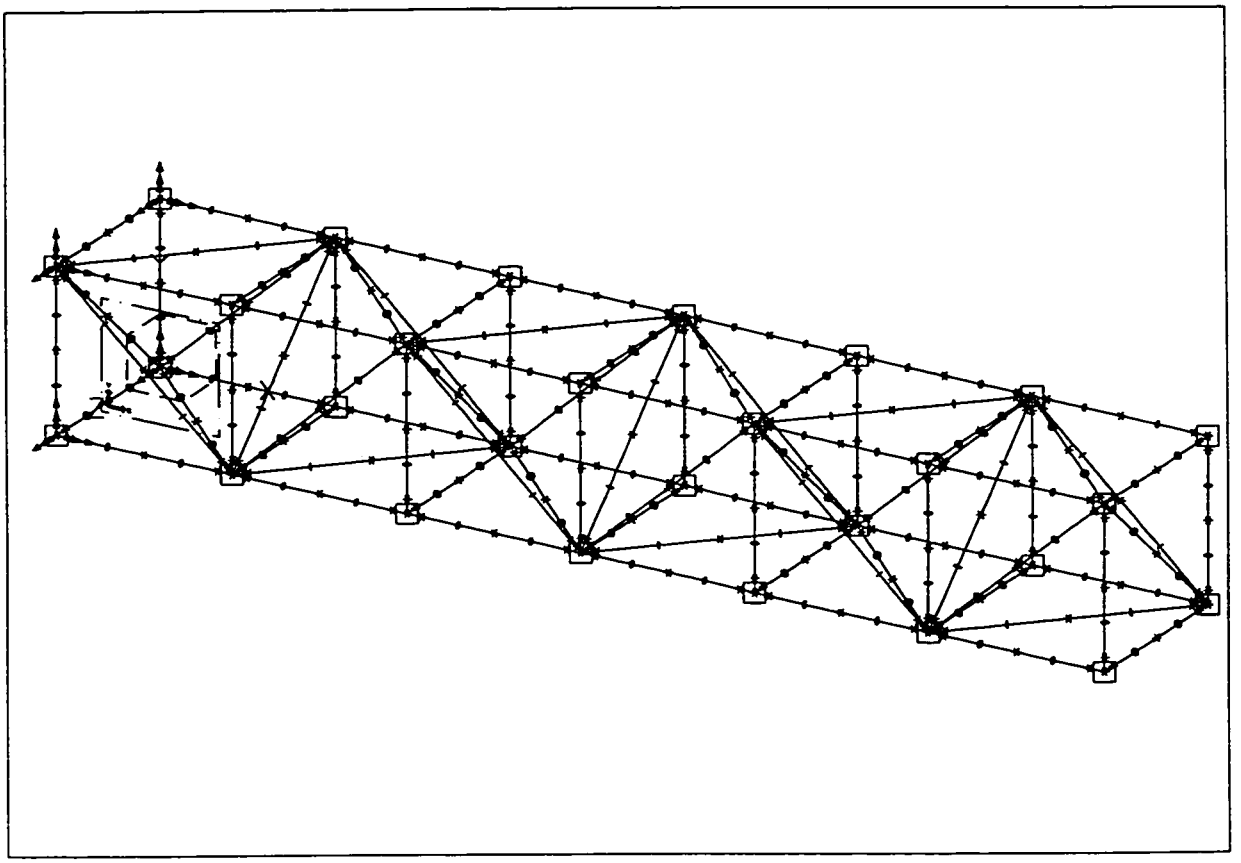

Figure 4.12: Finite Element Mesh for the Beam Element Model

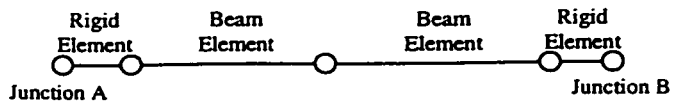

Figure 4.13: Beam Element Model of a Truss Member

By using beam elements instead of rod elements, it is possible to account for the fact that the truss members in the structure are clamped at the joints, instead of pin-jointed. Thus, the truss members are subjected to bending moments and torsion, in addition to axial loads. To model the effect of the rigidity of the connectors at the junctions, rigid finite elements were used at each junction location.

A modal analysis was performed to obtain the frequencies and mode shapes of the system. The results are shown in Figure 4.14 to Figure 4.17 for the first eight modes of the structure.

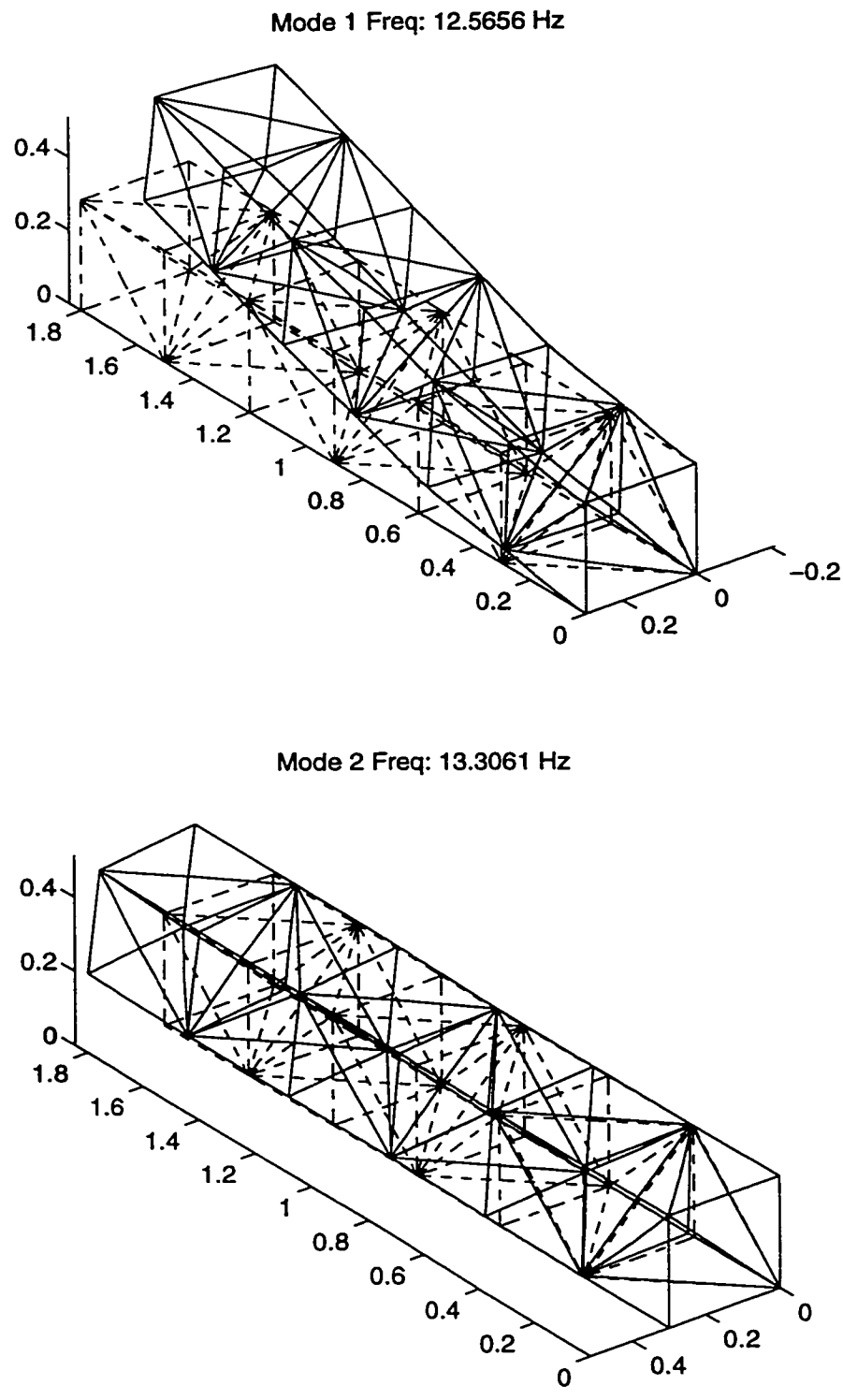

Figure 4.14: Modes 1 and 2. Beam Element Model

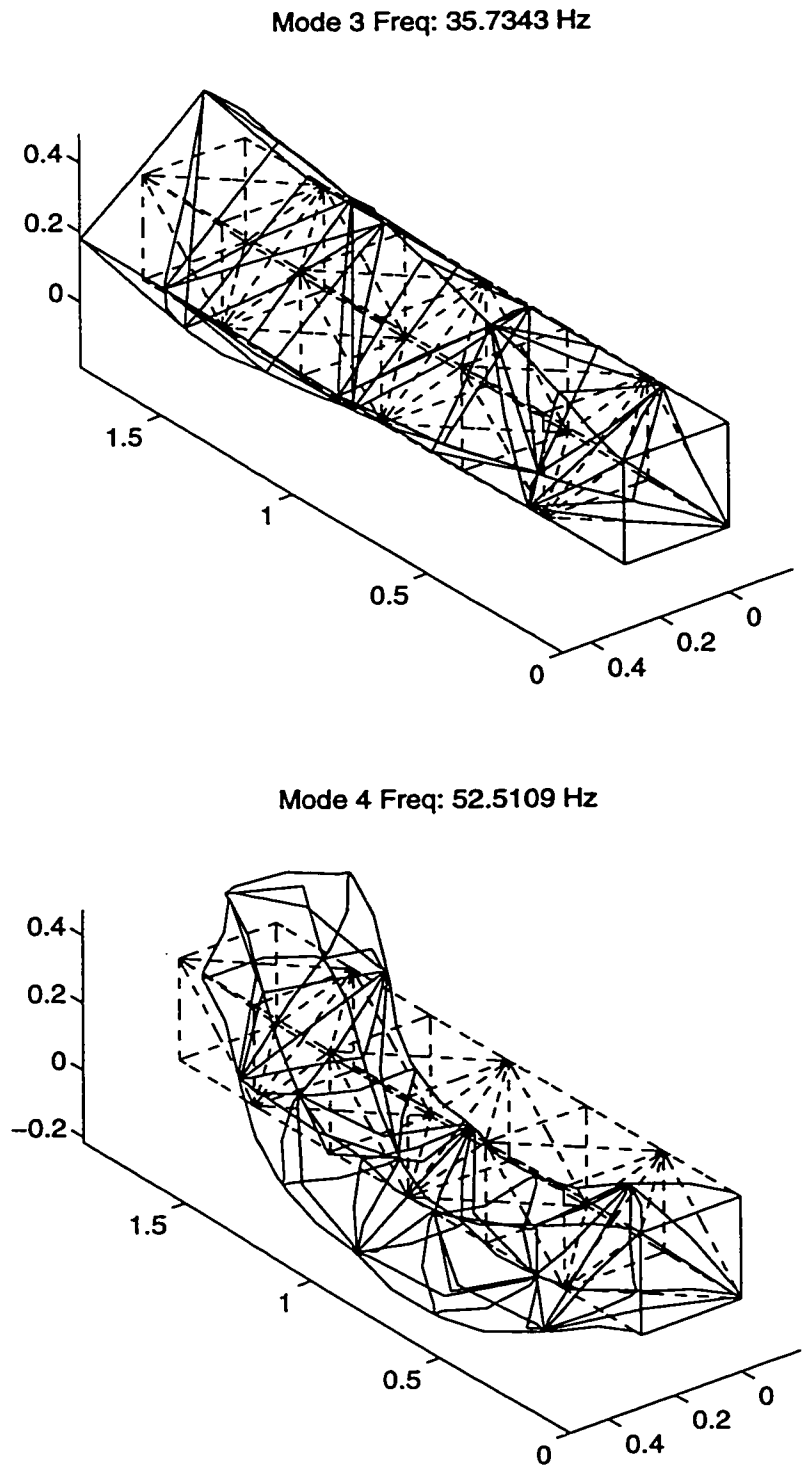

Figure 4.15: Modes 3 and 4. Beam Element Model

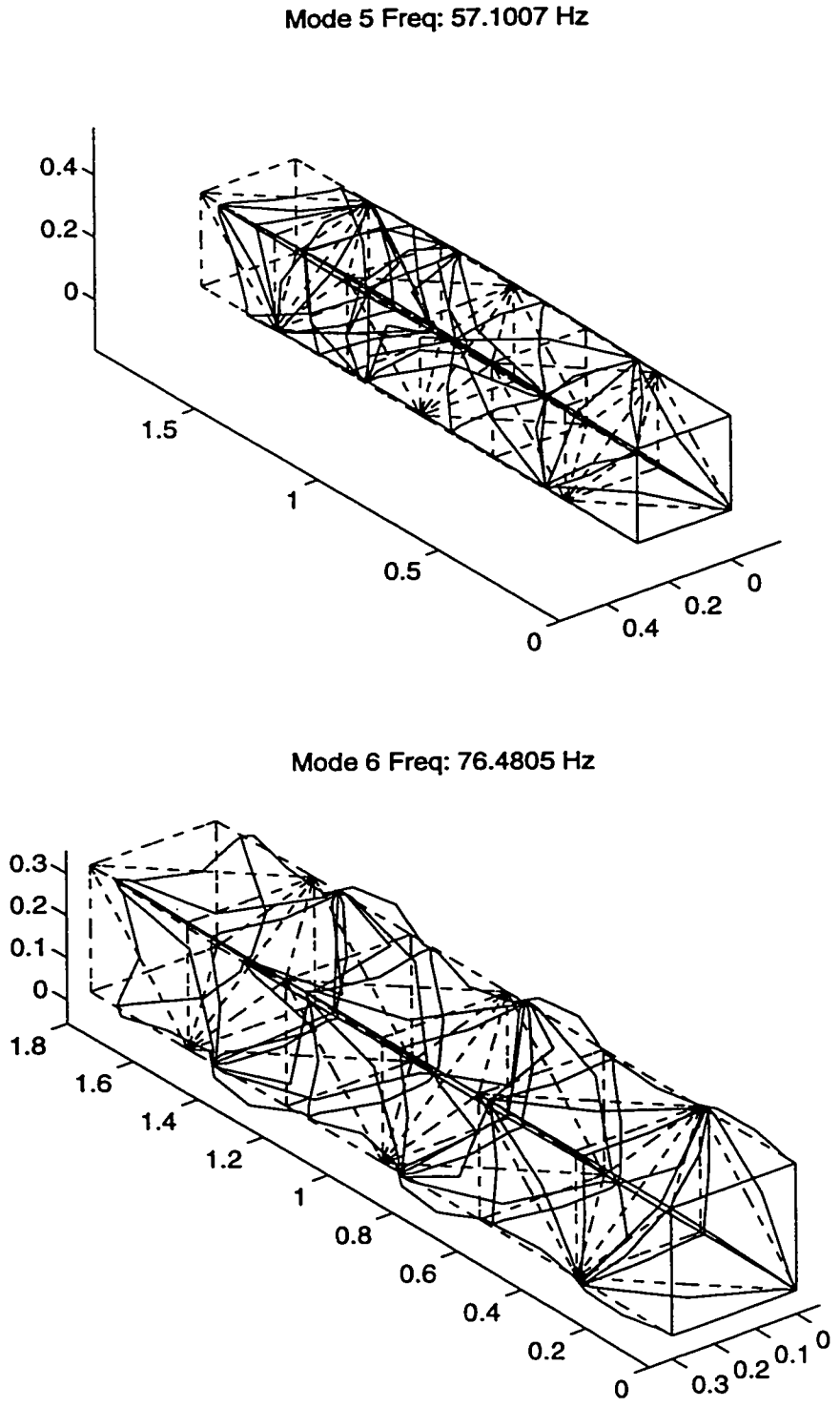

Figure 4.16: Modes 5 and 6. Beam Element Model

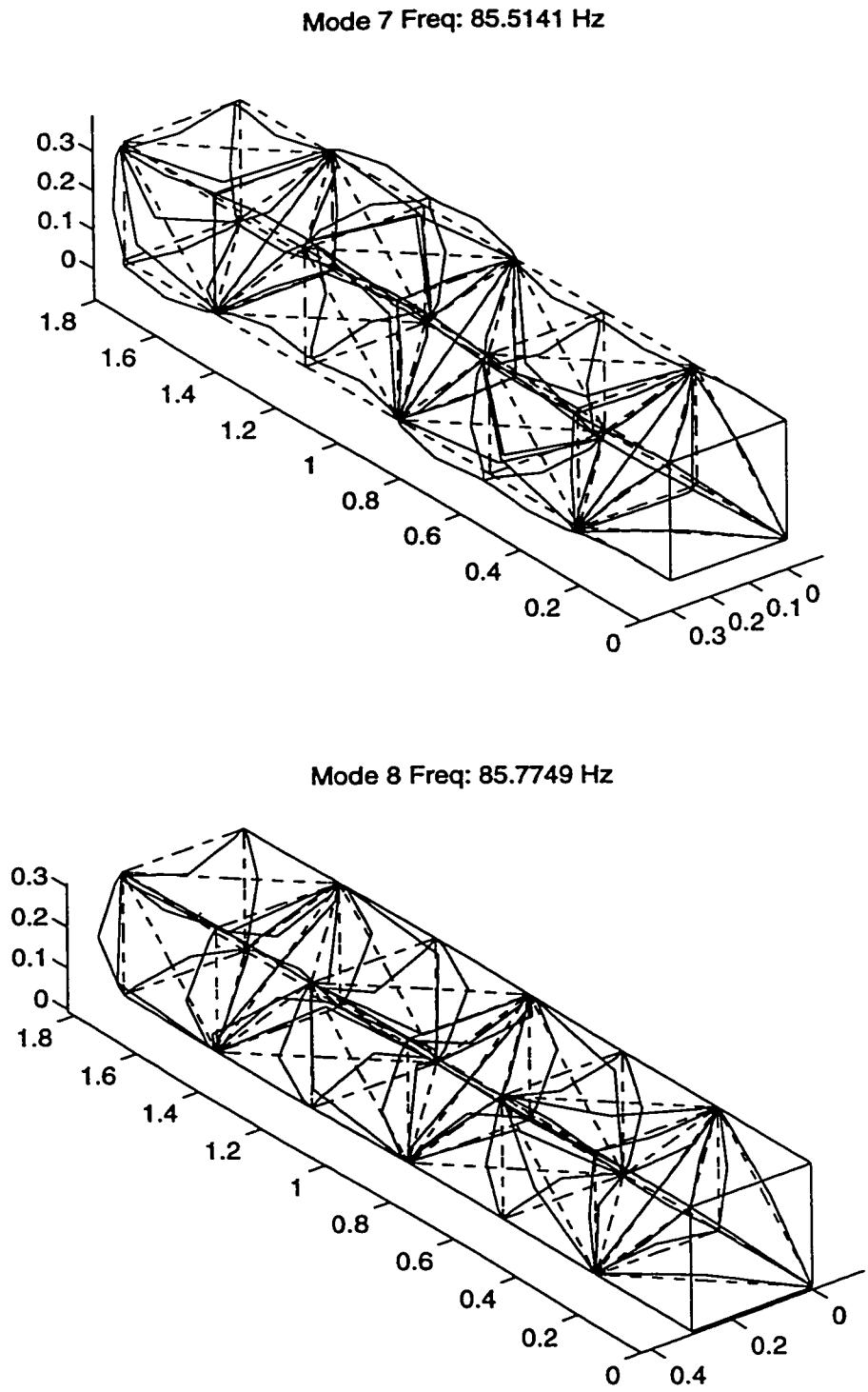

Figure 4.17: Modes 7 and 8. Beam Element Model

4.3.3 Comparison of Rod and Beam Element Models

Comparing the first eight modes (Table 4.2) of the beam element model with those of the rod element model, several observations can be made. The first six mode shapes for both models are similar, but the frequencies in the beam element model are between 10 and 20 percent higher. This is to be expected because the beam element model takes into account the additional stiffness introduced by the connector blocks at the junctions. The seventh and eighth modes of the beam element model do not appear in the rod element model. These modes involve some local bending of the truss members, which cannot be modeled by the rod element model.

Table 4.2: Comparison between Rod Element Model and Beam Element Model

Mode #	Rod Element Model (Hz)	Beam Element Model (Hz)	Difference (%)
1	11.1	12.6	13.5
2	11.8	13.3	12.7
3	29.8	35.7	19.8
4	47.4	52.5	10.8
5	51.9	57.1	10.0
6	77.4	76.5	-1.2
7	86.6	85.5	N/A
8	97.0	85.8	N/A

From this analysis one can conclude that the rod element model is suited for use in the modelling and control design of the truss structure.

4.4. Formulation of the State Space Dynamic Model

The selection of the sensors and actuators, and their influence on the state space model is described in the next subsections.

4.4.1 Observation Matrix for the Piezoelectric Sensor

The open circuit voltage $V_{oc}(t)$ of a piezoelectric film sensor is proportional to the strain of the film. The short circuit current $I_{sc}(t)$ of a piezoelectric film sensor is proportional to the strain rate of the film. Let $V_{oc}^k(t)$ and $I_{sc}^k(t)$ denote the open circuit voltage and short circuit current associated with the piezoelectric film attached to the k^{th} tubular member. Using the derivations in section 2.3.2, the deformation of the piezoelectric film in the axial direction gives the following equations for $V_{oc}^k(t)$ and $I_{sc}^k(t)$.

$$V_{oc}^k(t) = -\frac{d_{31s}^k E_s^k W_s^k}{C_s^k} \int_0^{L_k} \varepsilon^k(x, r_s, t) dx$$

$$I_{sc}^k(t) = -d_{31s}^k E_s^k W_s^k \int_0^{L_k} \frac{\partial \varepsilon^k(x, r_s, t)}{\partial t} dx$$

where d_{31s} is the transverse piezoelectric charge to stress ratio, E_s is the Young's modulus of the film, W_s is the width of the piezoelectric film, C_s is the capacitance of the film and $\varepsilon(x, r_s, t)$ is the strain profile of the piezoelectric film. Note that the subscript $_s$ denotes parameters of the sensor film, while superscript k denotes the element to which the sensor is attached.

Modelling the truss member with rod elements yields a strain profile that is constant along the tubular truss member. Accordingly, the expressions for the open circuit voltage and closed circuit current simplify to:

$$V_{oc}^{k}(t) = \gamma_{V_{oc}}^{k} \varepsilon_{s}^{k} \qquad \gamma_{V_{oc}}^{k} = -\frac{d_{31s}^{k} E_{s}^{k} W_{s}^{k} L_{s}^{k}}{C_{s}^{k}}$$

$$I_{sc}^{k}(t) = \gamma_{I_{sc}}^{k} \dot{\varepsilon}_{s}^{k} \qquad \gamma_{I_{sc}}^{k} = -d_{31s}^{k} E_{s}^{k} W_{s}^{k} L_{s}^{k}$$

From the above equations, it is easy to see that measurements of open circuit voltage and short circuit current can be employed to obtain the strain and strain rate in a truss member. Since a rod element is uniquely associated with each truss member, truss member k can be identified with rod element k. Accordingly, the above expressions are associated with rod element k.

The state space observation C matrix relates the state space variables (modal amplitudes and modal amplitude rates) to the sensor measurements. The structure of the C matrix varies the selection of truss members with bonded sensor films and the dimensions and piezoelectric properties of the films. Assuming that each sensed truss member has an open circuit voltage sensor and a short circuit current sensor, the observation matrix will have the following structure:

$$C = \begin{bmatrix} M_{V_{oc}} \Phi & 0 \\ 0 & M_{I_{sc}} \Phi \end{bmatrix}$$

where Φ is the modal matrix. The matrices $M_{V_{oc}}$ and $M_{I_{sc}}$ both have dimensions *NSENS* $\times$ *NDOF* (*NSENS*: # of sensed elements, *NDOF*: # of degrees of freedom). The matrix $M_{V_{oc}}$ relates nodal displacement vectors to a vector of sensor open circuit voltages. The matrix $M_{I_{sc}}$ relates nodal displacement rate vectors to a vector of sensor short circuit currents.

The notation associated with a sensor on rod element k is shown in Figure 4.18; denote the nodal coordinates by p and nodal displacements by q. In a structure with *NNOD* nodes, the p and q nodal vectors are given by:

$$p = \begin{Bmatrix} p^1 \\ \vdots \\ p^j \\ \vdots \\ p^{NNOD} \end{Bmatrix} \qquad p^j = \begin{Bmatrix} p_1^j \\ p_2^j \\ p_3^j \end{Bmatrix} \qquad q = \begin{Bmatrix} q^1 \\ \vdots \\ q \\ \vdots \\ q^{NNOD} \end{Bmatrix} \qquad q^j = \begin{Bmatrix} q_1^j \\ q_2^j \\ q_3^j \end{Bmatrix}$$

where p^j and q^j (j=1...*NNOD*) are referenced with respect to a global coordinate frame with the coordinates given by the subscripts $_{1,2,3}$. The 123 coordinate frame is an alternate representation of the x-y-z coordinate frame: 1 corresponds to x, 2 to y, and 3 to z.

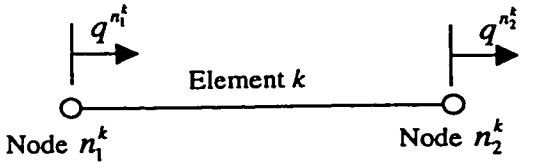

Figure 4.18: Sensor on Rod Element k

The components of the deformation of rod k in the global coordinate frame can be found as

$$\Delta q_i^k = \begin{cases} q_i^{n_2^k} - q_i^{n_1^k} & \text{if } p_i^{n_2^k} > p_i^{n_1^k} \\ q_i^{n_1^k} - q_i^{n_2^k} & \text{if } p_i^{n_1^k} > p_i^{n_2^k} \end{cases} \quad i = 1...3$$

With this definition a positive deformation corresponds to an elongation and a negative deformation corresponds to compression of the rod element.

The total deformation of the rod k can be found using direction cosines:

$$\Delta q^k = \sum_{i=1}^{3} \Delta q_i^k \cos\theta_i^k$$

where $\cos\theta_i^k$ is the direction cosine of element k in direction i, found from the nodal coordinates that correspond to element k. Compute:

$$\Delta p_i^k = \left| p_i^{n_2^k} - p_i^{n_1^k} \right| \quad i = 1...3 \qquad L^k = \left(\sum_{i=1}^{3} \left(\Delta p_i^k \right)^2 \right)^{1/2}$$

The direction cosines for element k are computed as

$$\cos\theta_i^k = \frac{\Delta p_i^k}{L^k} \quad i = 1...3$$

The unit deformation of element k, denoted by ε^k, is given by

$$\varepsilon^k = \frac{\Delta q^k}{L^k} = \frac{1}{L^k} \begin{bmatrix} \cos\theta_x^k & \cos\theta_y^k & \cos\theta_z^k \end{bmatrix} \begin{Bmatrix} \Delta q_1^k \\ \Delta q_2^k \\ \Delta q_3^k \end{Bmatrix}.$$

The open circuit voltage V_{oc}^k on element k is

$$V_{oc}^k = \gamma_{V_{oc}}^k \varepsilon^k = \gamma_{V_{oc}}^k \frac{\Delta q^k}{L^k} = \frac{\gamma_{V_{oc}}^k}{L^k} \begin{bmatrix} \cos\theta_1^k & \cos\theta_2^k & \cos\theta_3^k \end{bmatrix} \begin{Bmatrix} \Delta q_1^k \\ \Delta q_2^k \\ \Delta q_3^k \end{Bmatrix}$$

The short circuit current I_{sc}^k on element k is

$$I_{sc}^k = \gamma_{I_{sc}}^k \dot{\varepsilon}^k = \gamma_{I_{sc}}^k \frac{\Delta \dot{q}^k}{L^k} = \frac{\gamma_{I_{sc}}^k}{L^k} \begin{bmatrix} \cos\theta_1^k & \cos\theta_2^k & \cos\theta_3^k \end{bmatrix} \begin{Bmatrix} \Delta \dot{q}_1^k \\ \Delta \dot{q}_2^k \\ \Delta \dot{q}_3^k \end{Bmatrix}$$

Let the rod elements with sensors be indexed by k^r, $r = 1, 2, ...NSENS$. The element (r,t) of matrix $M_{V_{oc}}$ is given by

$$M_{V_{oc}}(r,t) = \frac{\gamma_{V_{oc}}^k}{L^k} \times \begin{cases} \cos\theta_i^{k^r} \operatorname{sgn}(p_i^{n_1^{k^r}} - p_i^{n_2^{k^r}}), \text{if some } i \in (1...3) \text{ satisfies } t = 3(n_1^{k^r} - 1) + i \\ \cos\theta_i^{k^r} \operatorname{sgn}(p_i^{n_2^{k^r}} - p_i^{n_1^{k^r}}), \text{if some } i \in (1...3) \text{ satisfies } t = 3(n_2^{k^r} - 1) + i \\ 0, \qquad \text{otherwise} \end{cases}$$

The matrix $M_{I_{sc}}$ is found in the same fashion, but using displacement rates instead of displacements, and using the adequate piezoelectric gains. The element (r,t) of matrix $M_{I_{sc}}$ is given by

$$M_{I_{sc}}(r,t) = \frac{\gamma_{I_{sc}}^k}{L^k} \times \begin{cases} \cos\theta_i^{k^r} \operatorname{sgn}(p_i^{n_1^{k^r}} - p_i^{n_2^{k^r}}), \text{ if some } i \in (1...3) \text{ satifies } t = 3(n_1^{k^r} - 1) + i \\ \cos\theta_i^{k^r} \operatorname{sgn}(p_i^{n_2^{k^r}} - p_i^{n_1^{k^r}}), \text{ if some } i \in (1...3) \text{ satifies } t = 3(n_2^{k^r} - 1) + i \\ 0, \qquad \text{otherwise} \end{cases}$$

4.4.2 Control Matrix for the Piezoelectric Actuator

Since a rod element model is being used on this part of the analysis, a unique rod element is associated with each truss member. Furthermore, the rod element only undergoes axial deformations. When perfect bonding is assumed between a piezoelectric film and the truss member to which it is attached, the force transmitted by the piezoelectric to the structure is concentrated at the ends of the piezoelectric film actuator (Vaz [41]). The forces at the ends of the piezoelectric film are transferred to the nodes that form the active element. The strain at each end of the piezoelectric attached to truss member k can be found as:

$$\varepsilon_a^k = \varepsilon_T^k = \frac{\psi^k}{\psi^k + 2}\varepsilon_T^k + \frac{2}{\psi^k + 2}\Lambda^k$$

where ε_a^k and ε_T^k denote the piezoelectric and truss strain at member k respectively, Λ^k is the effective strain of the piezoelectric film, which depends on the voltage applied to the element k, V^k, as described by the following expression:

$$\Lambda^k = \frac{d_{31a}^k V^k}{t_a^k}$$

and ψ^k is the truss member to piezoelectric stiffness ratio:

$$\psi^k = \frac{E_T^k t_T^k}{E_a^k t_a^k}$$

The force transmitted from the piezoelectric actuator to the structure at the ends of the actuator, f^k, can be written as:

$$f^k = \sigma_a^k A_{cs}^k = E_a^k A_{cs}^k (\varepsilon_a^k - \Lambda^k) = \frac{E_T^k A_{cs}^k}{\psi^k + 2}\varepsilon_T^k - \frac{E_T^k A_{cs}^k d_{31}^k}{(\psi^k + 2)t_a^k} V^k$$

where A_{cs}^k is the cross sectional area of truss member k. The transmitted forced can be rearranged as follows:

$$f^k = f_A^k + f_B^k$$

where

$$f_A^k = \lambda_A^k \varepsilon_T^k, \qquad f_B^k = \lambda_B^k V^k$$

$$\lambda_A^k = \frac{E_T^k A_{cs}^k}{\psi^k + 2}, \qquad \lambda_B^k = -\frac{E_T^k A_{cs}^k d_{31}^k}{(\psi^k + 2) t_a^k}$$

The force provided by the piezoelectric actuator varies with both the control voltage applied and the deformation of the structure. The active piezoelectric film contributes to the state space model of the structure through both the A-matrix (f_A^k term) and the B-matrix (f_B^k term). In order to find the contribution of the active elements to the A-matrix, it is necessary to find the vector of forces that acts on the nodes, caused by the active elements. To achieve this, the part the vector of forces of an active element that contribute to the A-matrix should be expressed in terms of the modal amplitudes η that constitute the state space, as follows:

$$f_A^k = N^k q = N^k \Phi \eta$$

where the matrix N^k of size $NDOF \times NDOF$ relates the nodal displacements q to the nodal forces produced by active element k. The matrix N^k can be decomposed as:

$$N^k = N_1^k N_2^k$$

where the matrix N_2^k of size *NACT*× *NDOF* (*NACT*: # of active elements) extracts the truss member strain ε_T^k from the nodal degrees of freedom, while the matrix N_1^k of size *NDOF*×*NACT* obtains the nodal forces in each direction from the truss member strain ε_T^k. The structure of the matrices N_1^k and N_2^k is obtained in a similar way as the one used to find the sensor signals in section 4.4.1 and is given next. Let the rod elements with actuators be indexed by k^r, $r = 1, 2, ...NACT$. Then

$$N_2^k(r,t) = \frac{1}{L^k} \times \begin{cases} \cos\theta_i^{k^r} \operatorname{sgn}(p_i^{n_1^{k^r}} - p_i^{n_2^{k^r}}), \text{if some } i \in (1...3) \text{ satisfies } t = 3(n_1^{k^r} - 1) + i \\ \cos\theta_i^{k^r} \operatorname{sgn}(p_i^{n_2^{k^r}} - p_i^{n_1^{k^r}}), \text{if some } i \in (1...3) \text{ satisfies } t = 3(n_2^{k^r} - 1) + i \\ 0, \qquad \text{otherwise} \end{cases}$$

$$N_1^k(t,r) = \lambda_A^k \begin{cases} \cos\theta_i^{k^r} \operatorname{sgn}(p_i^{n_1^{k^r}} - p_i^{n_2^{k^r}}), \text{if some } i \in (1...3) \text{ satisfies } t = 3(n_1^{k^r} - 1) + i \\ \cos\theta_i^{k^r} \operatorname{sgn}(p_i^{n_2^{k^r}} - p_i^{n_1^{k^r}}), \text{if some } i \in (1...3) \text{ satisfies } t = 3(n_2^{k^r} - 1) + i \\ 0, \qquad \text{otherwise} \end{cases}$$

The matrix A^k corresponds to the element k in the structure with a piezoelectric actuator. The matrix Γ^k relates the modal amplitudes η to the modal forces associated with active element k. Matrix Γ^k can be computed as follows

$$\Gamma^k = \Phi^T N^k \Phi .$$

The state space A-matrix is given by

$$A = A^0 + \sum_{r=1}^{NACT} A^{k^r}$$

where

$$A^0 = \begin{bmatrix} 0 & I \\ -\Lambda & -H \end{bmatrix} \qquad A^k = \begin{bmatrix} 0 & 0 \\ \Gamma^k & 0 \end{bmatrix}$$

The state space B-matrix caused by the active elements can be found from the force vector f_B^k in a manner analogous to the previous analysis. Given an applied voltage, the resulting piezoelectric force has to be included in the state space model, using an insertion matrix Δ and the modal matrix Φ, as follows

$$B = \begin{bmatrix} 0 \\ \Phi^T \end{bmatrix} \Delta$$

The insertion matrix $\Delta_{NDOF \times NACT}$ is determined as follows. The (t,r) element of matrix Δ is given by

$$\Delta(t,r) = \frac{\lambda_B^k}{L^k} \times \begin{cases} \cos\theta_i^{k'} \operatorname{sgn}(p_i^{n_1^{k'}} - p_i^{n_2^{k'}}), & \text{if some } i \in (1...3) \text{ satisfies } t = 3(n_1^{k'} - 1) + i \\ \cos\theta_i^{k'} \operatorname{sgn}(p_i^{n_2^{k'}} - p_i^{n_1^{k'}}), & \text{if some } i \in (1...3) \text{ satisfies } t = 3(n_2^{k'} - 1) + i \\ 0, & \text{otherwise} \end{cases}$$

4.5. Summary

The procedure for the calculation of the state space representation of a truss structure, including the effect of piezoelectric actuators and sensors was presented. A design for a truss structure that represents a typical LFSS was shown, and its mathematical model was obtained using finite element analysis and modal decomposition. The influence of the piezoelectric actuators and sensors on the space state model of the truss structure was found, in the finite element-modal analysis framework. Using the state space representation of the truss structure, it is possible to design control strategies that will be used to perform active vibration control on the truss structure taking advantage of smart truss members, as it will be shown in chapters 5 and 6.

5. Control Design and Closed Loop Behaviour

5.1. Introduction

In this section, collocated velocity feedback, optimal LQG control and robust H_∞ control are reviewed and applied to the truss structure described in section 4.2. For control design and closed loop simulation purposes the rod element model developed in section 4.3.1 was used. This dynamic model is more suited for control design because of the selection of sensors and actuators: the piezoelectric sensor and actuator elements can only properly observe and control vibrational modes that involve axial displacement of the truss components, and are unable to observe or act on bending. In addition, the truss structure is designed in such a way that the main modes of vibration involve mostly axial strain of the truss components.

For the design and simulation of the control techniques presented in this chapter, two dynamic models are obtained. A 30^{th} order test model is developed for simulation purposes; this model includes estimated modal damping coefficients obtained from the experimental structure. A 5^{th} order model is obtained for control design purposes. No damping is included in this model, since it is assumed that the designer does not have access to that information until the structure is orbited.

In section 5.2, some details on the design of the sensors and actuators are presented. In section 5.3 the synthesis and design of the Negative Velocity Feedback controller, as well as simulation results of the closed loop behaviour, is shown. The synthesis, design and simulations of a dynamic LQG controller are shown in section 5.4. The robust dynamic H_∞ controller synthesis, design and simulations are presented in section 5.5.

5.2. Actuator and Sensor Design

Table 5.1 shows some of the relevant mechanical and piezoelectric properties of the piezoelectric materials used in this research. For sensing purposes, polyvinyldene fluoride (PVDF) piezoelectric film was selected. This material was chosen because of its convenient piezoelectric properties: it produces relatively large voltages for a given strain (high g_{31} coefficient). For actuator purposes, a piezoceramic material such as lead zirconate titanate (PZT) is more suited to the task, because of its higher strain for a given electric field (high d_{31} coefficient).

Table 5.1: Properties of Piezoelectric Materials

Material	Application	d_{31} (C/N)	g_{31} (V m/N)	Young's Modulus E (N/m^2)	Permitivitty $\in$ (F/m)
PVDF	Sensor	23×10^{-12}	216×10^{-3}	2×10^{9}	106×10^{-12}
BM527 (PZT)	Actuator	215×10^{-12}	7×10^{-3}	6.9×10^{10}	3.54×10^{-8}

The actuators are cylindrical shells of ceramic PZT material, split longitudinally to facilitate the installation in the active truss members. The sensors are rectangular pieces of PVDF. The dimensions of the sensors and actuators are given in Table 5.2. The length is measured along the axis of the truss member; the width refers to the

dimension along the circumference of the member, and the thickness is measured across the radius, as shown on Figure 5.1.

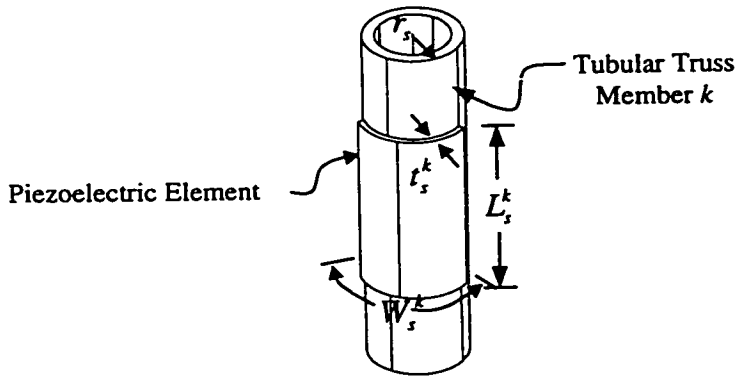

Figure 5.1: Piezoelectric Film Attached to Tubular Truss Member

Table 5.2: Dimensions of Sensors and Actuators

Application	Material	Length (mm)	Width (mm)	Thickness (mm)
Sensor	PVDF	42	17.0	28×10^{-3}
Actuator	BM527 (PZT)	25.4	39.9	1.0

5.3. Negative Velocity Feedback Controller Design

As a first approach for the active control of vibrations in the structure, a collocated negative velocity feedback controller was designed. This technique is intuitively appealing for several reasons:

a) It is inherently stable, due to the passivity properties of the approach, which mimics viscous damping at the locations of the sensor-actuator pairs.

b) It is robust with respect to parametric uncertainties and disturbances. In fact, a velocity feedback control is independent of the system dynamic model.

c) It has the implementation advantages of a decentralized control system, in the sense that each sensor feeds its signal only to the local actuator.

d) It is simple to implement.

Intuitively, one can see the collocated negative velocity feedback as a way of artificially introducing viscous damping into the system. A Lyapunov stability analysis can be used to show the stable nature of this control law (Balas [4]). Given the following system model, obtained using finite element analysis as shown in chapter 4:

$$M\ddot{q} + Kq = F$$

The assumed Lyapunov function is chosen as the sum of kinetic and potential energy of the structure:

$$E(t) = \tfrac{1}{2}(\dot{q}^T M\dot{q} + q^T Kq)$$

According to Lyapunov's second method, in order for the system to be stable,

$$E(t) > 0 \quad \text{for all } q \neq 0$$

and

$$\dot{E}(t) \leq 0$$

Calculating $\dot{E}(t)$, one obtains:

$$\dot{E}(t) = \dot{q}^T M\ddot{q} + \dot{q}^T Kq = \dot{q}^T (M\ddot{q} + Kq) = \dot{q}^T F$$

The control input F is chosen to be:

$$F = -K\dot{q}$$

where K is a positive definite matrix. This control input guarantees that

$$\dot{E}(t) = -\dot{q}^T K\dot{q} < 0 \text{ for all } \dot{q} \neq 0$$

which is the necessary and sufficient condition for the system to be globally stable.

There are two possible ways of obtaining a strain rate measurement using piezoelectric sensors. In the collocated negative velocity feedback control system, the strain rate is obtained at a given element of the structure. This signal is amplified, inverted and fed to a piezoceramic actuator placed at or near the same location as the sensor. Sensor-actuator pairs can be placed at any location in the structure, and as long as the sensors and actuators can achieve observability and controllability over all the modes of the system, then the damping factor for each mode will be increased. There are two possible ways of obtaining a strain rate signal from the piezoelectric sensors: by measuring the short circuit current, which as it was shown in section 4.4.1 is directly proportional to the strain rate, or by obtaining the open circuit voltage, which was shown in section 4.4.1 to be proportional to the strain, and differentiation with low-pass filtering to obtain a signal that is proportional to the strain rate. Although in theory both measurements should yield the same results, there are practical considerations. Both techniques were tested experimentally, and it was shown that measuring the open circuit

voltage and differentiation with low-pass filtering yielded a better strain rate signal, with less noise contamination that the one obtained from measuring the short circuit current. The reason for this may be the fact that the short circuit currents obtained in the sensor due to straining are very small, in the order of 10^{-7} amperes. Since there are high voltage amplifiers and cables in the vicinity, it is assumed that the small signal coupled with the electromagnetic fields created by the high voltage sources tend to contaminate the short circuit current measurement, which then needs to be greatly amplified in order to be usable, thus also amplifying the noise.

The state space observation matrix for the case of exclusive use of open circuit voltage measurement is given by

$$C = \lfloor M_{V_{oc}} \Phi \quad 0 \rfloor$$

A first order high pass filter is used to perform the differentiation. This provides for a much cleaner differentiation of the signal when compared to direct differentiation, which is known to have noise amplification qualities associated with it. The cutoff frequency was placed at 80 Hz. The transfer function of the resulting filter is given by:

$$\frac{Y(s)}{V_{oc}(s)} = \frac{s}{s + 2\pi 80}$$

The negative velocity feedback control law is

$$u = -K_v y$$

where K_v is the diagonal feedback matrix of gains and y contains the differentiated open circuit voltage signals. Theoretically, as the values of the gains in the matrix K_v increase, so do the modal damping coefficients for the system, but the required control effort also increases proportionally. In practice there are other limits to the feedback

gain, such as actuator saturation, unmodelled higher order dynamics, and noise, that can make the system unstable for high values of K_v.

In the simulations, an impact test was performed. Figure 5.2 shows the location of the impact. Sensor-actuator pairs were placed on the four truss members indicated with thick lines. This selection is made due to the high axial strains that these truss members undergo compared to other members in the first 5 vibrational modes. All the considered modes are controllable and observable with this sensor and actuator configuration.

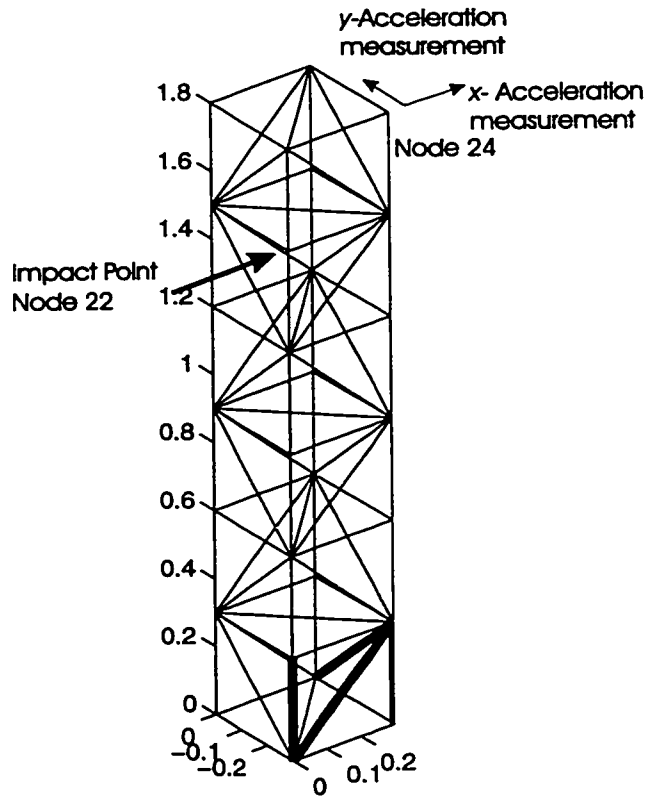

Figure 5.2: Impact Test: Location of Disturbance and Active Truss Members

The first 30 modes of vibration were included and the available actuation voltage was capped at ±265 volts, to match the power available in the experimental testbed.

Figure 5.3 shows the location of the poles for two different sets of values of the feedback gains in K_v. The two sets of poles correspond to the following gain matrices:

$$\text{High Feedback Gain: } K_v = 20\, I_4$$

$$\text{Low Feedback Gain: } K_v = 10\, I_4$$

where I_4 is a 4x4 identity matrix. It can be noticed that the effect of this controller is to move the poles to the left, without greatly affecting the imaginary part of the poles, as expected.

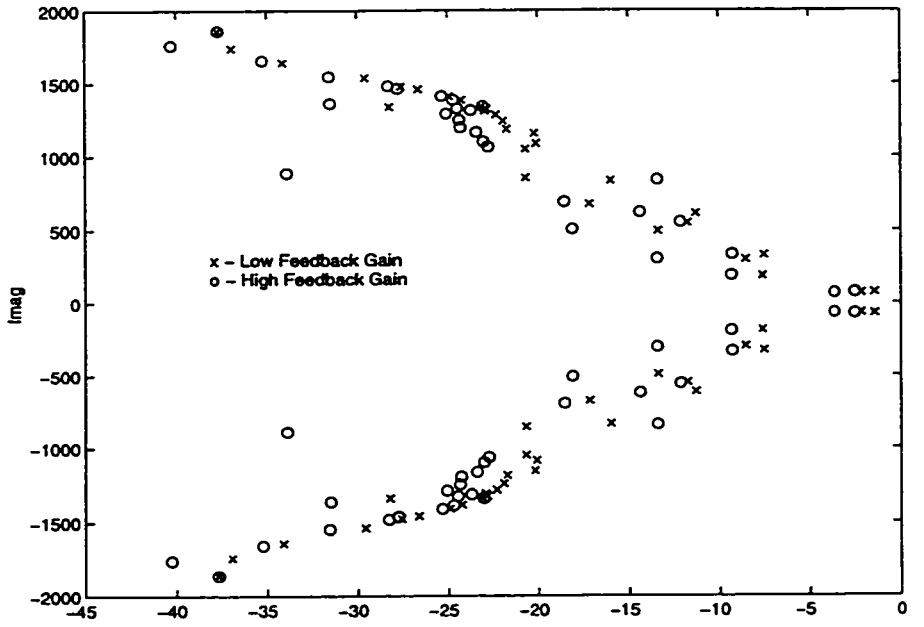

Figure 5.3: Closed Loop Poles, Velocity Feedback Control

Figure 5.4 shows the Maximum Singular Value plot for the open loop system and the closed loop system using the low feedback gain. The attenuation of the resonant peaks

can be easily appreciated on all frequencies, but more markedly in the higher frequencies, as pointed before.

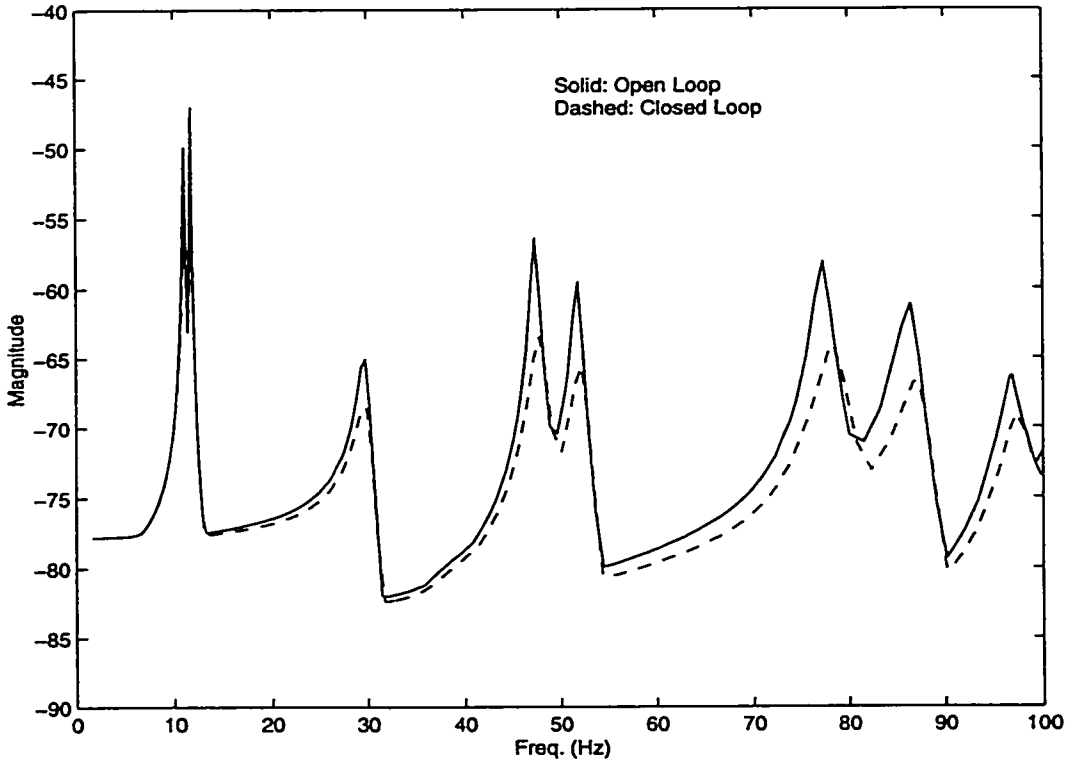

Figure 5.4: Maximum Singular Value Plot. Velocity Feedback Control

The Simulink block diagram of the closed loop system is shown in Figure 5.5. This model is used for the simulation of the time history of the response to the impact test. The matrices used in the simulation are obtained using a separate Matlab script.

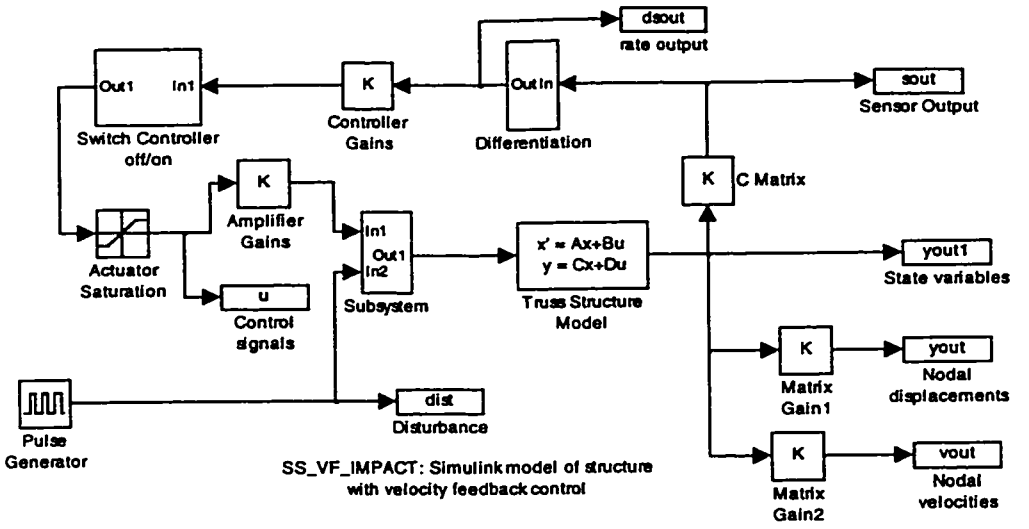

Figure 5.5: Simulink Model of the Negative Velocity Feedback System

Figure 5.6 shows the time history of the response of the structure to the impact, and Figure 5.7 shows the control signals to the actuators, for the low feedback gain controller. The displacement shown corresponds to node 24, located at one of the top corners of the structure.

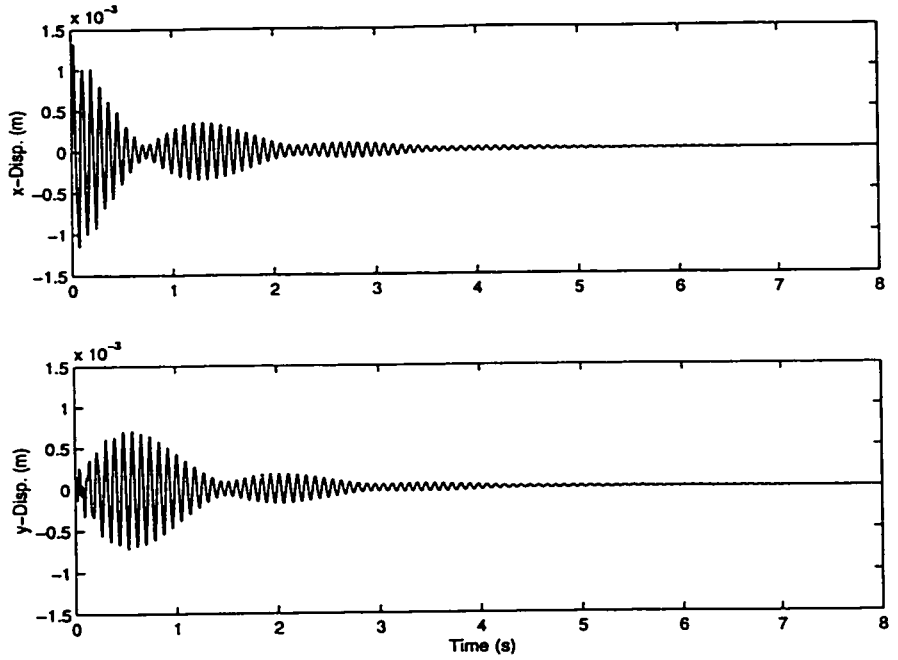

Figure 5.6: Displacement of Node 24. Velocity Feedback Control (Simulation)

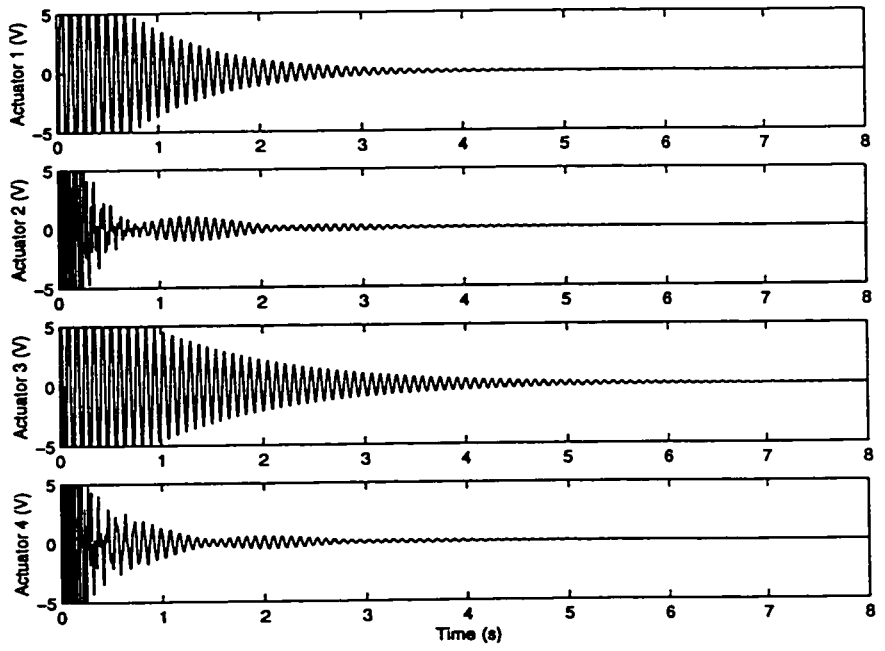

Figure 5.7: Control Signal. Velocity Feedback Control (Simulation)

5.4. LQG Controller Design

LQG state space control is well suited for control design in multiple input-multiple output (MIMO) systems in which a systematic trade-off between performance and control input is required. The LQG design problem consists of finding the following dynamic compensator (Allen *et al.* [2])

$$\dot{x}_c = A_c x_c + Fz$$
$$u = Kx_c$$

which stabilizes the system model

$$\dot{x} = Ax + B_u u + B_w w$$
$$z = Mx + v$$
$$y = Cx$$

while minimizing the following quadratic performance index:

$$J = E[\, y^T R_1 y + u^T R_2 u \,]$$

where w and v are white noise disturbances and sensor noise signals, respectively, with zero mean and constant variance:

$$E(w) = 0 \quad E(w^T w) = W$$

$$E(v) = 0 \quad E(v^T v) = V$$

($E(\cdot)$ is the expectation operator), and R_1 and R_2 are constant, positive definite matrices penalizing the output and the control signal, respectively. When the order of the compensator is restricted to be as that of the dynamic model, the solution to the LQG problem is the Kalman filter estimator coupled to the LQR regulator such that:

$$A_c = A - Q\overline{\Sigma} - \Sigma P$$
$$F = QM^T V^{-1}$$
$$K = -R_2 B_u^T P$$

where F is the Kalman filter optimal state estimator gain and K is the optimal LQR state feedback gain, and

$$\overline{\Sigma} = M^T V^{-1} M$$
$$\Sigma = B_u R_2^{-1} B_u^T$$

The matrices Q and P are the solutions to the following uncoupled Riccati matrix equations:

$$AQ + QA^T + B_w W B_w^T - Q\overline{\Sigma}Q = 0$$

$$A^T P + PA + C^T R_1 C - P\Sigma P = 0$$

For the simulation the same set of sensors and actuators used in the velocity feedback controller simulation were used, to provide a standard for comparison between the different control laws. In order to examine the effect of sensor and control spillover, the controller design was performed using a 5^{th}-order model, while the simulations were executed with a 30^{th} order model.

Details of the design of the LQG controller, together with the controller state space matrices are given in Appendix A. For this controller design, the maximum singular value plot is shown in Figure 5.8:

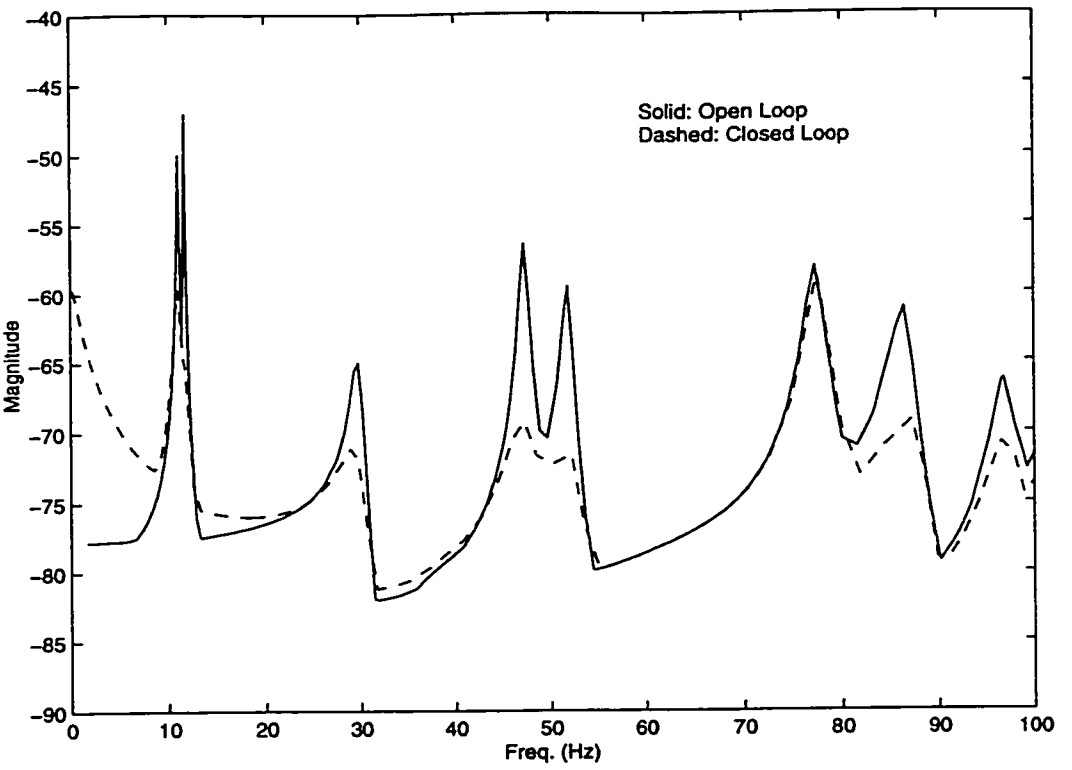

Figure 5.8: Maximum Singular Value Plot. LQG Control

The solid line corresponds to the open loop system, and the dashed line to the closed loop system. The attenuation of the resonant peaks can be noticed, particularly for the first 5 modes of the system, which were included in the control design. A marked increase in the frequency response near zero frequency can also be seen, which reflects the fact that this controller is not very robust with respect to the spillover problem. In fact, other controller designs with lower control penalties became unstable when coupled with higher order models of the system. This is a known problem for the LQG control design methodology, noted by Doyle [16].

Figure 5.9 shows the Simulink model of the closed loop truss with a dynamic controller. Both LQG and H_∞ techniques produce dynamic controllers.

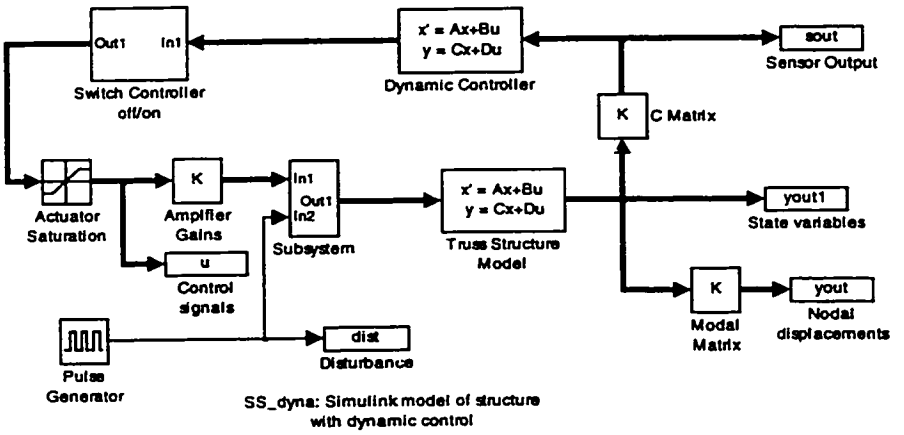

Figure 5.9: Simulink Model of the Dynamically Controlled System

No modal damping was included in the dynamic model used for control design. There are two reasons for this: any structural damping will tend to stabilize the system further, thus helping the stabilizing effect of the control law; and in a real space structure, it is very difficult to estimate the modal damping coefficients before the structure has been placed in orbit. Figure 5.10 shows the time history of displacement, for the same location (node 24) as used in the velocity feedback control case. Figure 5.11 shows the control signals for this case. A comparison with the case of negative velocity feedback shows that the LQG controller does a better work in damping out the oscillations, leading the system to the equilibrium position with a faster settling time.

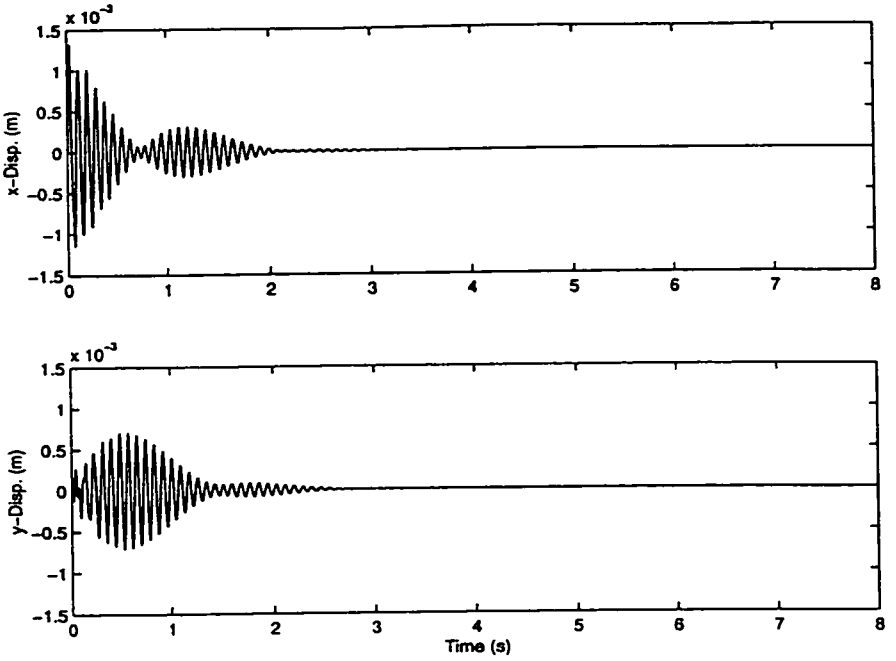

Figure 5.10: Displacement of Node 24. LQG Control (Simulation)

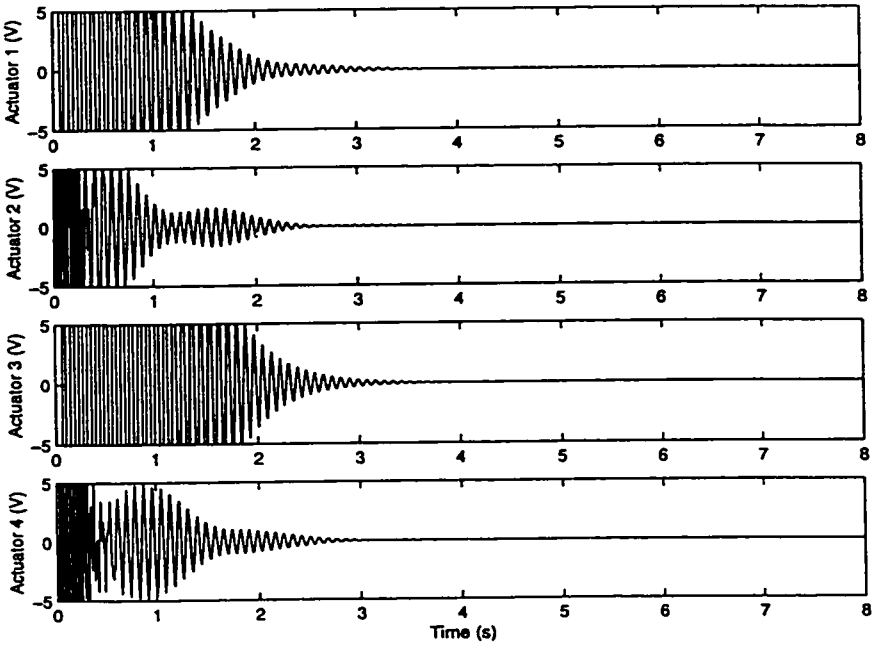

Figure 5.11: Control Signal. LQG Control (Simulation)

5.5. H_∞ Controller Design

A robust H_∞ feedback controller was designed for the truss structure. To obtain the controller using this technique, the dynamic model of the system has to be written in lower Linear Fractional Transformation (LFT) form. This formulation framework is convenient because it allows for the inclusion of the effects of the sensor and control disturbances, as well as loop-shaping weights on the inputs and outputs in a very compact and straightforward way. Figure 5.12 shows the block representation of the lower LFT form of the control problem

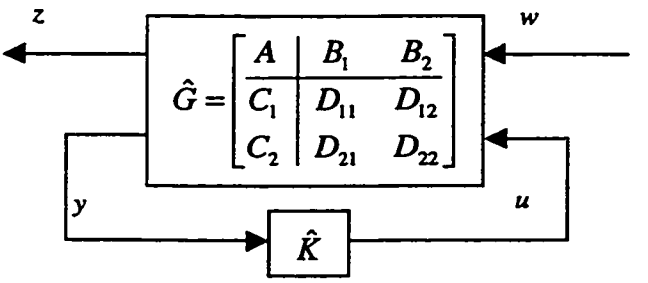

Figure 5.12: Lower LFT Representation of Control Problem

From Figure 5.12, it is possible to obtain the relation between the exogenous and controlled outputs z and y, the exogenous and control inputs w and u, and the system matrices:

$$\dot{x} = Ax + B_1 w + B_2 u$$
$$z = C_1 x + D_{11} w + D_{12} u$$
$$y = C_2 x + D_{21} w + D_{22} u$$

The dynamic controller that minimizes the H_∞ norm of the closed loop is given by (Gahinet [20]):

$$\hat{K} = \left[\begin{array}{c|c} A_k & B_k \\ \hline C_k & D_k \end{array}\right]$$

The state space matrices that form the controller are found from the solution of the following matrix inequality, where the unknowns are X_L and J:

$$H_{X_L} + Q^* J^* P_{X_L} + P_{X_L} J Q < 0 \tag{5.1}$$

where

$$J = \begin{bmatrix} A_k & B_k \\ C_k & D_k \end{bmatrix} \qquad H_{X_L} = \begin{bmatrix} \overline{A}^* X_L + X_L \overline{A} & X_L \overline{B} & \overline{C}^* \\ \overline{B}^* X_L & -I & D_{11}^* \\ \overline{C} & D_{11} & -I \end{bmatrix}$$

$$\overline{A} = \begin{bmatrix} A & 0 \\ 0 & 0_{n_k x n_k} \end{bmatrix} \qquad \overline{B} = \begin{bmatrix} B_1 \\ 0 \end{bmatrix} \qquad \underline{B} = \begin{bmatrix} 0 & B_2 \\ I & 0 \end{bmatrix}$$

$$\underline{C} = \begin{bmatrix} 0 & I \\ C_2 & 0 \end{bmatrix} \qquad \overline{C} = [C_1 \quad 0] \qquad \underline{D_{21}} = \begin{bmatrix} 0 \\ D_{21} \end{bmatrix} \qquad \underline{D_{12}} = [0 \quad D_{12}]$$

$$P_{X_L} = \begin{bmatrix} \underline{B}^* X_L & 0 & \underline{D_{12}}^* \end{bmatrix} \qquad Q = \begin{bmatrix} \underline{C} & \underline{D_{21}} & 0 \end{bmatrix}$$

It can be shown that if a controller exists, then X_L can be formed as

$$X_L = \begin{bmatrix} X & X_2 \\ X_2^* & I \end{bmatrix} \qquad X - Y^{-1} = X_2 X_2^*$$

where X and Y are the solutions to the following linear matrix inequalities:

$$\begin{bmatrix} N_y & 0 \\ 0 & I \end{bmatrix}^* \begin{bmatrix} A^*X + XA & XB_1 & C_1^* \\ B_1^*X & -I & D_{11}^* \\ C_1 & D_{11} & -I \end{bmatrix} \begin{bmatrix} N_y & 0 \\ 0 & I \end{bmatrix} < 0$$

$$\begin{bmatrix} N_x & 0 \\ 0 & I \end{bmatrix}^* \begin{bmatrix} AY + YA^* & B_1 & YC_1^* \\ B_1^* & -I & D_{11}^* \\ C_1Y & D_{11} & -I \end{bmatrix} \begin{bmatrix} N_x & 0 \\ 0 & I \end{bmatrix} < 0$$

where

$$\mathrm{Im}(N_y) = \mathrm{Ker}\begin{bmatrix} B_2^* & D_{12}^* \end{bmatrix}$$

$$\mathrm{Im}(N_x) = \mathrm{Ker}\begin{bmatrix} C_2 & D_{21} \end{bmatrix}$$

Once X_L has been found, the Matrix Inequality given in equation (5.1) becomes linear and can be solved using LMI solution techniques to obtain the matrix J, from which the controller matrices can be extracted. The LMI Lab toolbox of Matlab® contains functions to solve this type of problem. The next step in the control design process is to write the dynamic model of the system in lower LFT form. Figure 5.13 shows the conventional block diagram of the closed loop truss structure system, including the sensor noise and disturbances to the control:

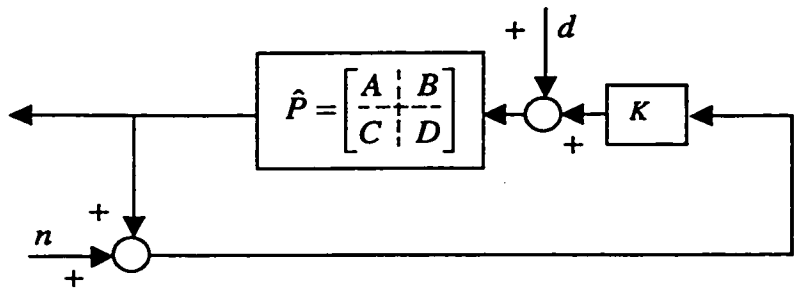

Figure 5.13: Block Diagram of the Closed Loop System

From this figure, it can be seen that the external input vector is comprised of the control disturbance d and the sensor noise n. Choosing the output vectors to contain the full state x and the control signal u allows shaping the open loop to improve the performance of a particular part of the state and the control. The resulting exogenous input and output vectors are:

$$w = \begin{Bmatrix} d \\ n \end{Bmatrix} \qquad z = \begin{Bmatrix} x \\ u \end{Bmatrix}$$

The design methodology explained above allows for the optimization of the response of the closed loop system using loop-shaping techniques. Loop shaping techniques use information about the nature of the exogenous input such as the sensor noise and control signal disturbances to select adequate filters that can be applied on the input and output signals to improve the response. Figure 5.14 shows the block diagram of the lower LFT model of the system, including an input filter $\hat{W}_1$ and an output filter $\hat{W}_2$.

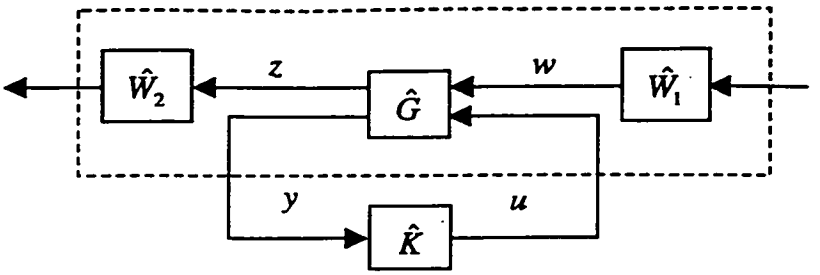

Figure 5.14: Shaping of the Open Loop

The system model can be uncertain over different frequency ranges. For example, uncertainty in the high frequency region can result from modal truncation. Uncertainty in the low frequency can result from low frequency disturbances being applied to the system due to ground movements. The uncertainty can be handled by specifying appropriate filters in $\hat{W}_1$ to introduce robustness to the perturbations in the model dynamics. The output filter $\hat{W}_2$ can be used to introduce performance requirements by placing weights on different elements of the control signal and state space.

The simulation was performed using the same sensor and actuator configuration as for the LQG case. For the preliminary simulations no input filter $\hat{W}_1$ was applied. Since the output vector z was designed to contain the state space and the control input, the output weighting matrix $\hat{W}_2$ was chosen to place increasing weight on the modal amplitudes and a relatively small weight on the control amplitudes.

As it was noted for the LQG controller case, the effect of sensor and control spillover due to the truncation of the model during the control design process is examined. A 5^{th} order model is used for control design, while in the simulation a 30^{th}

order model is employed. Details of the controller design process as well as the state space matrices for the controller are given in Appendix B. Figure 5.15 shows a Maximum Singular Value plot, which clearly shows the increased damping of the first five modes of the closed loop system as compared to the open loop system. It also shows that outside this range, the frequency response of the system is almost unchanged, which reflects robustness to the spillover problem.

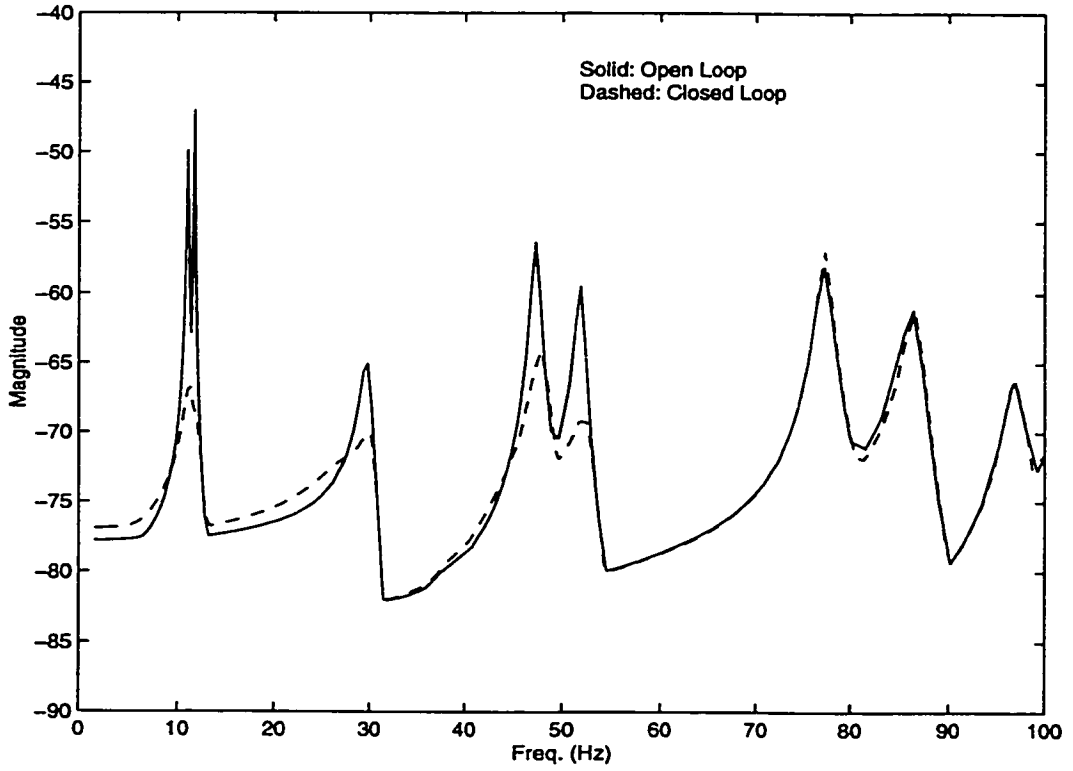

Figure 5.15: Maximum Singular Value Plot. H_∞ Control

The Simulink model used for this simulation is the same as the one used in LQG control, shown in Figure 5.9. The displacement and control signal response are shown in Figure 5.16 and Figure 5.17, respectively, for the same location (node 24) and actuators

as in the previous cases. The performance is better than the ones obtained with both velocity feedback control and LQG control. The settling time is lower. The controller exhibits the robustness to higher order dynamics that the velocity feedback control has, together with the ability to target specific modes of vibration by using penalties in the state and control outputs, as it is the case in LQG control.

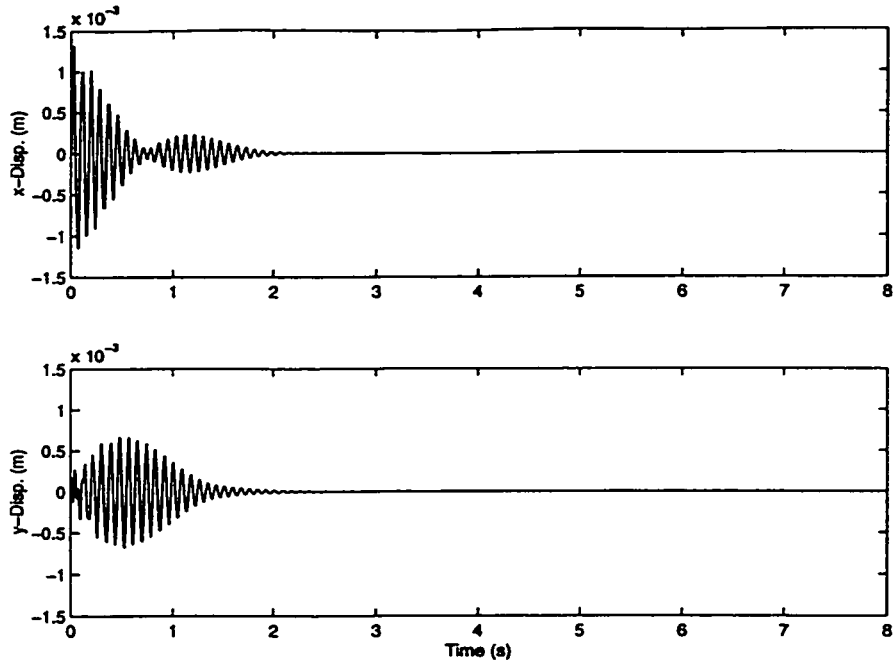

Figure 5.16: Displacement of Node 24. H_∞ Control (Simulation)

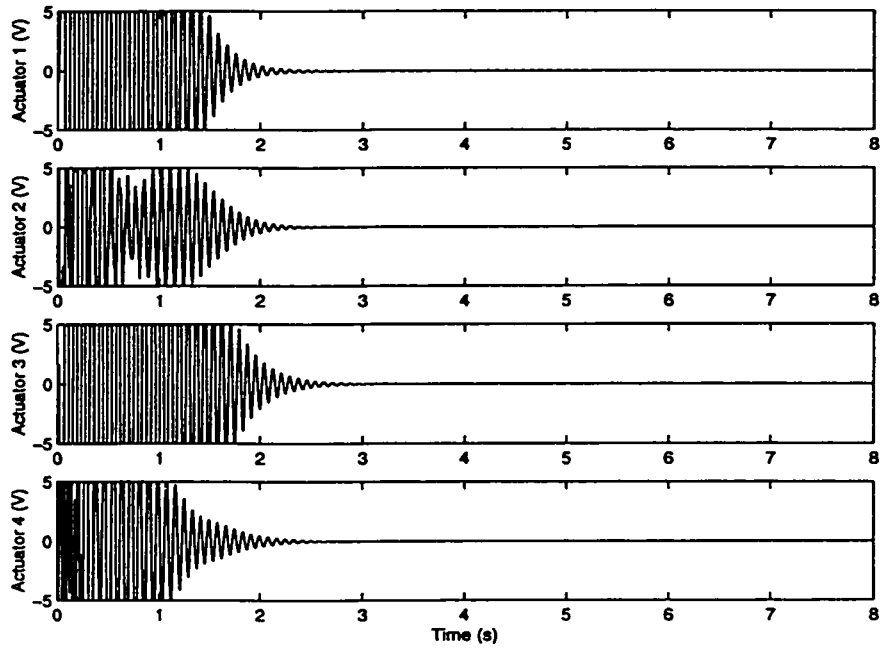

Figure 5.17: Control Signals. H_∞ Control (Simulation)

5.6. Summary

In this chapter, the design and simulation of several control laws for the truss structure presented in chapter 4 is shown, taking advantage of the use of piezoelectric actuators and sensors. Three control techniques are tested: negative velocity feedback, LQG and H_∞ control. Simulations are performed on the closed loop system (truss structure model plus control system) to assess the relative merits of each control technique.

Results of the simulations show that the robust H_∞ controller provides the better performance of the control techniques presented, even in the presence of higher order dynamics not accounted for in the control design process. However, optimal control techniques (LQG control and H_∞ control) are dynamic control techniques, in which the controller is of the same order as the system dynamic model. Because of this, LQG and H_∞ controllers have the capability of directing the control energy to specific modes of vibration.

From the point of view of controller complexity, the negative velocity feedback control technique is attractive, because it involves only static feedback, which results in a simpler controller to implement. The velocity feedback controller is also independent of the dynamic model, which adds a measure of robustness to parametric or modelling uncertainties.

The simulation results obtained are corroborated using an experimental testbed, to confirm the validity of the assumptions made during the modelling and simulation process. Those results are presented in chapter 6.

6. Experimental Verification

6.1. Introduction

The experimental implementation of the truss structure and controller techniques presented in chapters 4 and 5 are described in this chapter. A detailed description of the experimental testbed is shown in section 6.2, including construction details, as well as descriptions of the instrumentation and electronic hardware. Section 6.3 shows the results of the impact test on the testbed with nominal parameters for the open loop (uncontrolled), velocity feedback, LQG and H_∞ controller cases. Section 6.4 shows the impact test results for an altered structure. The structure is altered by adding a 1.625 Kg. mass at the top of the structure, thus modifying the mode frequencies and shapes. The controllers are the same as the ones used for the nominal system In section 6.5, experimental results of a continuous disturbance test are presented. This test is performed to examine the behaviour of the system to a continuous source of vibration, such as unbalanced rotary equipment.

6.2. Description of the Experimental Testbed

The basic configuration of the truss was described in section 4.2. Figure 6.1 shows a picture of the complete truss structure, including some of the associated electronics.

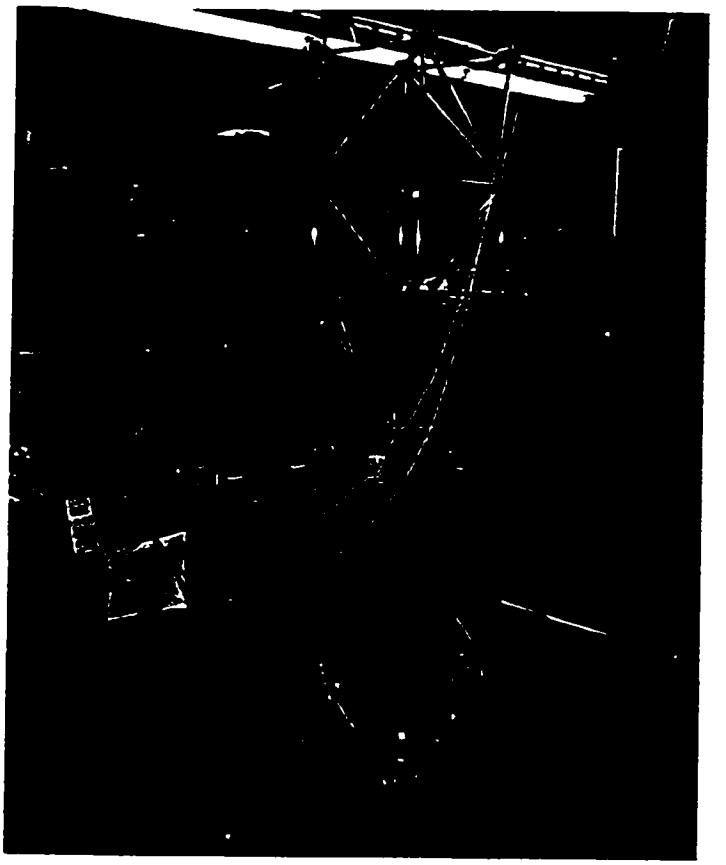

Figure 6.1: Truss Structure

The active truss members, shown in Figure 6.2, are fitted with two identical Polyvinyldene Di-Fluoride (PVDF) rectangular piezoelectric sensors. One sensor measures the open circuit voltage, which is proportional to the strain. The second measures short circuit current, which is proportional to the strain rate. In the mid-span of the active truss member there is a piezoceramic actuator, that receives the control signal and transforms it into actuation forces. The properties and dimensions of the sensors and actuators are given in section 5.2, Table 5.1 and Table 5.2.

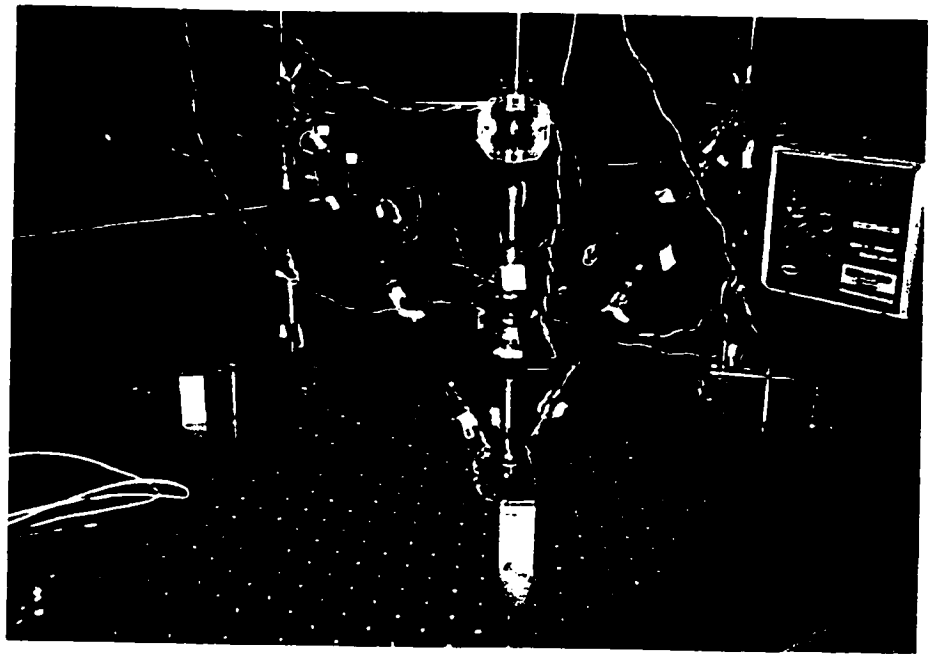

Figure 6.2: Active Truss Members

The truss members are bonded to the junction blocks using a liquid plastic solvent containing methylene chloride. Each bay is a 300 mm cube. The properties and dimensions of the polycarbonate truss members are presented in Table 4.1, while construction details are shown in Figure 4.2, Figure 4.3 and Figure 4.4 in section 4.2.

Figure 6.3 shows a schematic of the components of the truss structure testbed. The control logic is to be performed in a Pentium-based computer, running Matlab® and Simulink® together with the Real-time toolbox and Wincom® software, interfacing to the system via a Quanser MultiQ-3 I/O card. The Multi-Q- card is capable of supporting 8 input ADC and 8 output DAC channels at a resolution of 12 bits plus sign for the A/D conversion, 12 bits unsigned for the D/A conversion, and a sampling frequency of up to 15 kHz. Piezoelectric film actuators and sensors are bonded to the truss structure. Each piezoceramic actuator is driven by a custom designed high voltage amplifier that is

described Section 6.2.1. A HP 6521A DC high voltage power supply is used to power the high voltage amplifiers. In addition, for calibration purposes, strain gauges are fitted to some of the truss members, and two accelerometers are installed at the top corner of the structure, for displacement and frequency response measurements.

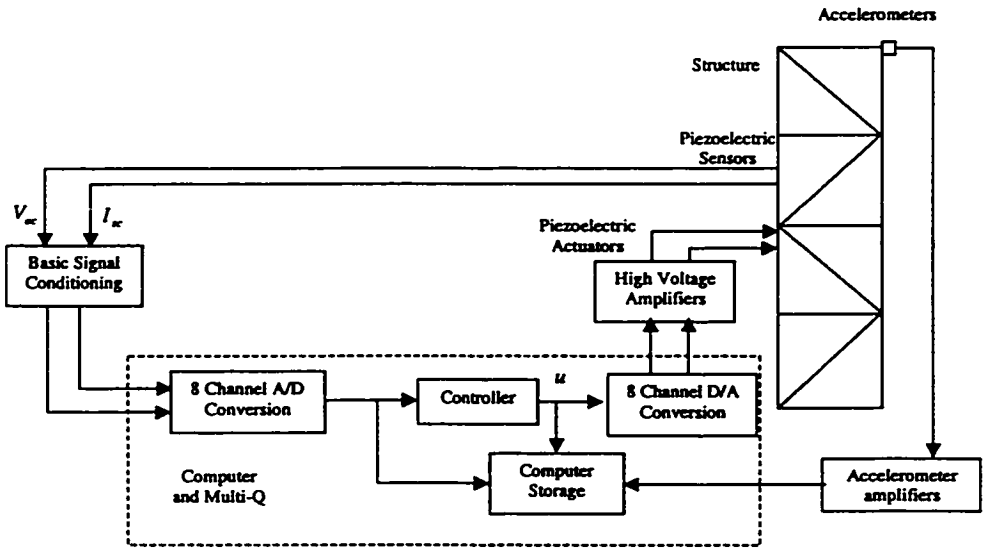

Figure 6.3: Schematic of Testbed System Architecture

6.2.1 High Voltage Amplifier for Piezoelectric Actuators

A high voltage amplifier was designed and built for the purpose of driving the piezoceramic actuators. A detailed description of the amplifier, including performance curves, is presented in Bravo *et al.* [11]. In designing the amplifier there were several factors taken into consideration. These are the source of the input signal, the type of load that the amplifier is to drive, the required frequency response and finally the high voltage power supplies available to power the circuit. The amplifier is to be used to amplify the low voltage signals from a Digital to Analog (D/A) board and produce high voltage output signals suitable for operating piezoceramic actuators.

The amplifier is designed to amplify the outputs of a Quanser MultiQ-3 I/O card installed in a computer. The D/A outputs of this card are capable of producing voltage signals in the range of –5V to +5V and are meant to drive a high impedance load. To accommodate the full range of input signal voltages the low-voltage portion of the amplifier is designed to run from a ±20V DC power supply. The amplifier input impedance is set to 10 MΩ to avoid loading the output of the D/A card and DC coupling is chosen to ensure that low frequency signals are not attenuated.

The load that the amplifier is intended to drive is a piezoceramic. In order to make the amplifier more versatile it is designed to work with any generic piezoceramic actuator. To work properly all actuators of this type require application of a high voltage signal. To the amplifier they appear as a high impedance capacitive load. To produce the necessary forces from the actuator, voltage signals of approximately 500V peak-to-peak are required. A Hewlett Packard 6521A DC power supply is used to provide 600V DC potential to the high voltage section of the amplifier. All components on the high voltage side of the amplifier are then chosen to have appropriate voltage ratings. Based on the input voltage range and the output voltage range a fixed voltage gain of 53 V/V is chosen. Such a gain allows a maximum output voltage swing of 530Vp-p for the maximum input voltage swing of 10Vp-p. To ensure that very low frequency signals can be produced the output is DC coupled to the load. The cutoff frequency of the amplifier is designed to be greater than 1000 Hz, as this exceeds the bandwidth of the controller to be implemented. Piezoceramic elements can produce hundreds of volts of potential across their terminals when distorted by an externally applied force. Since the amplifier is connected to the actuator for extended periods its output terminal could be exposed to these voltages both

when power is applied to the amplifier and when the power is turned off. Because of this some protection was needed on the output. As a final precaution to protect the amplifier against a short circuit, some current limiting is also implemented.

After the amplifier had been constructed and the design finalized it was tested to ensure that the design specifications had been met. Five identical amplifiers are used in the experimental testbed: four for the control system and one to act as a disturbance source. Table 6.1 contains these results as well as recommended power supply specifications.

Table 6.1: Performance for the High Voltage Amplifier

Voltage gain	53 V/V
3dB Bandwidth	0Hz - 5kHz
Input Impedance	10 MΩ
Maximum input voltage	± 5V
Maximum output current	20mA
High Voltage Power supply	+600VDC, 30mA
Low Voltage Power supply	±15V, ±200mA

6.3. Experimental Results: Impact Test, Nominal System

The results of the impact experiments carried out using the testbed described before are shown in this section. "Nominal" system refers to the truss structure as designed, with no additional mass to modify the dynamics. The impact test is performed as described in Figure 5.2, to have similar conditions to the simulations, thus allowing for comparisons between simulations and experiments. The results are shown for the cases

of open loop (uncontrolled structure), negative velocity feedback control, LQG control and H_∞ control.

6.3.1 Open Loop

The open loop tests are carried out to have a reference against which to compare the performance of the control laws. The results were also used to calibrate the modal damping ratios in the test model used in the simulations. Figure 6.4 shows the displacement response of the system to the impact, obtained from double integration of the accelerometer signals. The small inherent structural damping of the system is visible. The structure oscillates without control for 8 seconds.

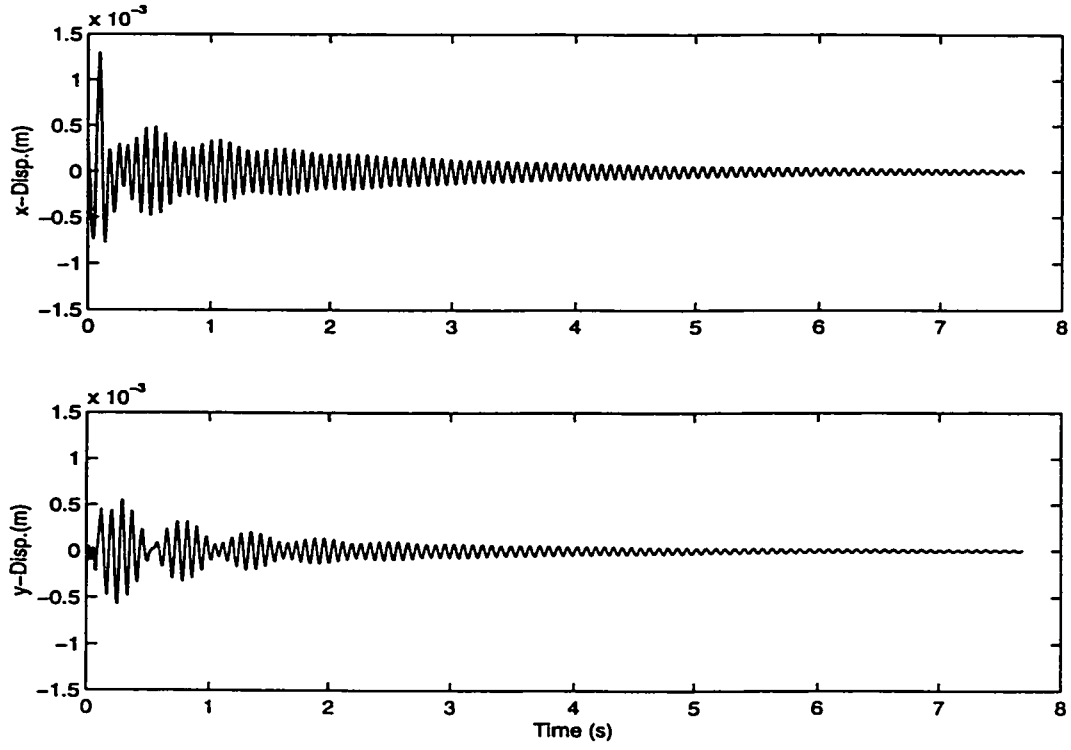

Figure 6.4: Displacement of Node 24. Open Loop (Experimental)

Figure 6.5 shows the frequency response of the open loop system. The dominant resonant peak corresponds to the second mode of vibration, at 13.3 Hz.

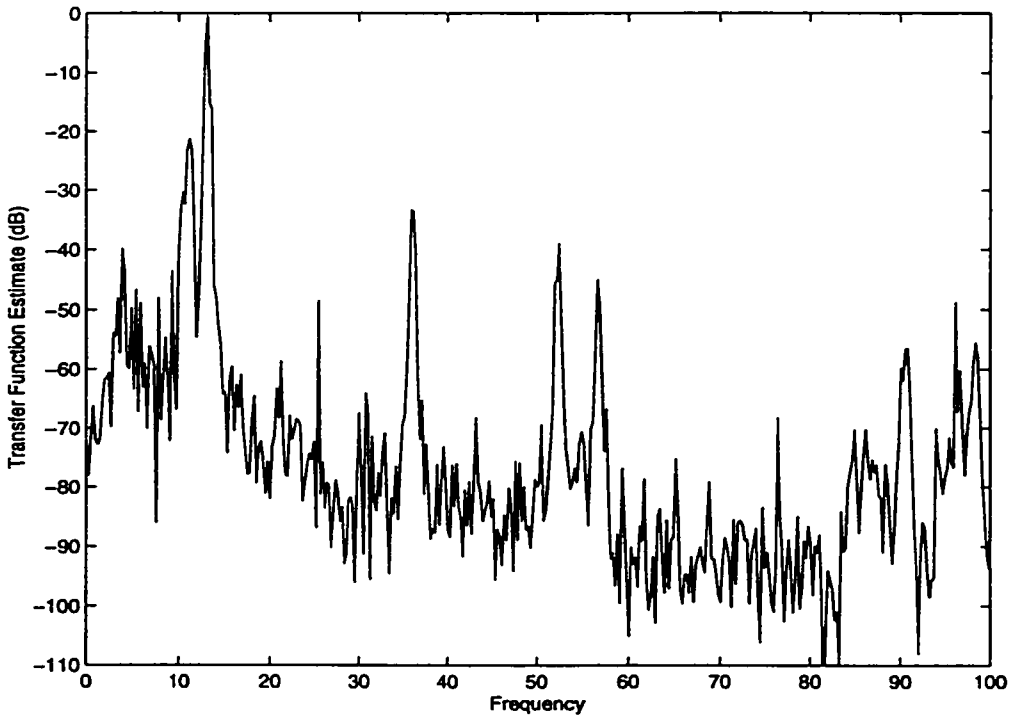

Figure 6.5: Frequency Response. Open Loop (Experimental)

6.3.2 Negative Velocity Feedback Control

For the experiments using the negative velocity feedback control law, the same feedback gains used in the simulations presented in section 5.3 were used. Figure 6.6 shows the displacement response, while Figure 6.7 shows the control signal to the amplifiers. The controller is able to damp out the oscillations in less than four seconds. The control signal shows saturation on some of the actuators during the first second after the impact. The displacement and control traces match well with the ones obtained in the simulations, shown in Figure 5.6 and Figure 5.7

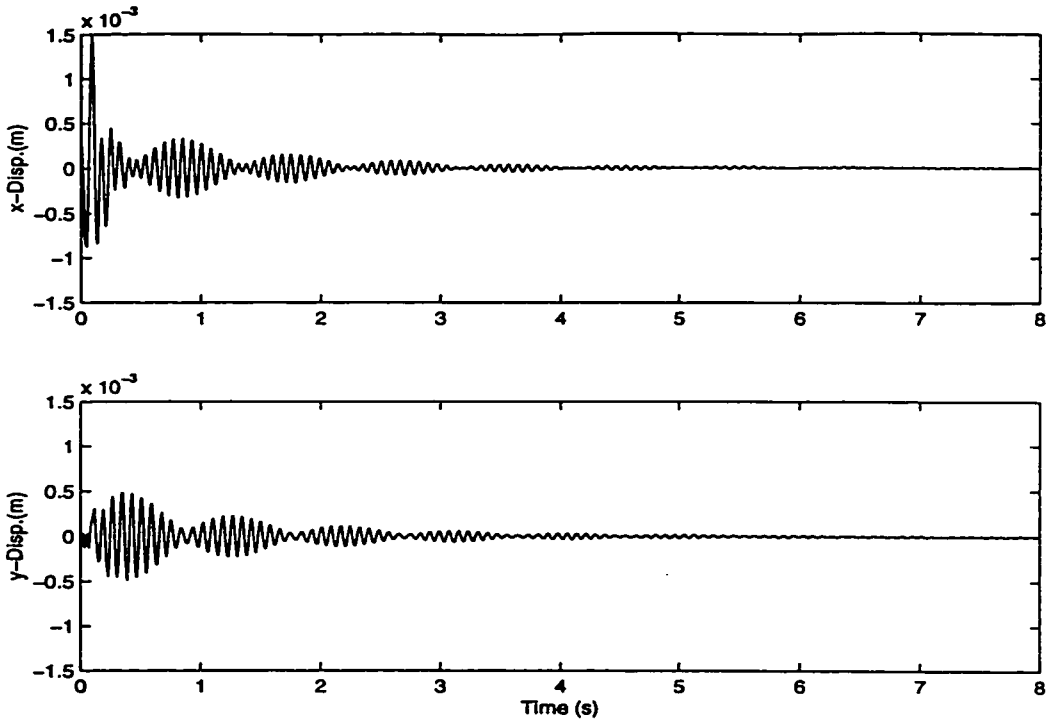

Figure 6.6: Displacement of Node 24. Velocity Feedback Control (Experimental)

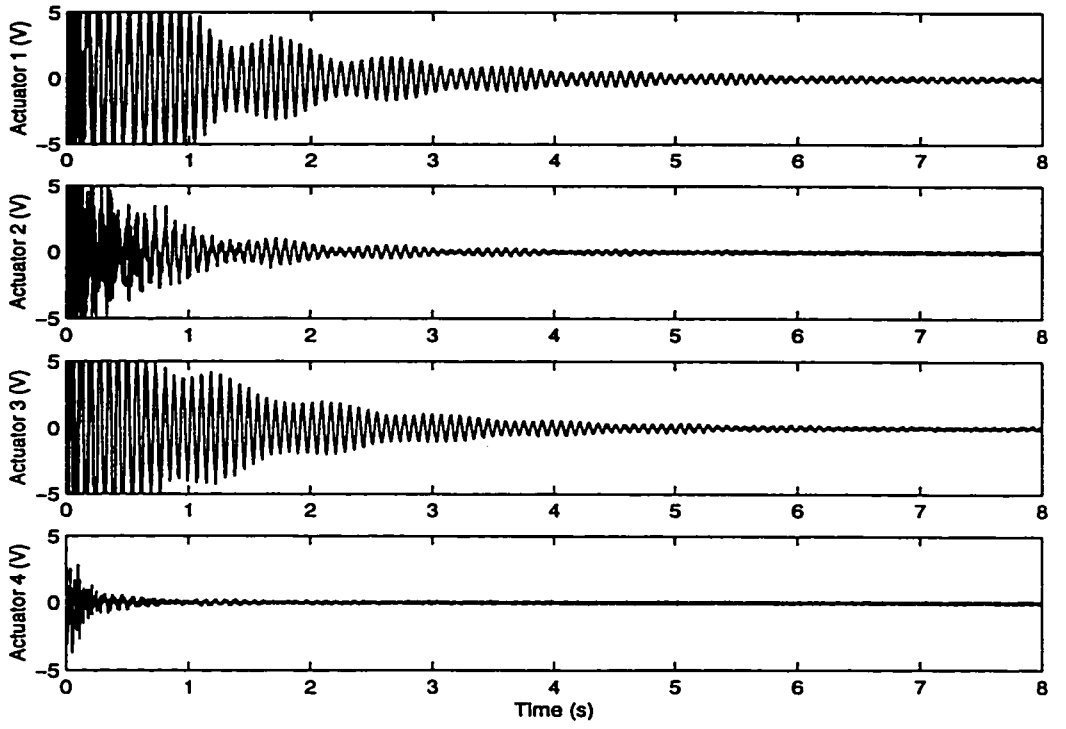

Figure 6.7: Control Signals. Velocity Feedback Control (Experimental)

Figure 6.8 shows the frequency response of the closed loop for the velocity feedback controller, showing a decrease of 10 dB in the dominant peak when compared to the open loop case, and proportional decreases in the other resonant peaks under 60 Hz.

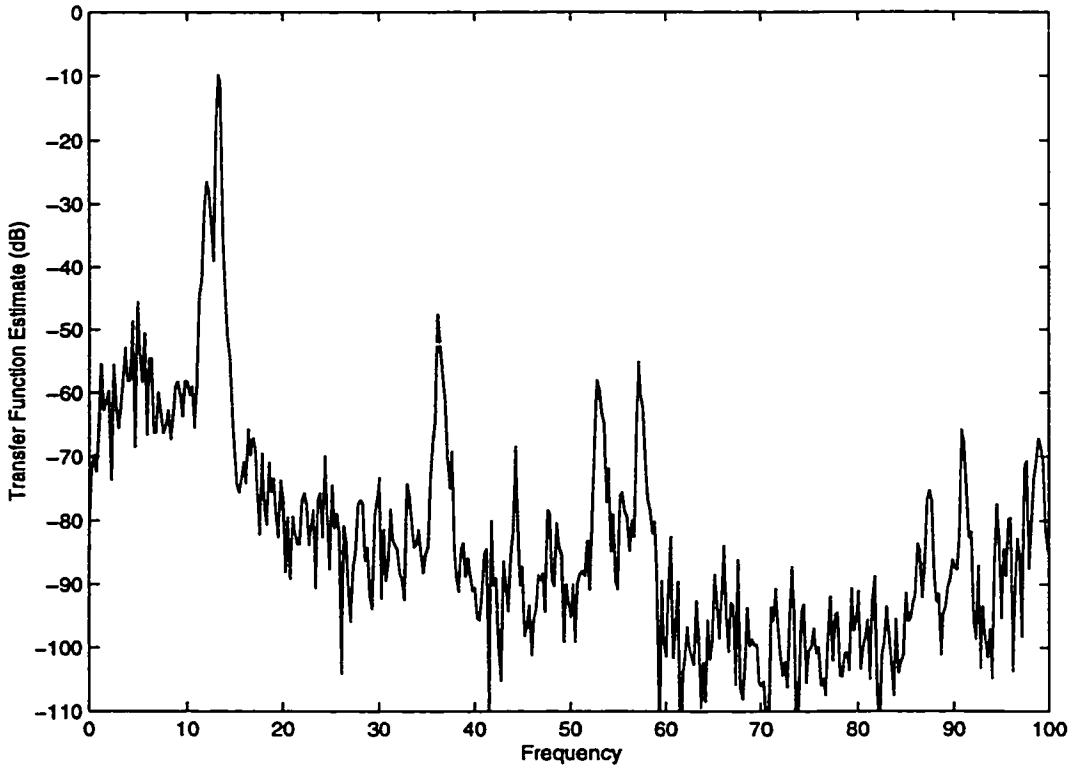

Figure 6.8: Frequency Response. Velocity Feedback Control (Experimental)

6.3.3 LQG Control

The LQG controller designed using the procedure shown in section 5.4 and listed in Appendix A was used for the experiments. The displacement response of Figure 6.9 show a better performance than the one obtained with the velocity feedback controller, as predicted in the simulations. Note that the control activity is similar to the velocity feedback case. Figure 6.10 shows the corresponding control signals. The displacements and control traces show a good correlation when compared to the simulation results, shown in Figure 5.10 and Figure 5.11.

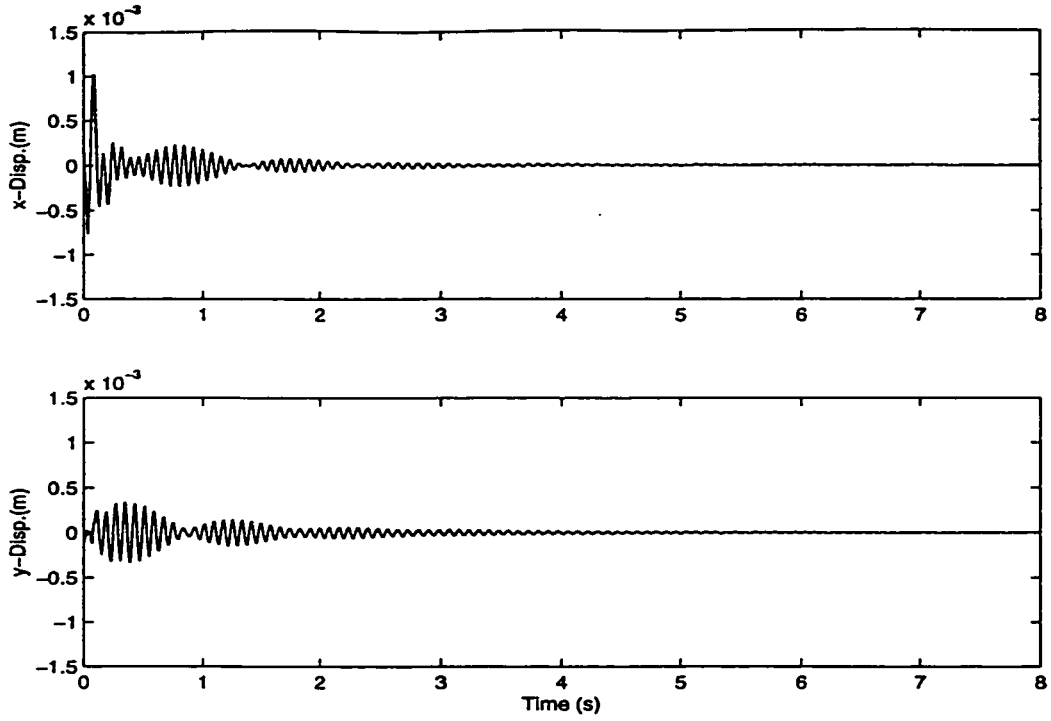

Figure 6.9: Displacement of Node 24. LQG Control (Experimental)

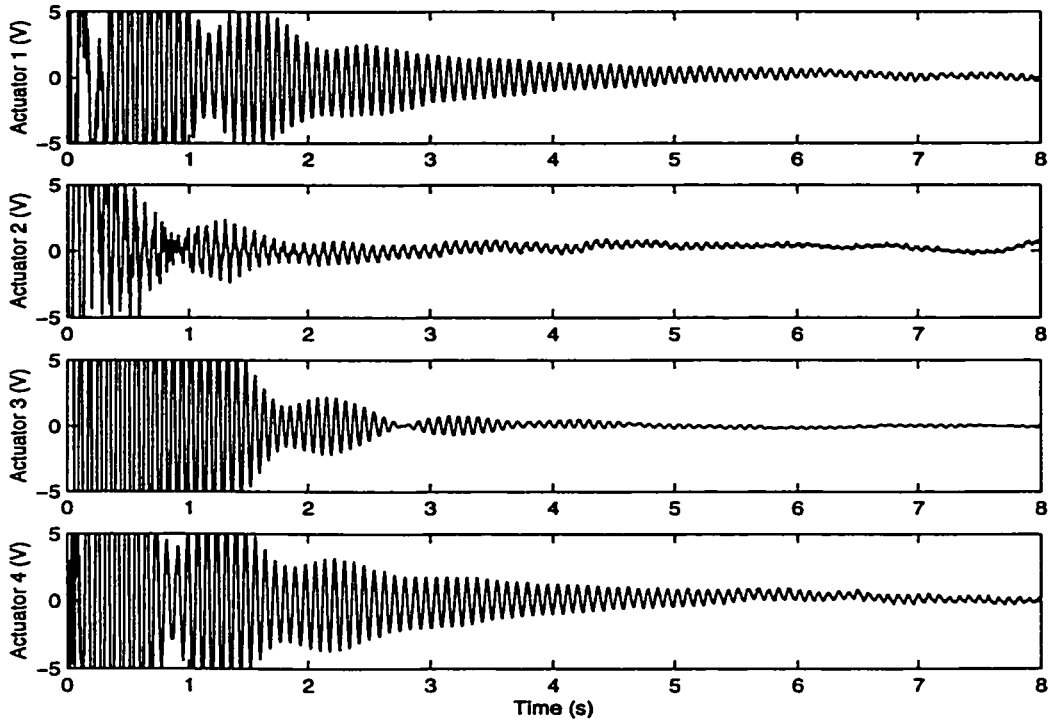

Figure 6.10: Control Signals. LQG Control (Experimental)

Figure 6.11 shows the frequency response plot for the closed loop LQG controlled system. The performance improvement noticed in the displacement trace is easy to appreciate. The maximum resonant peak has been attenuated nearly 20 dB compared to the open loop case, and 10 dB compared to the negative velocity feedback controller

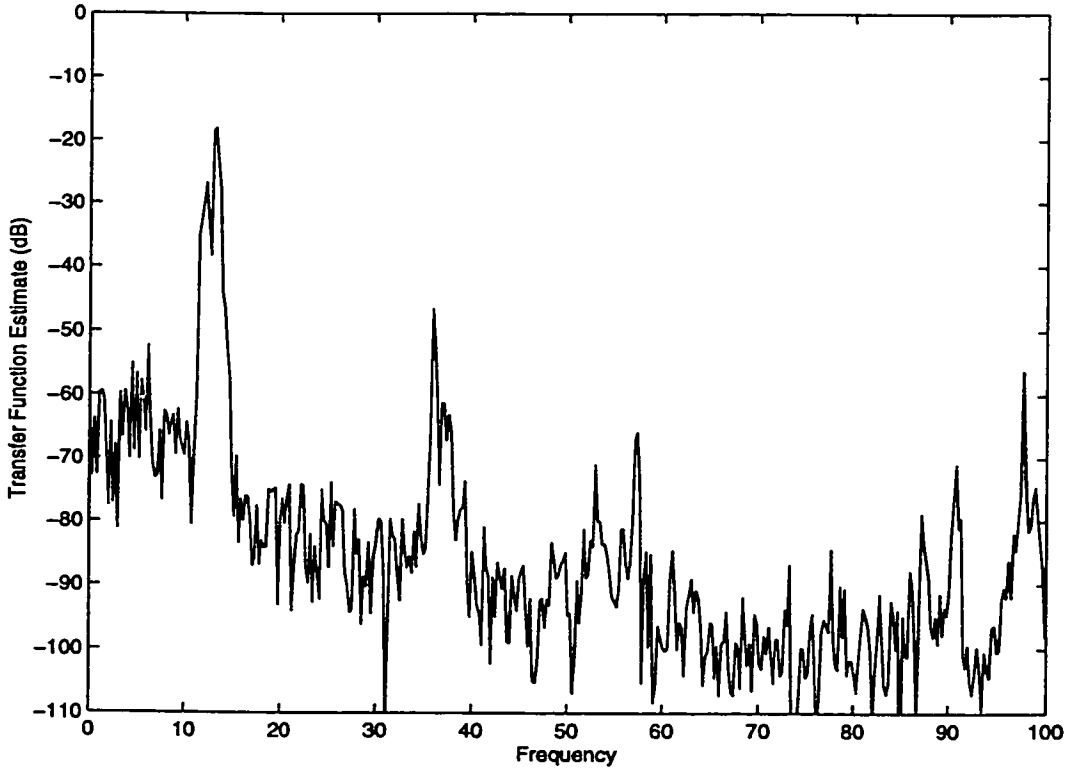

Figure 6.11: Frequency Response. LQG Control (Experimental)

6.3.4 H_∞ Control

The H_∞ controller design explained in section 5.5, and shown in Appendix B, was implemented on the experimental setup. The displacement and control signal traces, shown in Figure 6.12 and Figure 6.13, respectively, show better performance than the LQG controller in terms of settling time. The oscillations damp out in less than 2.5 seconds.

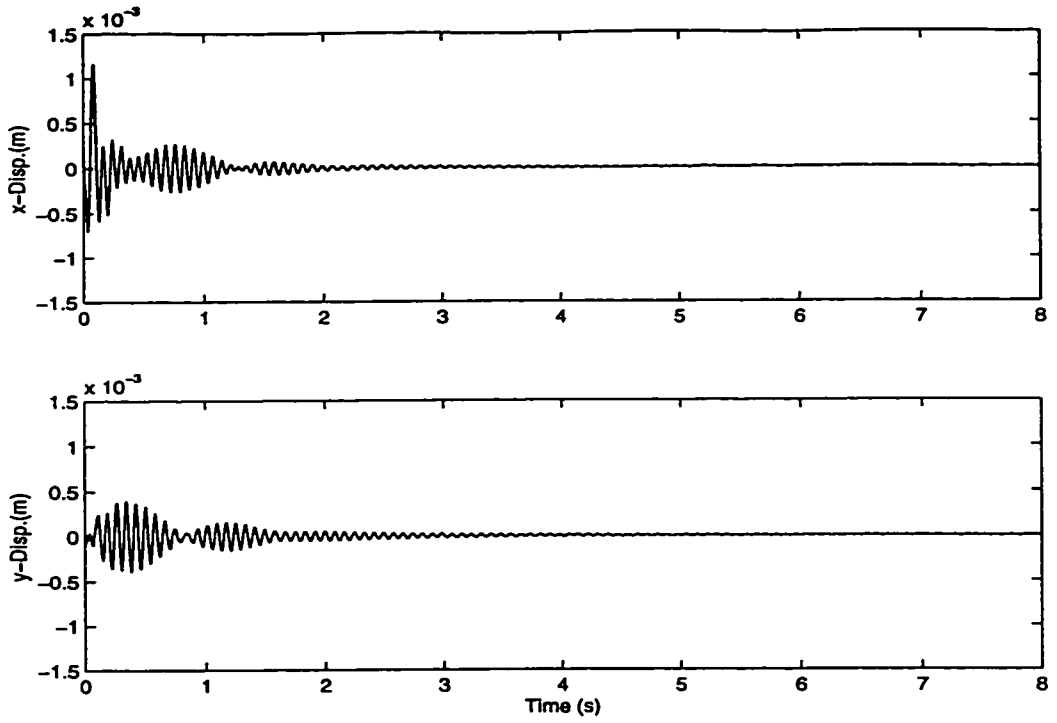

Figure 6.12: Displacement of Node 24. H_∞ Control (Experimental)

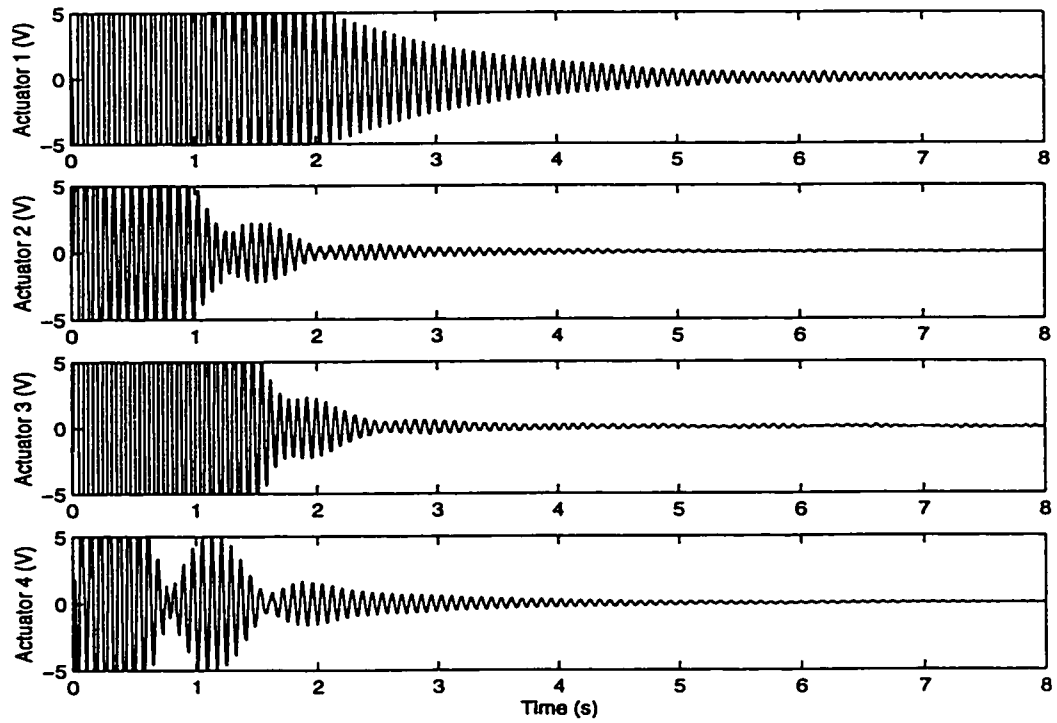

Figure 6.13: Control Signals. H_∞ Control (Experimental)

The improvement in performance is easier to notice in the frequency response plot, shown in Figure 6.14. The maximum resonant peak, at 13.3 Hz, is reduced by 5 dB when compared to the LQG controller case, and 25 dB when compared to the open loop case.

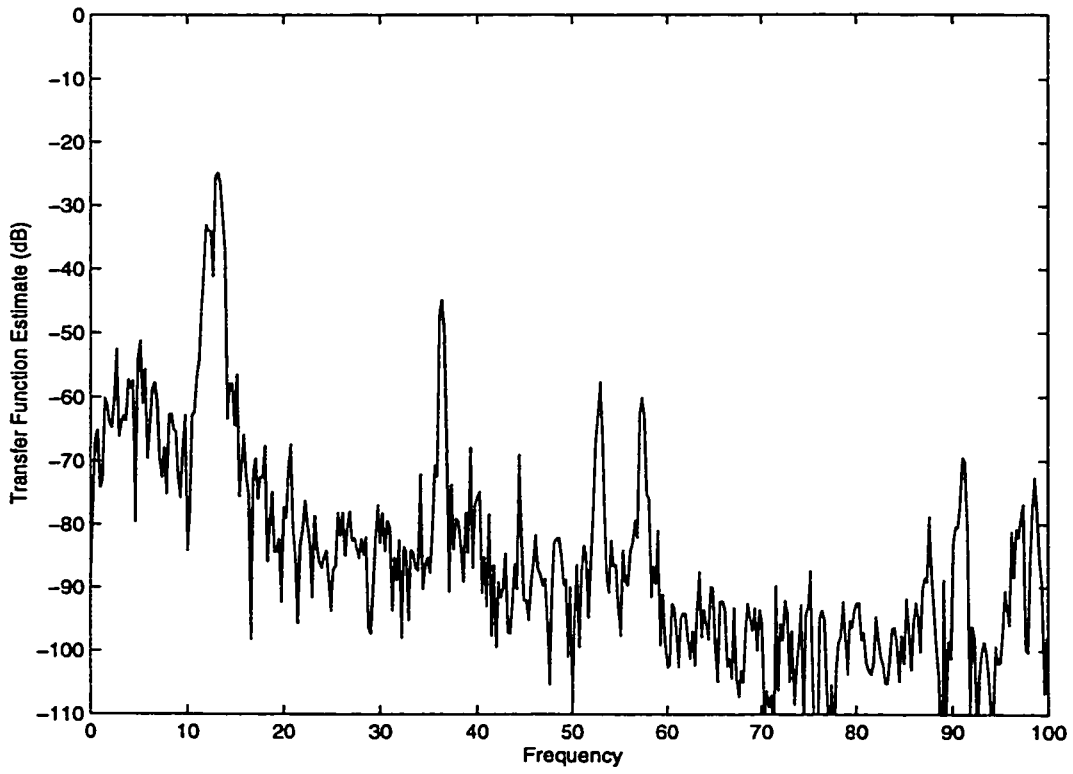

Figure 6.14: Frequency Response. H_∞ Control (Experimental)

6.4. Experimental Results: Impact Test, Altered Structure

In order to test the robustness of the different control techniques, the truss structure was altered by adding a mass of 1.625 Kg. at the top of the structure, as shown in Figure 6.15. This additional mass has the effect of modifying the dynamics of the structure by lowering the resonant frequencies and changing the mode shapes. Since the

controllers used for this experiments are the same as the ones used in the nominal case (section 6.3), this introduces parametric uncertainty to the controllers, which were designed using the parameters corresponding to the nominal structure. In the next sections, the structure with the additional mass is referred to as the "altered structure".

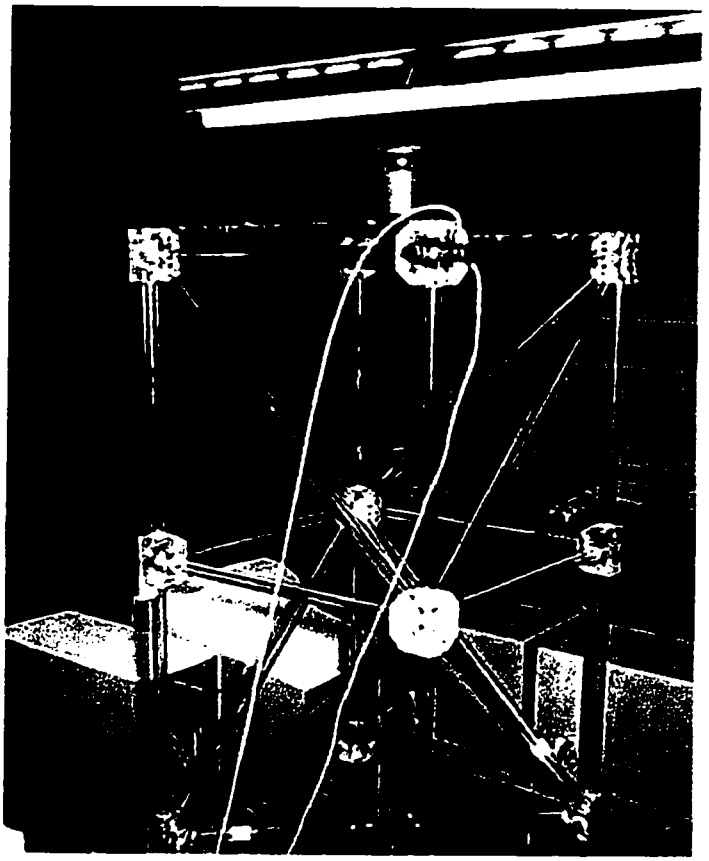

Figure 6.15: Structure with Additional Mass

6.4.1 Open Loop

The open loop behaviour of the altered structure is shown for reference purposes. The open loop displacement response of the structure to an impact is shown in Figure 6.16.

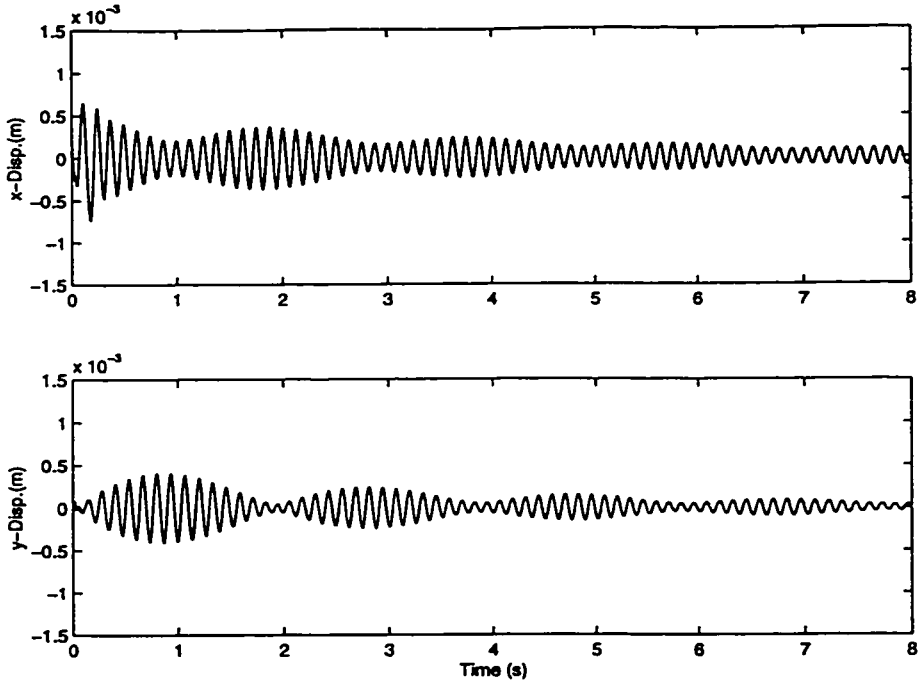

Figure 6.16: Displacement of Node 24. Altered Structure. Open Loop (Experimental)

Figure 6.17 shows the frequency response of the open loop system. The first two resonant frequencies dominate the spectrum; the first natural frequency occurs at 8 Hz instead of 12.5 Hz for the nominal structure.

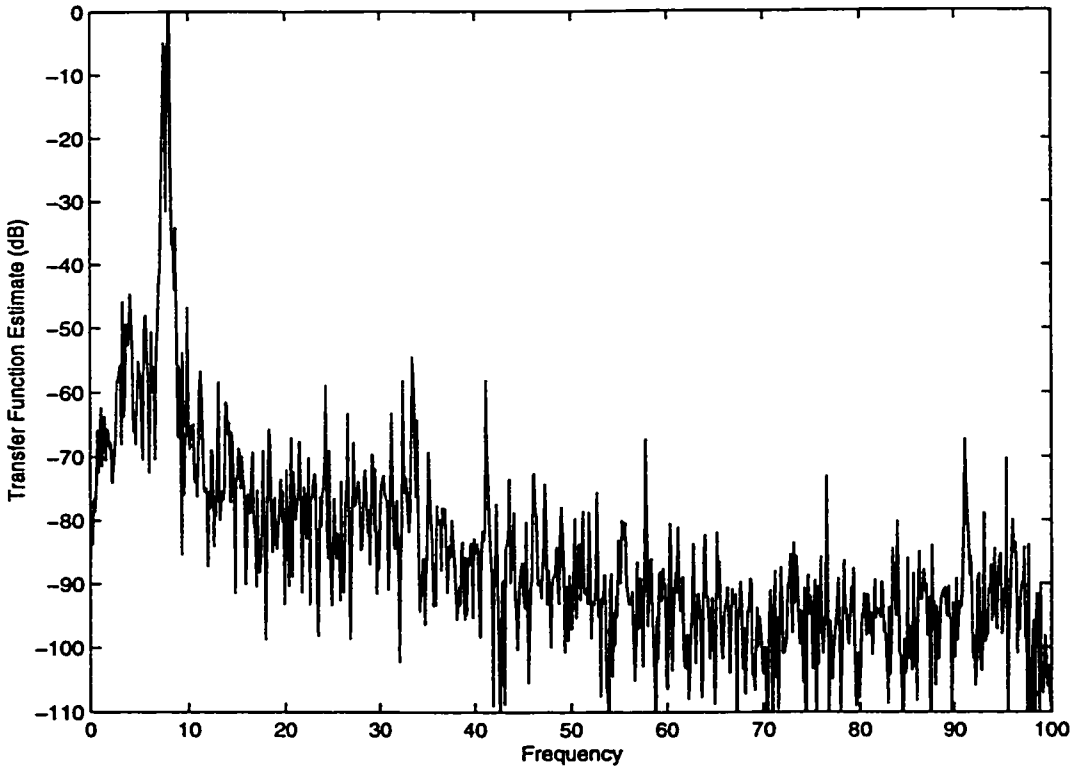

Figure 6.17: Frequency Response. Altered Structure. Open Loop (Experimental)

6.4.2 Negative Velocity Feedback Control

The displacement response of the perturbed system with negative velocity feedback control is shown in Figure 6.18. The additional damping provided by the control system is not as obvious as it is for the nominal case. This is because of the additional power required to damp the more massive structure, and the saturation limits of the actuator amplifiers. Figure 6.19 shows the control signal.

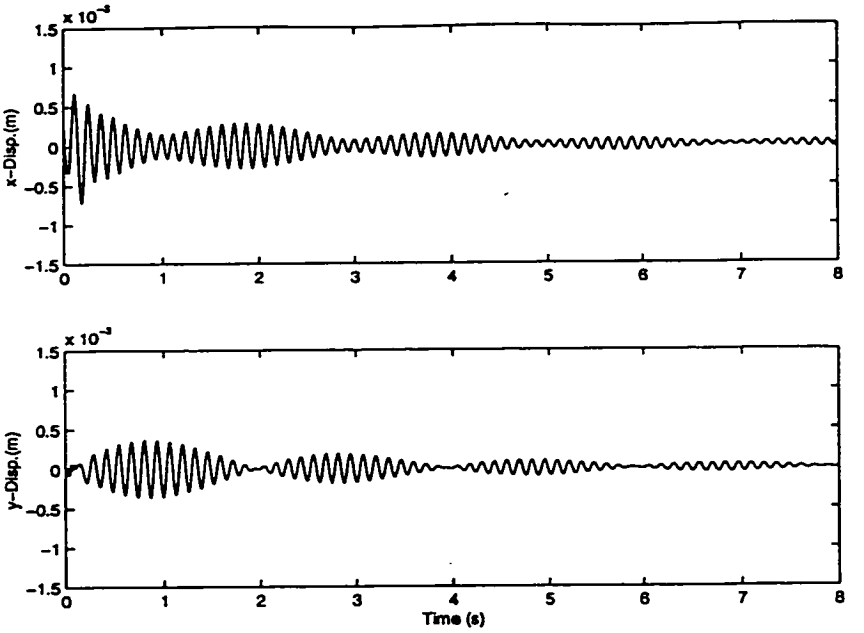

Figure 6.18: Displacement of Node 24. Altered Structure. Velocity Feedback Control (Experimental)

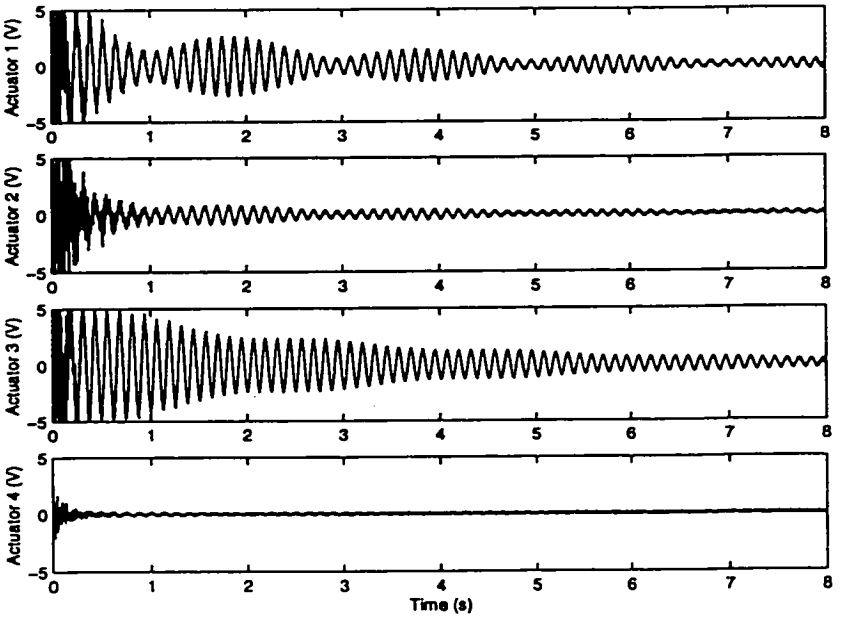

Figure 6.19: Control Signals. Perturbed Structure. Velocity Feedback Control (Experimental)

The frequency response of the velocity feedback controlled perturbed structure is shown in Figure 6.20. The attenuation of the dominant resonant peak is about 5 dB.

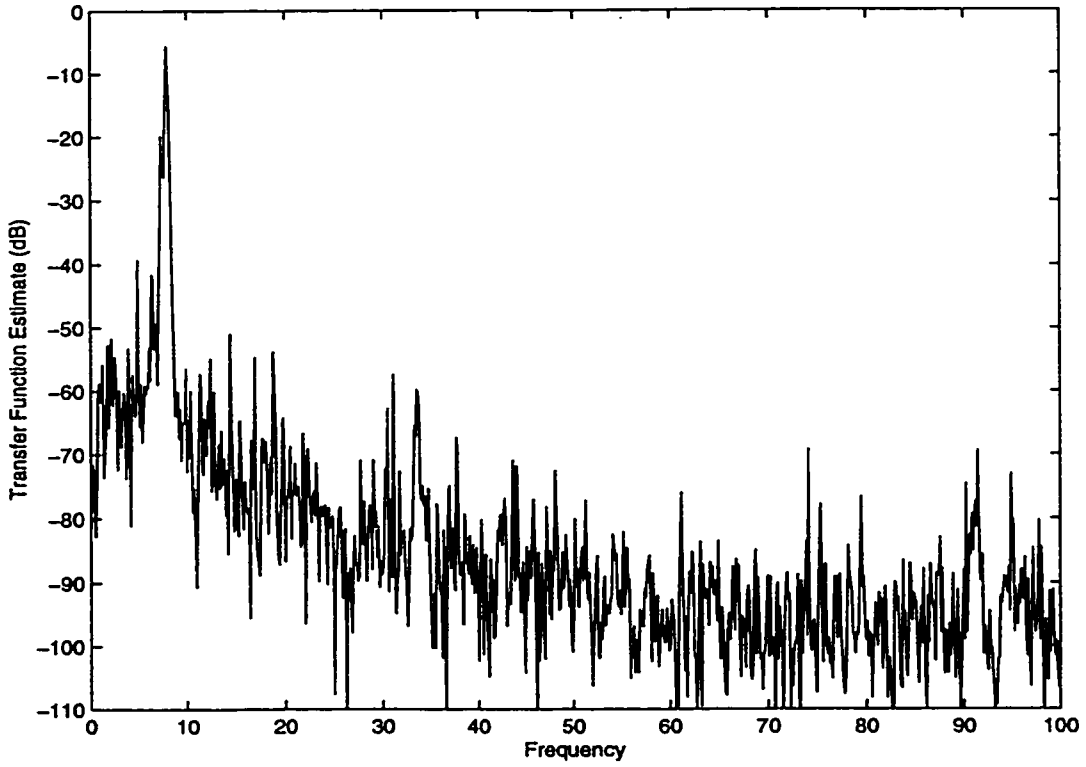

Figure 6.20: Frequency Response. Perturbed Structure. Velocity Feedback Control (Experimental)

6.4.3 LQG Control

The displacement response of the perturbed structure with LQG control to an impact is given in Figure 6.21, and the control signals are shown in Figure 6.22. The controller is capable of decreasing the settling time of the oscillations even in the presence of parametric uncertainty. The performance is better than in the velocity feedback case, at the cost of actuator saturation for a longer period of time.

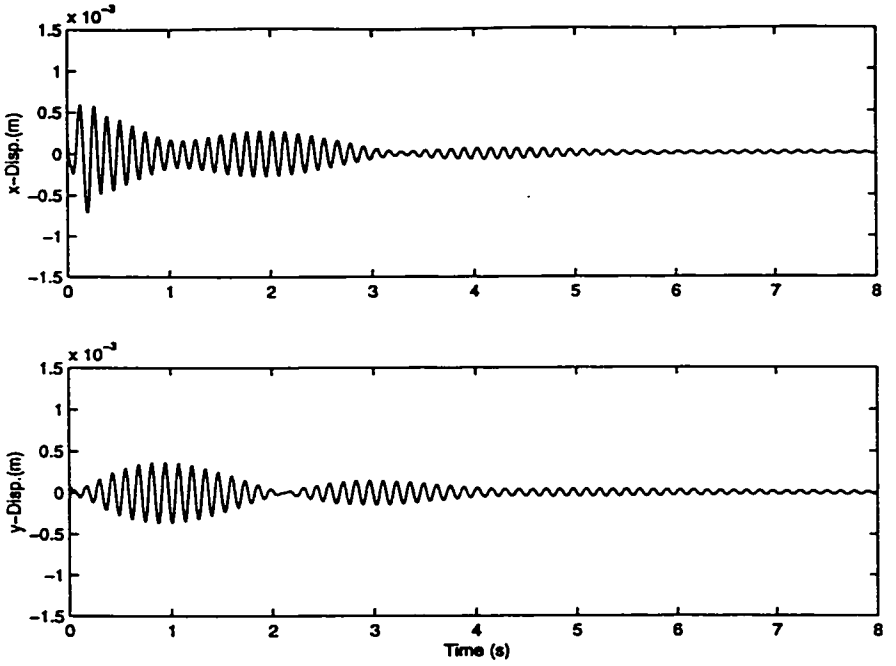

Figure 6.21: Displacement of Node 24. Altered Structure. LQG Control (Experimental)

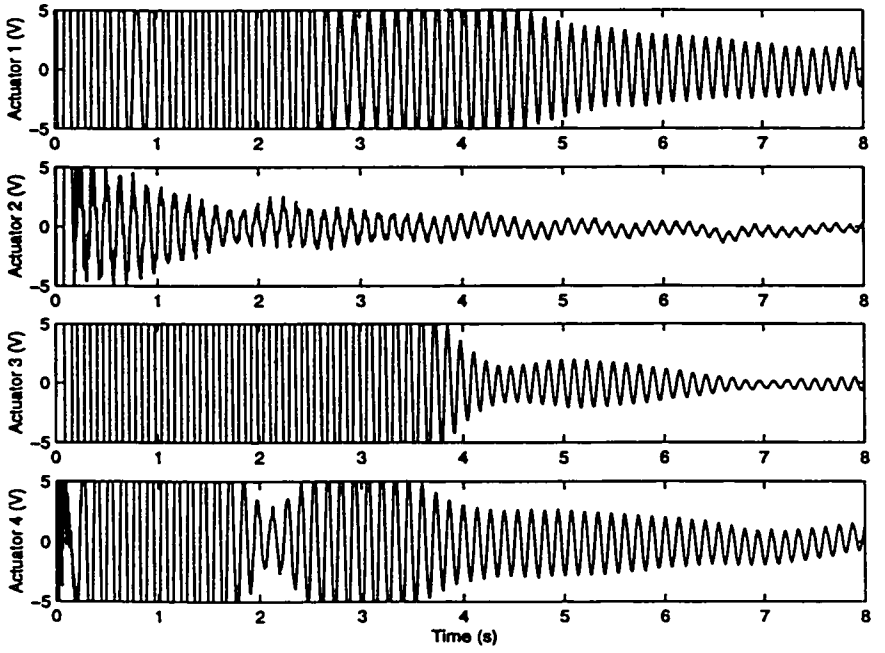

Figure 6.22: Control Signals. Altered Structure. LQG Control (Experimental)

The frequency response of the perturbed structure with LQG control is shown in Figure 6.23. The attenuation of the dominant peak is 10 dB with respect to the open loop case and 5 dB with respect to the velocity feedback case.

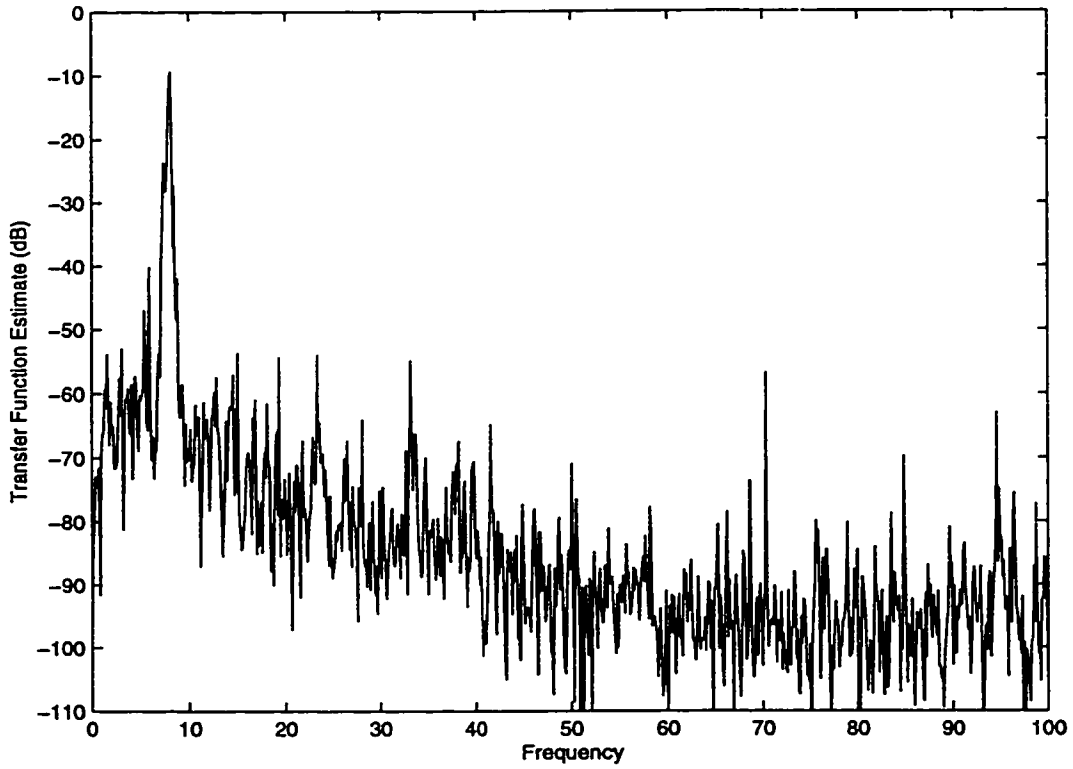

Figure 6.23: Frequency Response. Altered Structure. LQG Control (Experimental)

6.4.4 H_∞ Control

Figure 6.24 and Figure 6.25 show the displacement and control signal responses for the perturbed structure with H_∞ control. The settling time is the lowest of the controllers tested, with a lower control activity that the one corresponding to LQG control.

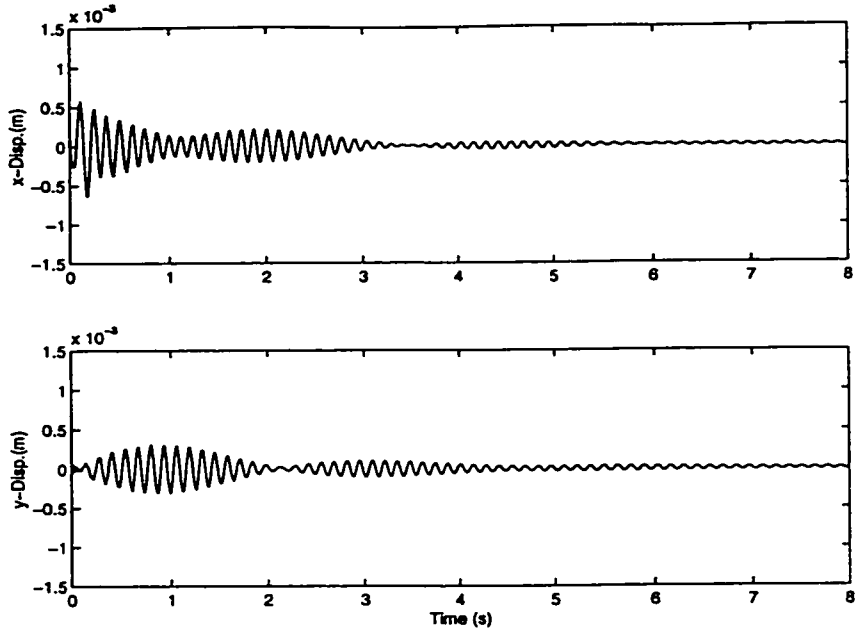

Figure 6.24: Displacement of Node 24. Altered Structure. H_∞ Control (Experimental)

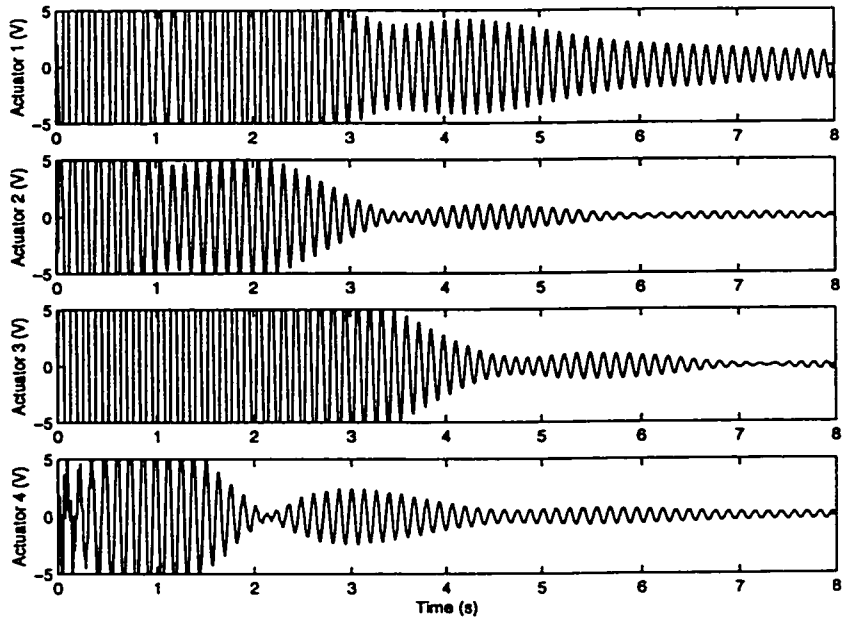

Figure 6.25: Control Signals. Altered Structure. H_∞ Control (Experimental)

Figure 6.26 shows the frequency response plot. The attenuation of the dominant resonant peak is about 13 dB; this is the best performance of the three controllers tested. A peak at the third natural frequency can be appreciated, which is not present in the previous frequency responses. It is important to note that the H_∞ controller tries to minimize the maximum gain over all frequencies, such that it is possible to see a frequency "waterbed effect"; this means that at some frequencies the frequency response can be increased, but the maximum peak is still lowered.

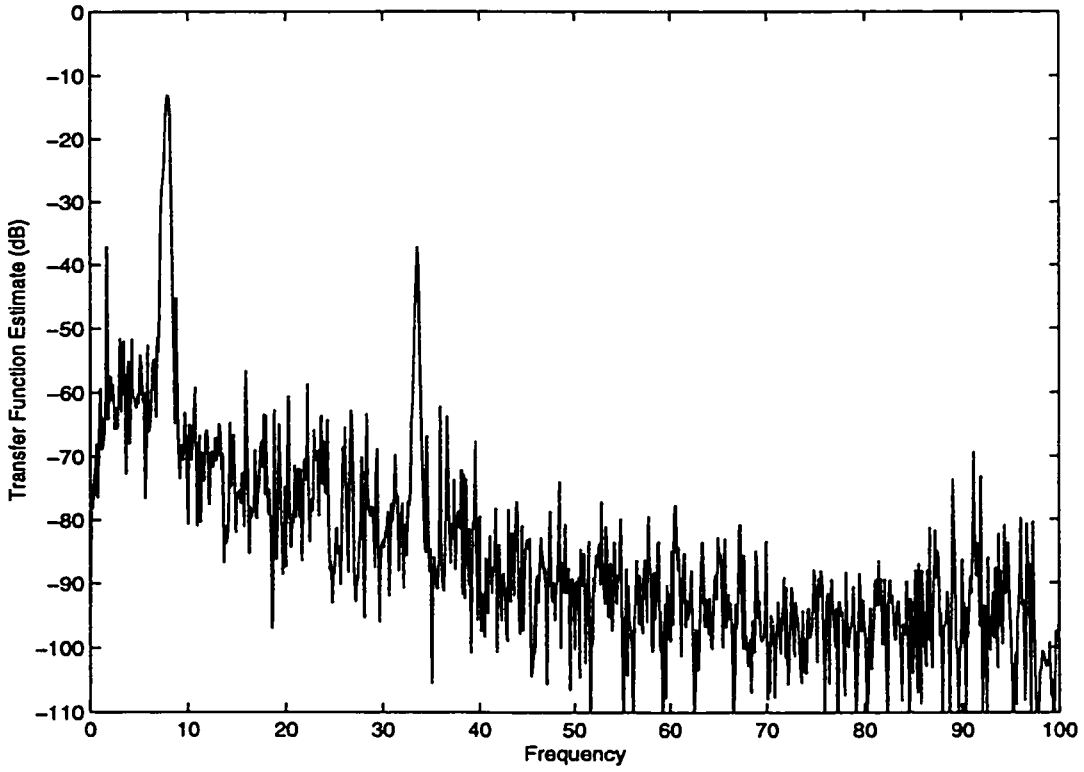

Figure 6.26: Frequency Response. Altered Structure. H_∞ Control (Experimental)

6.5. Experimental Results: Continuous Disturbance Test

In this experiment, a continuous sinusoidal disturbance signal is introduced into the structure. One of the active truss members that is not being used for control purposes is used as the disturbance source, and a sinusoidal signal is sent, tuned at the dominant resonant frequency of 13.3 Hz, with the maximum amplitude allowed by the amplifier of 560 V. The truss member that acts as a disturbance source is shown in Figure 6.27. The acceleration measurements were taken at node 24, and double integrated to obtain displacement measurements.

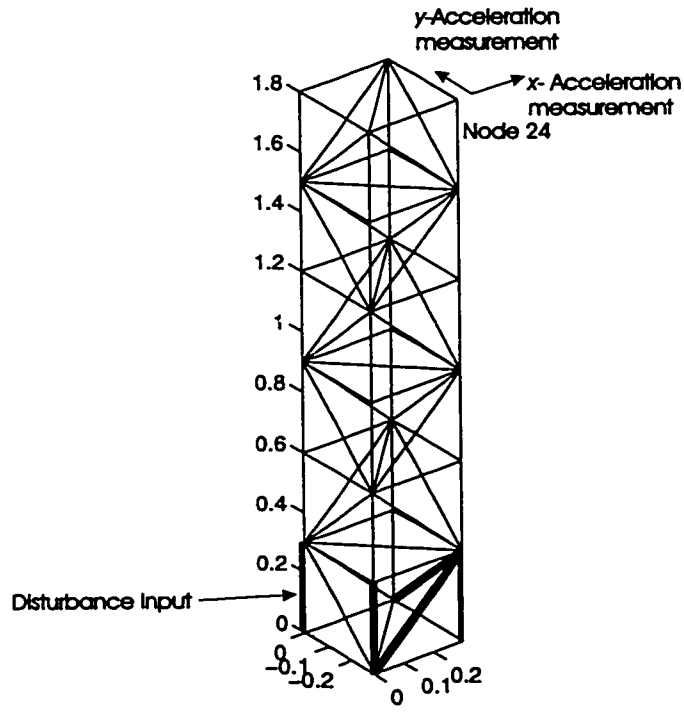

Figure 6.27: Application Point for the Continuous Disturbance

The test was performed on the three controllers. During the first 4 seconds of each test, the structure is oscillating without control. At that moment the controller is started. In this way it is possible to appreciate the effect of the controllers on the amplitude of oscillations.

6.5.1 Negative Velocity Feedback Control

Figure 6.28 and Figure 6.29 show the displacement and control signal response for the continuous disturbance test with negative velocity feedback control. The controller provides some attenuation on the amplitude of vibration. The velocity feedback controller is not able to concentrate control power on a particular mode of vibration, an thus it is comparatively ineffective.

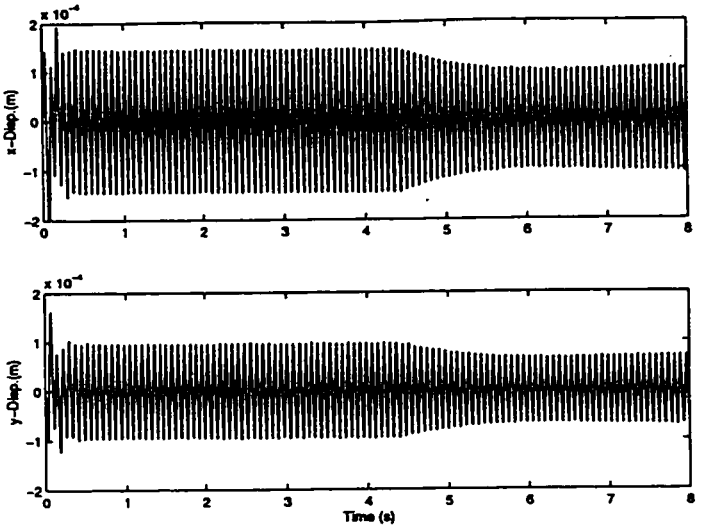

Figure 6.28: Displacement of Node 24. Continuous Disturbance Test. Velocity Feedback Control (Experimental)

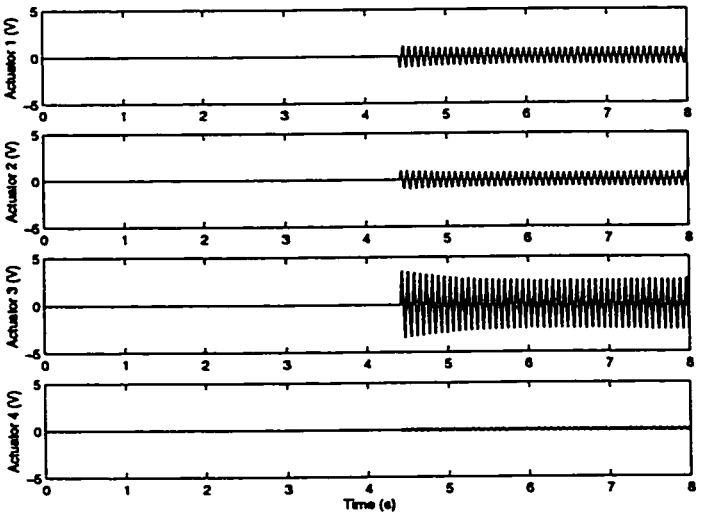

Figure 6.29: Control Signals. Continuous Disturbance Test. Velocity Feedback Control (Experimental)

6.5.2 LQG Control

The displacement and control responses are shown in Figure 6.30 and Figure 6.31 respectively. In this case the attenuation of the vibration amplitude is much more marked than in the velocity feedback case, as is expected from the frequency response plots shown in section 6.3. The controller is capable of directing the control power to a number of specific vibrational modes.

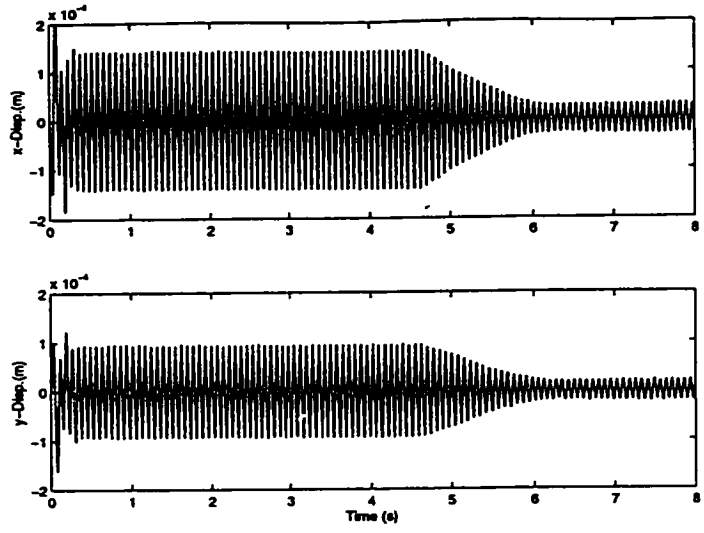

Figure 6.30: Displacement of Node 24. Continuous Disturbance Test. LQG Control (Experimental)

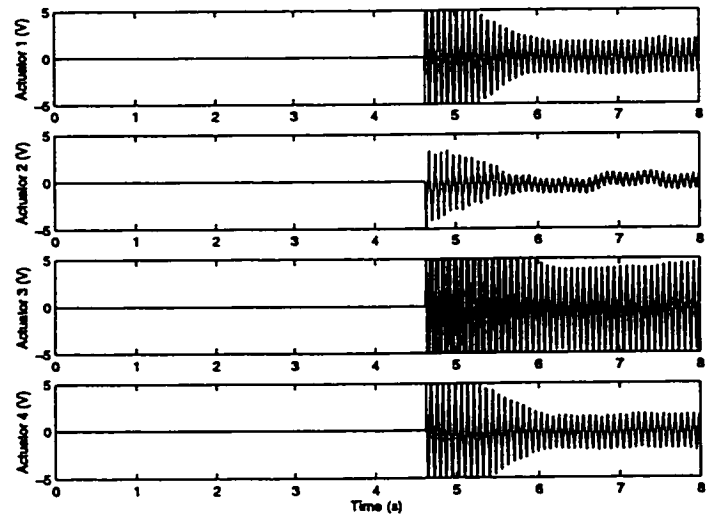

Figure 6.31: Control Signals. Continuous Disturbance Test. LQG Control (Experimental)

6.5.3 H_∞ Control

The displacement and control signal response for the continuous disturbance test using the H_∞ controller are shown in Figure 6.32 and Figure 6.33. The performance is the best of the controllers tested in this research. The vibration amplitude is attenuated by a factor of approximately 10, as predicted by the frequency response analysis.

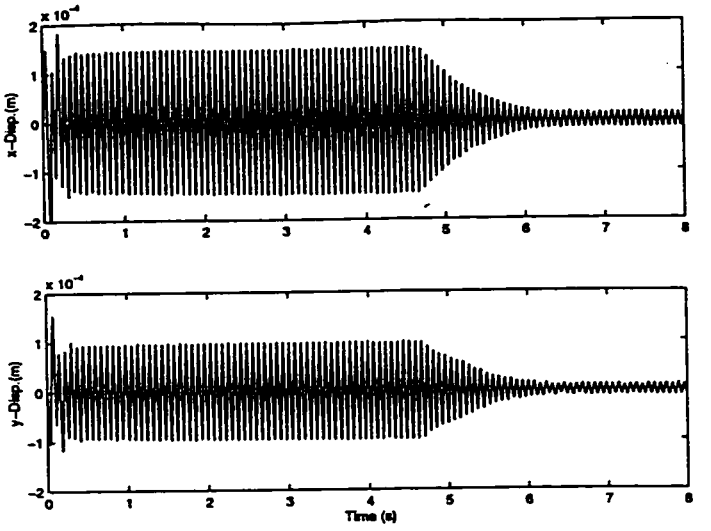

Figure 6.32: Displacement of Node 24. Continuous Disturbance Test. H_∞ Control (Experimental)

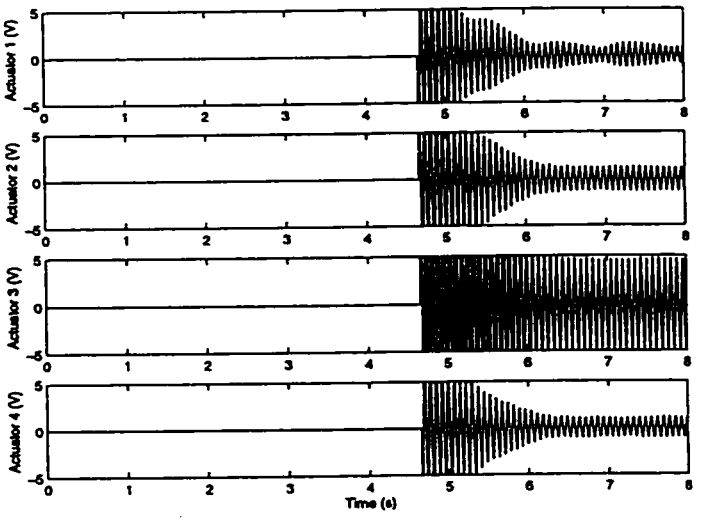

Figure 6.33: Control Signals. Continuous Disturbance Test. H_∞ Control (Experimental)

6.6. Summary

The experimental results for the active vibration control of the truss structure are presented. The configuration of the truss structure and its associated instrumentation and electronic hardware is described in detail. Results are presented for three experiments: impact test on the nominal structure, impact test on the perturbed structure, and continuous disturbance test. The experiments are performed for each of the control techniques presented in chapter 5: Negative Velocity Feedback, LQG, and H_∞ control, as well as on the open loop system to provide a reference for the performance of the controllers.

The experiments match well with the numerical simulation, confirming the findings obtained in chapter 5: the optimal controllers (LQG and H_∞) are effective in providing the largest amount of vibration suppression, due to their ability to target the control energy on a few specific modes of vibrations, as stipulated by the designer. The attenuation provided by each control law for the first five modes of the nominal structure, compared to the open loop case is shown in Table 6.2.

Table 6.2: Mode Attenuation. Nominal Structure

	Attenuation (dB)		
Mode	Velocity Feedback	LQG	H_∞
1	7	5	13
2	10	18	25
3	15	14	12
4	19	32	29
5	10	20	15

It can be seen that for the velocity feedback case, the attenuation generally increases with the mode frequency. This is to be expected, since the control signal increases proportionally to the strain rate. The LQG controller provides a high amount of attenuation for the five modes considered, and in fact, provides a higher attenuation than the H_∞ controller for the 3rd, 4th and 5th modes. This happens because the H_∞ controller is designed to minimize the maximum peak of the frequency response, which corresponds to the second mode at 13.3 Hz.

7. Conclusion

7.1. Summary and Discussion

In chapter 2, the dynamic model of a flexible one link manipulator was obtained. Lagrange's formula and the assumed modes method was used to obtain the model using generalized variables obtained from a modal analysis of a cantilever beam. A finite element analysis of the piezoelectric-beam interaction in the sensor application was performed, including the effect of shaping the sensor. A relation was found that allows for the design of sensors that provide a specific linear combination of modal amplitudes and gains, thus giving a feedback signal that can be used for control purposes. The state space observation matrix of the shaped piezoelectric sensor was obtained in terms of the state space variables.

The development of a control strategy for the flexible link manipulator was presented in chapter 3, taking advantage of the signal processing function of the piezoelectric sensor, obtained by shaping, as presented in chapter 2. A robust H_∞ state feedback controller was designed using LMI techniques, and was implemented using shaped PVDF films for modal strain and modal strain rate feedback. Numerical simulations of the closed loop system were performed. The results showed that the controller was capable of improving the performance of the manipulator when compared

to the case of no flexible states feedback. The settling time of the oscillations of the tip of the manipulator is decreased from 7 s to 2 s for a step input in the joint angle.

An experimental setup for the validation of the simulation results was designed and built, together with the development of techniques for the shaping and bonding of the PVDF piezoelectric sensors. The experimental results obtained confirm the findings of the numerical simulations, matching well with the previous results and showing the feasibility of the proposed approach.

In chapter 4, the procedure for the calculation of the state space representation of a truss structure, including the effect of piezoelectric actuators and sensors was presented. A design for a truss structure that represents a typical LFSS was shown, and its mathematical model was obtained using finite element analysis and modal decomposition. The influence of the piezoelectric actuators and sensors on the space state model of the truss structure was found, in the finite element-modal analysis framework.

The design and simulation of several control laws for the truss structure presented in chapter 4 is shown in chapter 5, taking advantage of the use of piezoelectric actuators and sensors. Three control techniques are tested: negative velocity feedback, LQG and H_∞ control. Impact test simulations are performed on the closed loop system (truss structure model plus control system) to assess the relative merits of each control technique, and to compare with experimental results obtained in chapter 6.

Results of the simulations show that the robust H_∞ controller provides the better performance of the control techniques presented, even in the presence of higher order dynamics included in the simulation model but not accounted for in the control design

process. From the point of view of controller complexity, the negative velocity feedback control technique is attractive, because it involves only static feedback, which results in a simpler controller to implement. The velocity feedback controller is also independent of the dynamic model, which adds a measure of robustness to parametric or modelling uncertainties.

The experimental results for the active vibration control of the truss structure are presented in chapter 6. The configuration of the truss structure and its associated instrumentation and electronic hardware is described in detail. Results are presented for three experiments: impact test on the nominal structure, impact test on the perturbed structure, and continuous disturbance test. The experiments are performed for each of the control techniques presented in chapter 5: Negative Velocity Feedback, LQG, and H_∞ control, as well as on the open loop system to provide a reference for the performance of the controllers.

The experiments match well with the numerical simulation, confirming the findings obtained in chapter 5: the dynamic optimal controllers (LQG and H_∞) are effective in providing the largest amount of vibration suppression to specific modes of vibration, due to their ability to target the control energy on a few specific modes of vibrations, as stipulated by the designer. The H_∞ controller provides the highest attenuation for the dominant resonant peak, as expected, since the controller tries to minimize the H_∞ norm of the closed loop, which corresponds to the maximum value of the frequency response of the system.

Simulations and experimental results on the truss structure confirm that the piezoelectric material are well suited for both sensing and actuating tasks. In sensing

applications, the PVDF piezoelectric material provides the advantages of light weight, good signal power, ease of handling and ruggedness, as well as the ability to be shaped to any desired configuration. In the actuation role, piezoceramic materials, such as PZT provide sufficient actuation power for the effective control of a large structure in a compact and simple package, with no mechanical moving parts, which adds to the reliability of a piezoelectric based control system.

7.2. Suggestions for Future Research

7.2.1 Flexible Link Manipulators

In terms of the flexible link manipulators, an interesting problem to explore is to extend the theory and methodology proposed in chapters 2 and 3 to multiple link systems. In this problem, the robustness of the feedback control laws could provide for the nonlinear nature of the dynamics, in particular of the inertial loads, due to the configuration changes. Another idea that comes to mind is the combination of nonlinear control techniques, such as feedback linearization, with smart links, with shaped piezoelectric sensors.

The use of piezoelectric actuators to act on the flexible links was not addressed in this research. Future work should look into the feasibility of the use of piezoceramic "muscles" as actuators. In this way, sensors and actuators collocated with the flexibility source might prove more effective in suppressing oscillations, in combination with joint actuators, as opposed to the current approach of only using rotary joint actuators for the combined purpose of joint angle control and flexible states control.

In terms of the implementation of the controllers using shaped piezoelectric sensors, even though the technique used in this research proved satisfactory, further work should be carried out in terms of the manufacturing process, to provide the designers with a reliable and precise technique involving numeric machine tools.

7.2.2 Flexible Truss Structures

Several ideas in the area of LFSS control can be examined in future research into the area. The first suggestion would be to examine the use approach of robust performance control laws, such as μ-synthesis (Zhou [44]). This techniques are able to guarantee a prescribed level of performance for a given level of system uncertainty (as opposed to guaranteed stability in the H_∞ control case). Boulet [9] and Buddie [12] propose approaches to model structure and unstructured uncertainties and disturbances. Applying this techniques to the problem of LFSS may provide controllers that give better responses, since tighter bounds on the uncertainties can be found.

The concept of spatial filters for feedback control, as presented for the flexible manipulator, could be extended to the truss structure configuration. Due to the simplicity and relative low cost of the PVDF piezoelectric material, all members of a truss could be instrumented with "shaped" sensors that can perform part of the computations needed for active vibration control, using piezoceramic actuators.

Another interesting line of research is the idea of localized control. In certain applications it might not be necessary to increase the damping or suppress vibrations in the complete structure, but only on certain locations, such as were sensitive payloads are located. In this applications piezoelectric materials seem to be well suited for sensing and actuation. Some approaches that have been proposed is the use of wave propagation

control (Pines [30]), and the use of point control and H_- local control (Morris [28]). Preliminary results have shown that problems can arise because of a spatial waterbed effect, in which the level of vibration outside the target area can increase to unacceptable levels.

The use of piezoelectric actuators and sensors for shape control in space applications should also be examined in the future. In certain types of large space structures, such as space based mirrors and antennas, thermal stresses might produce undesired deformations that may affect the performance of the system. Piezoelectric actuators can be used to correct the shape in combination with vibration control

8. References

[1] Allen, J.J., Lauffer, J.P., Marek, E.L., "The Sandia Structural Control Experiments", *Proceedings of the First Joint US/Japan Conference on Adaptive Structures*, pp. 928-951, Maui, Hawaii, 1990.

[2] Allen, J.J., Lauffer, J.P., "Design and Evaluation of Frequency Weighted LQG Maximum Entropy Controllers on an Experimental Truss Structure", *Journal of Dynamic Systems, Measurement, and Control*, Vol. 119, September 1997.

[3] Bailey, T., Hubbard, J. E., "Distributed Piezoelectric-Polymer Active Vibration Control of a Cantilever Beam", *Journal of Guidance, Control and Dynamics*, Vol. 8, pp. 605-611, Sept.-Oct. 1985.

[4] Balas, M.J., "Direct Velocity Feedback of Large Space Structures", *Journal of Guidance and Control*, Vol. 2, No. 3, pp 252-253, May-June 1979.

[5] Balas, M.J., "Trends in Large Space Structure Control Theory: Fondest Hopes, Wildest Dreams", *IEEE Transactions in Automatic Control*, Vol. 27, No. 3, pp. 522-535, 1982.

[6] Biswas, S. K., Klafter, R. D., "Dynamic Modeling and Optimal Control of Flexible Robotic Manipulators", *Proceedings of the 1988 IEEE International Conference on Robotics and Automation*, Vol. 1, pp. 15-20, 1988.

[7] Book, W. J., Maizza-Neto, O., Whitney, D. E., "Feedback Control of Two-Beam, Two-Joint Systems with Distributed Flexibility", *Journal of Dynamic Systems, Measurement and Control*, pp. 424-431, December 1975.

[8] Book, W. J., "Modeling, Design and Control of Flexible Manipulator Arms: A Tutorial Review", *Proceedings of the 29th Conference on Decision, Control and Dynamics*, pp. 500-506, Honolulu, Hawaii, 1990.

[9] Boulet, B., *Modeling and Robust Control of Large Flexible Space Structure*, Ph.D. Thesis, Dept. of Electric and Computer Engineering, University of Toronto, 1996.

[10] Bravo, R., Farr, T., Vaz, A.F., *Analysis and Testing of Flexible Structure Dynamics*, Report submitted to the Canadian Space Agency for contract 9F028-6-6162, December 1997.

[11] Bravo, R., Leatherland, S. Vaz, A.F., *Final Report on Design and Construction of a Truss Structure Testbed*, Report submitted to the Canadian Space Agency for contract 9F028-8-2094/001-XSD, April 1999.

[12] Buddie, S.A. and Goergiu, T.T., Özgüner, Ü., Smith, M.C., "Flexible Structure Experiments at JPL and WPAFB: H_∞ Controller Designs", *International Journal of Control*, Vol. 58, No. 1, pp. 1-19, 1993.

[13] Burke, S. E.and Hubbard, J. E., "Active Vibration Control of a Simply Supported Beam Using a Spatially Distributed Actuator", *IEEE Control Systems Magazine*, pp. 25-30, August 1987.

[14] Cannon, R. H.and Schmitz, E., "Initial Experiments on the End-Point Control of a Flexible One-Link Robot", *The International Journal of Robotics Research*, Vol. 3, No. 3, pp. 62-75, Fall 1984.

[15] Crawley, E. F. and de Luis, J. "Use of Piezoelectric Actuators as Elements of Intelligent Structures", *AIAA Journal*, Vol. 25, No. 10, pp. 1373-1385, 1987.

[16] Doyle, J.C., "Guaranteed Magins for LQG Regulators", *IEEE Transactions in Automatic Control*, Vol. AC-23, No. 4, pp. 756-757, 1978.

[17] Doyle, J.C., Glover, K., Khargonekar, P.P. and Francis, B.A., "State-space solutions to standard H_2 and H_∞ control problems", *IEEE Transactions in Automatic Control*, Vol. AC-34, No. 8, pp. 831-847, 1989.

[18] Farr, T., *Shaped Piezoelectric Sensors and Actuators for Structural Control*, Master of Engineering Thesis, McMaster University, Hamilton, 1997.

[19] Francis, B.A., *A Course in H_∞ Control Theory*, Lecture Notes in Control and Information Series, Vol. 88, 1987.

[20] Gahinet, P., "Explicit Controller Formulas for LMI-based H_∞ Synthesis", *Automatica*, Vol. 32, No. 7, pp. 1007-1014, 1996.

[21] Glover, K., Doyle, J.C., "State-Space Formulae for All Stabilizing Controllers that Satisfy an H_∞ Norm Bound And Relations to Risk Sensitivity", *System and Control Letters*, Vol. 11, pp. 167-172, 1988.

[22] Gupta, N.K. "Frequency_Shaped Cost Functionals: Extension of Linear-Quadratic-Gaussian Methods", *Journal of Guidance, Control and Dynamics*, Vol. 3, No. 6, Nov.-Dec. 1980

[23] Hastings, G. G., Book, W. J., "A Linear Dynamic Model for Flexible Robotic Manipulators", *IEEE Control Systems Magazine*, pp. 61-64, February 1987.

[24] Lee, C.K., Moon, F.C., "Modal Sensors/Actuators", *Journal of Applied Mechanics*, Vol. 57, No. 6, pp. 434-441, 1990.

[25] Hanselman, D.C., *Mastering MATLAB 5 : a comprehensive tutorial and reference*, Prentice Hall, N.J., 1998.

[26] Meirovich, L., *Elements of Vibration Analysis*, New York: McGraw-Hill, 1975.

[27] Miller, D. W., van Schoor, M., "Formulation of Full State Feedback for Finite Order Structural Systems", *Proceedings of the First Joint US/Japan Conference on Adaptive Structures*, pp. 304-331, Maui, Hawaii, 1990.

[28] Morris, K.A., "Noise Reduction in Ducts Achievable by Point Control", Accepted for Publication, *Journal of Dynamic Systems, Measurement and Control*,1998.

[29] Naganathan, G., Soni, A. H., "Coupling Effects of Kinematics and Flexiblity on Manipulators", *The International Journal of Robotics Research*, Vol. 6, No. 1, pp. 75-84, Spring 1987.

[30] Pines, D.J., *Wave Propagation Sensors for Structural Control*, Ph.D. Thesis, Department of Mechanical Engineering, Massachusetts Institute of Technology, 1992.

[31] Plump, J. M., Hubbard, J. E., Bailey, T., "Nonlinear Control of a Distributed System: Simulation and Experimental Results", *Journal of Dynamic Systems, Measurement, and Control*, Vol. 109, pp. 133-139, June 1987.

[32] Popov, E.P., *Mechanics of Materials*, 2nd Edition, Prentice-Hall Inc., Englewood Cliffs, New Jersey, 1976

[33] Ravichandran, T., Pang, G.K.H. and Wang, D., "Robust H_∞ Optimal Control of a Single Flexible Link", *Control-Theory and Advanced Technology*, Vol. 9, No. 4, pp. 887-908, December 1993.

[34] Ryou, J. K., Park, K. Y., Kim, S. J., "Electrode Pattern Design of Piezoelectric Sensors and Actuators Using Genetic Algorithms", *AIAA Journal*, Vol. 36, No. 2, pp. 227-233, February 1998.

[35] SDRC Corp., *I-DEAS Master Series Student Guide*, OnWorld Press, 1996.

[36] Sunada, W., Dubowsky, S., "On the Dynamic Analysis and Behavior of Industrial Robotic Manipulators with Elastic Members", *Journal of Mechanisms, Transmission Automation in Design*, Vol.105, pp. 42-51, March 1983.

[37] Van Woerkom, P.Th.L.M., "Synthesis and Survey of Control Laws for Large Flexible Spacecraft", , *Control-Theory and Advanced Technology*, Vol. 9, No. 3, pp. 639-669, September 1993.

[38] Vaz, A.F., *Modelling Piezoelectric Behaviour for Actuator and Sensor Applications*, Report submitted to the Canadian Space Agency for contract 9F009-0-4140., 1991.

[39] Vaz, A.F., *Theoretical Development for an Active Vibration Damping Experiment*, Report submitted to the Canadian Space Agency for contract 9F009-0-4140., 1991.

[40] Vaz, A.F., *Empirical Verification of Interaction Equations with Bonded Piezoelectric Films*, Report submitted to the Canadian Space Agency for contract 9F009-0-4140., 1991.

[41] Vaz, A.F., "Composite Modeling of Flexible Structures with Bonded Piezoelectric Film Actuators and Sensors", *IEEE Transactions on Intrumentation and Measurement*, Vol. 24, No. 2, April 1998.

[42] Wang, D., "Comparison of Control Strategies for the Single Flexible Link", *Fields Institute Communications Vol. 2: Control of Flexible Structures*, American Mathematical Society, 1993.

[43] Weaver, W., Johnston, P. R., *Structural Dynamics by Finite Elements*, New Jersey: Prentice Hall, 1987.

[44] Zhou, K., Doyle, J. C., Glover, K., *Robust and Optimal Control*, New Jersey, Prentice Hall, 1995.

Appendix A

LQG Controller Design for the Truss Structure

The design of the LQG control law for the truss structure was performed using the control toolbox of Matlab, using the equations found in section 5.4. The matrices R_1 and R_2, which are the weights on the states and control inputs, respectively, are chosen as:

$$R_1 = \begin{bmatrix} 20 & 0 & 0 & 0 & 0 & 0 & 0 & 0 & 0 & 0 \\ 0 & 20 & 0 & 0 & 0 & 0 & 0 & 0 & 0 & 0 \\ 0 & 0 & 30 & 0 & 0 & 0 & 0 & 0 & 0 & 0 \\ 0 & 0 & 0 & 40 & 0 & 0 & 0 & 0 & 0 & 0 \\ 0 & 0 & 0 & 0 & 50 & 0 & 0 & 0 & 0 & 0 \\ 0 & 0 & 0 & 0 & 0 & 1 & 0 & 0 & 0 & 0 \\ 0 & 0 & 0 & 0 & 0 & 0 & 1 & 0 & 0 & 0 \\ 0 & 0 & 0 & 0 & 0 & 0 & 0 & 1 & 0 & 0 \\ 0 & 0 & 0 & 0 & 0 & 0 & 0 & 0 & 1 & 0 \\ 0 & 0 & 0 & 0 & 0 & 0 & 0 & 0 & 0 & 1 \end{bmatrix} \qquad R_2 = 1 \times 10^{-4} I_{4x4}$$

The matrices W and V, estimates of the noise intensity in the control and sensor signals, respectively, are given by:

$$W = 0.01 \times I_{10x10} \qquad V = 0.1 \times I_{4x4}$$

The resulting state space matrices that define the LQG dynamic controllers are found to be:

A_{10x10}=

-5.46E+02	9.80E-12	-4.30E-11	5.77E+02	1.85E-10	1.00E+00	0.00E+00	0.00E+00	0.00E+00	0.00E+00
-2.85E-12	-6.06E+02	1.24E+02	-7.06E-12	-5.55E+02	0.00E+00	1.00E+00	0.00E+00	0.00E+00	0.00E+00
2.89E-11	9.05E+00	-9.58E+02	4.01E-11	1.41E+03	0.00E+00	0.00E+00	1.00E+00	0.00E+00	0.00E+00
4.64E+02	1.76E-11	-7.28E-12	-1.99E+03	3.29E-11	0.00E+00	0.00E+00	0.00E+00	1.00E+00	0.00E+00
4.38E-11	-2.47E+02	8.61E+02	1.99E-11	-1.41E+03	0.00E+00	0.00E+00	0.00E+00	0.00E+00	1.00E+00
2.32E+02	-7.94E-10	2.54E-09	-1.41E+04	-4.59E-09	-1.56E+01	-1.53E-13	-6.66E-15	1.32E+01	6.61E-13
-5.33E-10	-1.96E+03	-9.10E+03	8.20E-10	1.51E+04	-1.61E-13	-1.40E+01	3.55E+00	4.61E-13	-6.72E+00
1.11E-08	-4.08E+04	8.33E+04	-1.55E-08	-1.96E+05	-1.19E-13	7.82E+00	-2.56E+01	0.00E+00	2.85E+01
2.54E+04	-3.18E-09	1.10E-08	-1.35E+05	-2.21E-08	3.79E+01	1.17E-12	2.13E-14	-4.78E+01	-4.97E-14
2.25E-08	-8.58E+04	2.34E+05	-3.40E-08	-5.05E+05	1.83E-12	-2.01E+01	3.96E+01	-4.97E-14	-4.59E+01

B_{10x4}=

2.84E-01	9.55E-02	-9.94E-14	9.55E-02
7.85E-14	2.30E-02	3.13E-01	-2.30E-02
-3.46E-15	-1.78E-01	6.37E-02	1.78E-01
-1.56E-01	1.92E-01	-1.82E-14	1.92E-01
-9.53E-15	1.60E-01	6.94E-02	-1.60E-01
-1.81E+00	6.72E-01	5.32E-13	6.72E-01
3.94E-14	-1.61E+00	-9.28E-01	1.61E+00
-2.35E-12	2.14E+01	1.31E+01	-2.14E+01
-1.28E+01	-3.07E-01	4.29E-12	-3.07E-01
-4.07E-12	4.46E+01	2.89E+01	-4.46E+01

C_{4x10}=

-1.84E+02	1.07E-11	-1.19E-10	-1.53E+03	9.44E-11	1.03E+02	2.54E-11	-1.40E-13	-7.42E+01	-1.26E-13
1.23E+02	-2.22E+02	1.49E+03	2.78E+02	3.33E+03	-1.76E+01	2.18E+01	-7.14E+01	5.78E+01	7.96E+01
8.33E-12	-3.53E+01	-9.91E+01	2.53E-10	8.20E+02	-2.05E-11	1.03E+02	-7.36E-01	5.46E-13	2.28E+01
1.23E+02	2.22E+02	-1.49E+03	2.78E+02	-3.33E+03	-1.76E+01	-2.18E+01	7.14E+01	5.78E+01	-7.96E+01

D_{4x4}=

0.00E+00	0.00E+00	0.00E+00	0.00E+00
0.00E+00	0.00E+00	0.00E+00	0.00E+00
0.00E+00	0.00E+00	0.00E+00	0.00E+00
0.00E+00	0.00E+00	0.00E+00	0.00E+00

Appendix B

H_∞ Controller Design for the Truss Structure

The design of the H_∞ control law was done using the control and LMI Lab toolboxes of Matlab, using the relations given in section 5.5. If the state space matrices of the model used for control synthesis are:

$$\hat{G}_c = \left[\begin{array}{c|c} A_c & B_c \\ \hline C_c & D_c \end{array}\right]$$

then LFT representation, necessary for the design, was obtained as:

$$B_1 = [0.1B_c \quad 0_{10x4}] \qquad B_2 = B_c$$

$$C_1 = \begin{bmatrix} Q \\ 0_{4x10} \end{bmatrix} \qquad C_2 = C_c$$

$$D_{11} = 0_{14x8} \qquad D_{12} = \begin{bmatrix} 0_{10x4} \\ R \end{bmatrix}$$

$$D_{21} = 0.01 \times [0_{4x4} \quad I_{4x4}] \qquad D_{22} = D_c$$

where Q and R are weights on state and control, chosen as:

$$Q = \begin{bmatrix} 20 & 0 & 0 & 0 & 0 & 0 & 0 & 0 & 0 & 0 \\ 0 & 20 & 0 & 0 & 0 & 0 & 0 & 0 & 0 & 0 \\ 0 & 0 & 30 & 0 & 0 & 0 & 0 & 0 & 0 & 0 \\ 0 & 0 & 0 & 40 & 0 & 0 & 0 & 0 & 0 & 0 \\ 0 & 0 & 0 & 0 & 50 & 0 & 0 & 0 & 0 & 0 \\ 0 & 0 & 0 & 0 & 0 & 0 & 0 & 0 & 0 & 0 \\ 0 & 0 & 0 & 0 & 0 & 0 & 0 & 0 & 0 & 0 \\ 0 & 0 & 0 & 0 & 0 & 0 & 0 & 0 & 0 & 0 \\ 0 & 0 & 0 & 0 & 0 & 0 & 0 & 0 & 0 & 0 \\ 0 & 0 & 0 & 0 & 0 & 0 & 0 & 0 & 0 & 0 \end{bmatrix} \qquad R = 1 \times 10^4 I_{4x4}$$

The resulting controller state space matrices obtained from the LMI optimization process are given next:

A_{10x10}=

-7.80E+00	-1.38E-13	-1.18E-13	2.95E+01	1.45E-12	1.00E+00	0.00E+00	0.00E+00	0.00E+00	0.00E+00
-1.42E-13	-5.04E+00	5.45E+00	8.68E-13	-1.37E+01	0.00E+00	1.00E+00	0.00E+00	0.00E+00	0.00E+00
-1.22E-14	1.73E+00	-8.85E+00	1.78E-15	1.86E+01	0.00E+00	0.00E+00	1.00E+00	0.00E+00	0.00E+00
5.79E+00	2.04E-13	-1.78E-15	-1.75E+01	-3.82E-14	0.00E+00	0.00E+00	0.00E+00	1.00E+00	0.00E+00
2.56E-13	-2.66E+00	1.13E+01	-2.40E-14	-1.27E+01	0.00E+00	0.00E+00	0.00E+00	0.00E+00	1.00E+00
-4.89E+03	6.00E-12	-4.52E-12	-1.28E+03	-2.78E-11	-3.68E+01	1.21E-12	2.55E-14	8.47E+00	8.25E-13
5.75E-11	-7.01E+03	-1.03E+02	6.27E-11	7.18E+01	5.49E-13	-6.96E+01	4.33E+00	2.25E-13	-8.82E+00
-6.80E-11	1.43E+03	-3.27E+04	-4.97E-13	-2.71E+03	-9.50E-13	4.72E+01	-2.17E+01	4.88E-14	3.30E+01
3.12E+01	1.77E-10	-1.93E-11	-8.25E+04	-2.91E-13	9.10E+01	1.54E-12	-1.14E-13	-2.96E+01	-2.20E-13
1.35E-10	-3.04E+03	-3.67E+03	-2.94E-11	-1.02E+05	5.76E-12	-1.12E+02	3.44E+01	-2.24E-13	-5.37E+01

B_{10x4}=

1.50E+00	-2.67E-01	-2.03E+00	-3.79E+00
3.22E-13	2.88E-01	5.77E-01	8.65E-01
-2.86E-15	-6.31E-01	-1.26E+00	-1.89E+00
-6.16E-01	4.69E-01	1.55E+00	2.64E+00
4.29E-16	5.92E-01	1.18E+00	1.78E+00
8.35E+00	-2.78E+00	-1.39E+01	-2.50E+01
1.25E-12	1.83E+00	3.67E+00	5.50E+00
-5.18E-13	-4.77E+00	-9.54E+00	-1.43E+01
-1.30E+01	5.39E+00	2.38E+01	4.21E+01
4.61E-13	1.06E+01	2.11E+01	3.17E+01

C_{4x10}=

1.62E+01	1.23E-11	-1.39E-12	-8.63E+00	2.88E-12	8.69E-01	3.97E-13	-1.02E-14	-1.73E-01	5.39E-15
-3.76E+00	1.81E+01	-4.26E+00	2.85E+00	1.79E+01	-1.64E-01	4.72E-01	-2.17E-01	1.22E-01	3.30E-01
-4.59E-12	5.27E+01	-6.00E+00	1.13E-12	1.63E+01	-1.93E-13	1.80E+00	-3.99E-02	6.43E-15	1.24E-01
-3.76E+00	-1.81E+01	4.26E+00	2.85E+00	-1.79E+01	-1.64E-01	-4.72E-01	2.17E-01	1.22E-01	-3.30E-01

D_{4x4}=

0.00E+00	0.00E+00	0.00E+00	0.00E+00
0.00E+00	0.00E+00	0.00E+00	0.00E+00
0.00E+00	0.00E+00	0.00E+00	0.00E+00
0.00E+00	0.00E+00	0.00E+00	0.00E+00